

# On-Surface Assembly and Reactions of Organic Molecules in Ultra-High Vacuum

THÈSE N° 7348 (2016)

PRÉSENTÉE LE 20 DÉCEMBRE 2016  
À LA FACULTÉ DES SCIENCES DE BASE  
LABORATOIRE DE SCIENCE À L'ÉCHELLE NANOMÉTRIQUE  
PROGRAMME DOCTORAL EN PHYSIQUE

ÉCOLE POLYTECHNIQUE FÉDÉRALE DE LAUSANNE

POUR L'OBTENTION DU GRADE DE DOCTEUR ÈS SCIENCES

PAR

Claudius MORCHUTT

acceptée sur proposition du jury:

Prof. C. Hébert, présidente du jury  
Prof. K. Kern, directeur de thèse  
Prof. T. Greber, rapporteur  
Prof. T. Jung, rapporteur  
Dr W. Harbich, rapporteur



ÉCOLE POLYTECHNIQUE  
FÉDÉRALE DE LAUSANNE

Suisse  
2016



# Acknowledgements

This Ph.D. thesis would not have been possible without the support of many people. First and foremost I would like to thank my supervisor **Prof. Klaus Kern** who offered me this challenging research topic and gave me the opportunity to work in his department ‘Nanoscale Science’ at the Max Planck Institute for Solid State Research in Stuttgart (Germany). Without his knowledge and assistance this work would not have been possible. Furthermore, I wish to express my gratitude for giving me the opportunity to attend various conferences and workshops to shape and increase my scientific knowledge.

In addition, I would like to thank my group leader **Dr. Rico Gutzler** who was abundantly helpful and available for scientific discussions. He was encouraging at any time and became a good friend. I appreciate his scientific expertise and profound knowledge which helped me immensely.

Furthermore, I am grateful to **Prof. Thomas Jung**, **Prof. Thomas Greber**, and **Dr. Wolfgang Harbich** for agreeing to be part of my thesis committee and **Prof. Cécile Hébert** for agreeing to be the jury president.

Gratitude is also due to **Dr. Magali Lingenfelder**, head of the Max-Planck-EPFL Nanolab in Lausanne (Switzerland), who guided my research activities in my first year (first part of the first chapter of this thesis).

Moreover, I would like to thank my collaborators **Dr. Jonas Björk** for supporting and corroborating experimental findings theoretically, and **Prof. Bettina Lotsch** and **Dr. Vijay Vyas** for providing tailor-made molecules.

I am thankful to each 6B15 laboratory member. In particular to **Dr. Sören Krotzky** who introduced me to the system and taught me the basics and all the unwritten tricks about UHV and STM, **Dr. Benjamin Wurster** who shared the lab with me for around a year and answered every little question with patience, and **Dr. Doris Grumelli** who shares the great attention to detail with me and was always available for discussions. Special thanks go to my lab as well as office colleague **Diana Hötger** for the positive atmosphere and attitude, her organizing talents and the philosophical debaucheries about life. Also many thanks to my other office colleagues **Kristina Vaklinova**, **Dr. Pas-**

## Acknowledgements

---

**cal Gehring**, and **Elise Duquesne** for the steadily productive and pleasant atmosphere in our office.

I am grateful to **Prof. Ulrich Starke** and **Dr. Carola Straßer** for introducing me to the in-house XPS facilities, **Tolga Acartürk** and **Artur Küster** for their technical support.

During my Ph.D. many colleagues became very good friends. I am thankful to **Christian Dette**, **Dr. Stiven Forti**, **Sabine Abb**, **Dr. Berthold Jäck**, **Pascal Gröger**, and **Matthias Munks** for pizza and beer sessions and the good times.

I am also grateful to the non-scientific people who were always willing to help, **Wolfgang Stiepany**, **Peter Andler**, **Marko Memmler**, **Rafail Chaikévitch**, and **Martin Siemers**.

Thanks are also due to our secretary **Sabine Birtel** for her friendly help with paperwork. Special thanks go to **Anh Eymann**, secretary of the doctoral program at EPFL, for the organizational help during my Ph.D.

I would like to express my gratitude to all colleagues and friends at the Max Planck Institute for being helpful, sociable and respectful at all times, **Dr. Markus Ternes**, **Dr. Christian Ast**, **Dr. Markus Etzkorn**, **Dr. Uta Schlickum**, **Dr. Stephan Rauschenbach**, **Prof. Kannan Balasubramanian**, **Dr. Soon Jung Jung**, **Dr. Marko Burkhard**, **Dr. Klaus Kuhnke**, **Dr. Christian Schön**, **Dr. Tobias Herden**, **Tomas Michnowicz**, **Anna Roslawska**, **Dr. Loc Duon Dinh**, **Roberto Urcuyo**, **Patrick Sailer**, **Dr. Christoph Große**, **Patrick Alexa**, **Shai Mangel**, **Alexander Kölker**, **Alessio Scavuzzo**, **Stephan Link**, **Dr. Kathrin Müller**, **Dr. Alexander Stöhr**, **Jacob Senkpiel**, **Lukas Schlipf**, **Sebastian Koslowski**, **Dr. Matthias Eltschka**, **Dr. Verena Schendel**, **Ahmed Faleh**, **Jing Wang**, **Soudabeh Mashhadi**, **Piotr Kot**, **Dr. Pablo Marino**, **Katharina Polyudov**, **Dr. Laura Zuccaro**, **Dr. Hadj Benia**, **Dr. Alexander Hoyer**, **Andreas Topp**, and **Dr. Eike Oliver Schäfer-Nolte**.

Finally, I offer my regards and blessings to all of those who supported me in any respect during the completion of this work. In particular I wish to express my love and gratitude to **my family**; for their understanding and endless love through the duration of my studies.

Last but not least my special thanks go to all those innumerable and nameless STM tips which crashed (accidentally and intentionally) for the benefit of the research.

*Stuttgart, August 2016*

C. M.



# Abstract

Two-dimensional (2D) materials are potentially suitable for applications in various fields such as molecular electronics, host-guest chemistry, sensors, etc. In particular, 2D structures built up by organic molecules relying on self-organizing and -assembly phenomena are formed inexpensively and efficiently. However, 2D materials stabilized by supramolecular chemistry generally suffer from limited stability. Therefore, 2D polymers formed by organic molecules which are interconnected by covalent bonds have attracted great research attention since the last decade due to their improved stability.

This thesis comprises the study of both types of 2D materials, those stabilized by non-covalent and those by covalent interactions. They are synthesized and studied on well-defined metallic surfaces in ultra-high vacuum (UHV). First, the self-assembly of terephthalic acid (TPA) on Ag(100) is explored. TPA stays intact upon deposition at room temperature (RT) and forms densely packed islands stabilized by hydrogen bonds. The TPA islands influence the homoepitaxial growth of silver. After Ag deposition in presence of TPA, less Ag is observed on TPA covered regions compared to clean terraces because the presence of TPA islands reduce the sticking coefficient of Ag atoms. Moreover, at RT Ag atoms intercalate TPA islands which are not disrupted. In contrast, TPA molecules in conjunction with Mg atoms on Ag(100) results in tip-induced altering of the surface at RT. The electric field between tip and sample interacts with Mg atoms and TPA molecules which leads to a restructuring of the step-edges during scanning. Moreover, the self-assembly of the organic semiconductor 2,7-dicyano[1]benzothiophene[3,2-b]benzothiophene (cBTBT) on Ag(111) at RT is presented. The pro-chiral molecules form compact islands with a chevron-like structure containing both enantiomers. The network is stabilized by hydrogen bonds. Deposition of Fe atoms leads to an amorphous metal-organic coordination network (MOCN) comprising Fe atoms as metal centers and cBTBT as ligands. Statistical analysis of the network reveals that conformational entropy plays a critical part in its stabilization. Phase segregation of the network into spatially homogeneously crystalline domains of molecules and metal atoms upon annealing and subsequent cooling suggests that the amorphous network is kinetically trapped at RT during the preparation process. The second part presents the on-surface synthesis of 2D polymers via different cou-

pling schemes. The resulting 2D materials are stabilized by covalent bonds and are thus more resistant against external influences. First, the Ullmann coupling on Au(111) is explored. The precursor molecule 1,3,5-tris(4-bromophenyl)benzene (TBPB) debrominates upon annealing and polyphenylene is formed. To investigate the influence of metal substrates on the dehalogenation, a single layer of hexagonal boron nitride (h-BN) as well as graphene grown on Ni(111) is introduced. On both surfaces TBPB forms densely packed self-assembly islands stabilized by halogen bonds, while on bare Ni(111) the substrate-molecule interaction dominates resulting in structures without long-range order. Upon annealing on both surfaces, h-BN/Ni(111) and graphene/Ni(111), dehalogenation is induced and 2D nanostructures are formed. In contrast, on bare Ni(111) the precursor molecules merely decompose upon annealing. The experimental annealing temperatures are consistent with debromination barriers calculated by DFT for the model compound bromobenzene. An example of the synthesis of tailor-made 2D structures by using particularly designed precursor molecules is given. A terminal alkyne with a triazine core undergoes on-surface Glaser coupling and cyclotrimerization on Au(111) resulting in nitrogen doped 2D polymers. Finally, a comprehensive study of the on-surface decarboxylation reaction of the precursor molecule 1,3,5-tris(4-carboxyphenyl)benzene (TCPB) on Cu(111) is presented. TCPB deprotonates upon deposition on Cu(111) at RT and self-assembles in compact islands forming a  $3\sqrt{3} \times 3\sqrt{3}R30^\circ$  superstructure. The self-assembly is stabilized by ionic hydrogen bonds between deprotonated and (partially) negatively charged oxygen atoms and hydrogen atoms of neighboring molecules. Annealing leads to decarboxylation and formation of 2D nanostructures. The reaction occurs in a clean fashion because  $\text{CO}_2$  leaves the surface. In addition, STS reveals that the lowest unoccupied molecular orbital (LUMO) of the 2D polymer is destabilized compared to the LUMO of the monomer although the  $\pi$ -electron system is more extended in the polymer. The decarboxylation impacts the energy position of the LUMO to a greater extend which is corroborated by DFT calculations of the model compound biphenyl-4-carboxylic acid.

**Keywords:** *Homoepitaxial growth, self-assembly, amorphous metal-organic coordination network, covalent coupling, Ullmann coupling, Glaser coupling, cyclotrimerization, decarboxylation, HOMO/LUMO gap, porous polymer, hexagonal boron nitride, graphene*

## Zusammenfassung

2D-Materialien können in den verschiedensten Bereichen wie beispielsweise in der Molekularelektronik oder Sensortechnik Anwendung finden. Insbesondere 2D-Strukturen, die auf organischen Molekülen aufbauen und auf Selbstorganisations- und Selbstassemblierungsprozessen beruhen, sind kostengünstig und effizient herstellbar. Allerdings stellt die begrenzte Stabilität von 2D-Materialien, die aus supramolekularen Wechselwirkungen aufgebaut sind, einen großen Nachteil dar. Deshalb sind 2D-Polymere, die nur aus kovalenten Bindungen aufgebaut und somit stabiler sind, seit Beginn des letzten Jahrzehnts in den Fokus der Forschung gerückt. Diese Arbeit umfasst die Untersuchung von 2D-Materialien, die einerseits durch nicht-kovalente Bindungen stabilisiert werden und andererseits nur aus kovalenten Bindungen aufgebaut sind. Hergestellt und untersucht werden sie auf wohldefinierten, metallischen Oberflächen im Ultrahochvakuum (UHV). Zu Beginn wird die Selbstassemblierung von Terephthalsäure (TPA) auf Ag(100) näher beleuchtet. TPA Moleküle bleiben beim Aufdampfen bei RT unversehrt und bilden dichtgepackte, selbstassemblierte Inseln, die durch Wasserstoffbrückenbindungen stabilisiert sind. Diese TPA-Inseln beeinflussen das homoepitaktische Wachstum von Ag. Die TPA-Inseln reduzieren den Haftkoeffizienten der ankommenden Ag-Atome, wodurch weniger Ag auf TPA-Inseln zu beobachten ist. Darüber hinaus diffundieren die Ag-Atome durch die TPA-Inseln, die dabei intakt bleiben. Im Gegensatz dazu führt das Aufdampfen von TPA und Mg-Atomen auf Ag(100) zu einer spitzeninduzierten Veränderung der Oberfläche. Das elektrische Feld zwischen STM-Spitze und Probe wechselwirkt mit den Mg-Atomen und TPA-Molekülen, sodass eine Umstrukturierung der Stufenkanten hervorgerufen wird. Außerdem wird die Selbstassemblierung des organischen Halbleiters 2,7-Dicyano[1]benzothiophene[3,2-b]benzothiophen (cBTBT) auf Ag(111) bei RT untersucht. Die pro-chiralen Moleküle ordnen sich in einem Fischgrätenmuster an und bilden kompakte Inseln, die beide Enantiomere enthalten. Das Netzwerk ist durch Wasserstoffbrückenbindungen stabilisiert. Das zusätzliche Aufdampfen von Fe-Atomen führt zu einem amorphen metall-organischen Koordinationsnetzwerk (MOCN), bestehend aus Fe-Atomen als Metallzentren und cBTBT-Molekülen als Liganden. Statistische Auswertungen legen nahe, dass die Konformationsentropie des amorphen Netzwerkes eine entscheidende Rolle bei der Stabilisierung spielt. Die Phasentrennung des Netz-

werkes in räumlich homogene und kristalline Domänen, bestehend aus Molekülen und Metallatomen/-clustern, wird durch Tempern hervorgerufen. Hieraus lässt sich schließen, dass das amorphe Netzwerk bei RT kinetisch gefangen ist. Der zweite Teil präsentiert die Oberflächensynthese von 2D-Polymeren mittels verschiedener Kupplungsreaktionen. Die resultierenden 2D-Materialien sind durch kovalente Bindungen stabilisiert, wodurch sie resistenter gegenüber äußeren Einflüssen sind. Zu Beginn wird die Ullmann-Kupplung auf Au(111) näher betrachtet. Durch Tempern debromiert das Precursor-Molekül 1,3,5-Tris(4-bromophenyl)benzol (TBPB) und Polyphenylen bildet sich. Um den Einfluss des Metallsubstrates auf die Dehalogenierung näher zu beleuchten, wird eine Monolage hexagonales Bornitrid (h-BN) und Graphen auf Ni(111) gewachsen. Auf beiden Oberflächen bildet TBPB dichtgepackte Inseln, die durch Halogenbindungen stabilisiert sind. Auf reinem Ni(111) dominiert die Substrat-Molekül-Wechselwirkung, wodurch sich Strukturen ohne Fernordnung bilden. Durch Tempern findet auf beiden passivierten Oberflächen eine Dehalogenierung statt und es bilden sich 2D-Nanostrukturen. Auf reinem Ni(111) hingegen zersetzen sich die Precursor-Moleküle lediglich. Die experimentellen Temper-Temperaturen stimmen mit theoretischen Debromierungsbarrieren überein, die durch DFT ermittelt wurden. Weiterhin wird ein Beispiel für die maßgeschneiderte Herstellung von 2D-Strukturen mittels entsprechend funktionalisierter Precursor-Moleküle vorgestellt. Terminale Alkine mit einem Triazinkern reagieren auf Au(111) via Glaser-Kupplung und Cyclotrimersierung zu Stickstoff dotierten 2D-Polymeren. Zum Schluss wird eine umfassende Untersuchung der Decarboxylierung als Oberflächenreaktion des Precursor-Moleküls 1,3,5-Tris(4-carboxyphenyl)benzol (TCPB) auf Cu(111) präsentiert. Bei RT deprotoniert TCPB auf Cu(111) und bildet kompakte Inseln mit einer  $3\sqrt{3} \times 3\sqrt{3} R30^\circ$  Überstruktur. Die Inseln sind durch ionische Bindungen zwischen deprotonierten und (teilweise) negativ geladenen O- und H-Atomen benachbarter Moleküle stabilisiert. Durch Tempern kann eine Decarboxylierung induziert werden und es bilden sich 2D-Nanostrukturen. CO<sub>2</sub> verlässt hierbei als Nebenprodukt die Oberfläche. Zusätzlich wurde mittels STS das niedrigste unbesetzte Molekülorbital (LUMO) untersucht. Das LUMO des 2D-Polymers ist gegenüber dem LUMO des Monomers destabilisiert, obwohl das  $\pi$ -Elektronensystem im Polymer weitreichender ist. Die Decarboxylierung hat einen größeren Einfluss auf die Energieposition des LUMO. DFT-Berechnungen der Modellverbindung Biphenyl-4-carboxylsäure untermauern dies.

**Stichwörter:** *Homoepitaktisches Wachstum, Selbstassemblierung, Amorphes metallorganisches Koordinationsnetzwerk, Kovalente Kupplungsreaktion, Ullmann-Kupplung, Glaser-Kupplung, Cyclotrimersierung, Decarboxylierung, HOMO/LUMO Lücke, Poröses Polymer, Hexagonales Bornitrid, Graphen*

# Contents

<b>Acknowledgements</b>	<b>i</b>
<b>Abstract (English/Deutsch)</b>	<b>iii</b>
<b>List of Figures</b>	<b>ix</b>
<b>1 Introduction</b>	<b>1</b>
<b>2 Experimental Techniques</b>	<b>5</b>
2.1 Scanning Tunneling Microscopy . . . . .	5
2.1.1 Quantum Tunneling . . . . .	7
2.1.2 Bardeen's Tunneling Theory . . . . .	8
2.1.3 Tersoff-Hamann Model . . . . .	10
2.1.4 Scanning Tunneling Spectroscopy . . . . .	11
2.2 Photoelectron Spectroscopy (PES) . . . . .	12
2.3 Experimental Apparatus . . . . .	16
<b>3 Synthesis and Characterization of Non-Covalent 2D Structures</b>	<b>21</b>
3.1 Homoepitaxial Growth on Ag(100) in Presence of an Organic Surfactant	21
3.2 Tip-Induced Finger Formation on Ag(100) . . . . .	26
3.3 Amorphous 2D Metal-Organic Coordination Network . . . . .	31
3.3.1 Synthesis of an Amorphous 2D MOCN . . . . .	32
3.3.2 Characterization of Amorphous 2D MOCN . . . . .	34
3.3.3 Thermodynamics of Phase Segregation . . . . .	40
<b>4 Synthesis and Characterization of 2D Covalent Nanostructures</b>	<b>45</b>
4.1 2D Nanostructures via On-Surface Ullmann Coupling . . . . .	46
4.1.1 2D Polymer Formation on Au(111) . . . . .	47
4.1.2 Halogenated Molecules (TBPB) on Ni(111) . . . . .	49
4.1.3 Covalent Coupling on Ni(111) Supported Hexagonal Boron Nitride and Graphene . . . . .	50
4.2 Homo-(Glaser)-Coupling and Cyclotrimerization of Alkynes on Au(111)	62

## Contents

---

4.2.1	Homo-(Glaser)-Coupling of Arylalkynes . . . . .	63
4.2.2	Cyclotrimerization of Terminal Alkynes . . . . .	65
4.3	2D Polymer Synthesis via On-Surface Decarboxylation Reaction . . . . .	66
4.4	Electronic Properties of 2D Nanostructures . . . . .	75
<b>5</b>	<b>Conclusions and Perspectives</b>	<b>81</b>
5.1	Conclusions . . . . .	81
5.1.1	Non-Covalent 2D materials . . . . .	81
5.1.2	On-Surface Synthesis of Covalent Nanostructures . . . . .	82
5.2	Perspectives . . . . .	83
5.2.1	Atomically Thin 2D Heterostructures . . . . .	83
	<b>Bibliography</b>	<b>100</b>
	<b>Curriculum Vitæ</b>	<b>101</b>

## List of Figures

2.1	Schematic view of sample–tip tunnel junction and sketch of the working principle . . . . .	6
2.2	Sketch of quantum tunneling . . . . .	8
2.3	Relation between energy levels in photoelectron spectroscopy measurements . . . . .	13
2.4	Sample XPS and UPS spectra of clean Cu(111) . . . . .	14
2.5	Chemical shifts of O 1s core levels . . . . .	15
2.6	Photograph of the experimental apparatus . . . . .	17
2.7	Drawings and photograph of Besocke ‘Beetle’ type STM head . . . . .	18
3.1	STM images of Ag(100) covered with sub-monolayer TPA at RT . . . . .	22
3.2	STM image after homoepitaxial Ag growth on Ag(100) in presence of TPA	23
3.3	STM images of Ag vacancies covered with TPA . . . . .	25
3.4	STM images of Ag(100) after Mg deposition . . . . .	27
3.5	STM images of Ag(100) after Mg and TPA deposition and tip-induced finger formation . . . . .	29
3.6	Phase diagram which shows free energy against temperature of cBTBT and Fe on Ag(111) . . . . .	31
3.7	Chemical structure of cBTBT and STM image of its self-assembly on Ag(111) . . . . .	32
3.8	STM images of amorphous metal-organic coordination network . . . . .	34
3.9	Pair correlation functions of four different 2D networks . . . . .	36
3.10	STM images after phase segregation of amorphous cBTBT–Fe network	39
4.1	Sketch of on-surface Ullmann coupling reaction . . . . .	46
4.2	STM images of 2D polymer formed by reaction of TBPB on Au(111) . . .	48
4.3	STM image of TBPB on bare Ni(111) at RT . . . . .	49
4.4	STM images of TBPB on bare Ni(111) after different annealing temperatures . . . . .	50
4.5	STM images of clean h-BN/Ni(111) . . . . .	51

## List of Figures

---

4.6	STM images of TBPB on h-BN/Ni(111) and model of halogen-bonded dimer . . . . .	52
4.7	STM images of reaction products of TBPB on h-BN/Ni(111) . . . . .	53
4.8	STM images of clean graphene grown on Ni(111) . . . . .	55
4.9	STM images of self-assembly of TBPB on graphene/Ni(111) . . . . .	56
4.10	STM images of oligomers of TBPB on graphene/Ni(111) . . . . .	58
4.11	With Arrhenius equation calculated reaction rates for debromination on h-BN/Ni(111) and graphene/Ni(111) . . . . .	59
4.12	Debromination reaction pathway of bromoenzene on h-BN/Ni(111) and graphene/Ni(111) . . . . .	61
4.13	Reaction scheme of Glaser-Hay coupling and cyclotrimerization of terminal alkynes . . . . .	62
4.14	Glaser-Coupling of TEPT on Au(111) . . . . .	63
4.15	Cyclotrimerization of TEPT on Au(111) . . . . .	65
4.16	Self-assembly of TCPB on Cu(111) at RT . . . . .	67
4.17	LEED pattern of Cu(111) and TCPB on Cu(111) at RT. . . . .	68
4.18	STM images of reactions products of TCPB on Cu(111) . . . . .	69
4.19	Reaction products of TCPB on Cu(111) after annealing . . . . .	70
4.20	X-ray photoelectron spectroscopy measurements of TCPB on Cu(111) .	71
4.21	DFT calculated reaction pathway of decarboxylation of model compound biphenyl-4-carboxylic acid on Cu(111) . . . . .	73
4.22	XPS C 1s spectra of multilayers of TCPB on Cu(111) . . . . .	74
4.23	XPS O 1s spectrum of multilayers of TCPB on Cu(111) . . . . .	75
4.24	Scanning tunneling spectroscopy of TCPB and its decarboxylated polymer	76
4.25	UPS photoemission spectra of TCPB multilayers . . . . .	78
5.1	Sketch of in-plane atomically thin heterostructure consisting of graphene and porous graphene and gas-phase DFT calculated band structures of both materials . . . . .	84
5.2	STM images of h-BN islands and 2D nanostructures on Cu(111) . . . .	86



# 1 Introduction

Materials built up by non-covalent bonds such as metal-ligand interactions, hydrogen bonding, van der Waals interactions, or electrostatic forces are of particular interest because the interplay of different interactions and various coupling and molecular recognition schemes enables the direct control of topology and functionality of the material. Additionally, the huge abundance of different molecules opens the way towards novel functional materials with unprecedented physical and chemical properties. As bulk materials change dramatically their physical and chemical properties when the size of the material is sufficiently reduced, the reduction of size turns old well-known materials into ‘new materials’ with new properties. It is thus the task of nano- and materials science to discover and explore new materials with novel and interesting properties leading to technological advances. Nanoscience is the term that comprises the study and investigation of objects with dimensions smaller than 100 nm.

With the birth of the Scanning Tunneling Microscope (STM) in 1981 [1, 2] surface science had received new attention. Single atoms and molecules on well-defined metallic surfaces could be investigated. [3–5] In particular, two-dimensional (2D) materials built up by non-covalent bonds could be studied on the atomic level to obtain fundamental insight into self-ordering and -assembly phenomena. Only the understanding on an atomic scale allows for designing and tuning novel materials with desired and unprecedented properties on a macroscopical scale. Metal–organic coordination networks (MOCNs) consisting of metal atoms as centers and organic molecules as ligands constitute an interesting class of non-covalent 2D materials due to promising properties and applications for instance in molecular electronics, host-guest chemistry, sensors, etc. [6, 7] However, 2D materials relying on supramolecular chemistry have limited stability which restricts their possible application.

2D covalently bonded materials constitute an auspicious alternative due to the in-

trinsically increased stability of covalent bonds. In particular since the discovery of one atom thick graphene sheets in 2004, [8] 2D materials such as MoS<sub>2</sub> [9] or phosphorene [10] have been subject of intense research. Their peculiar electronic properties [11] turn them into potential materials for applications in optoelectronics, catalysis [12] and supporting membranes. [13] In principal, the number of distinct organic 2D materials which can be fabricated is as high as for supramolecular structures. Due to the high abundance of different organic precursor molecules in conjunction with various on-surface coupling reaction schemes, a quasi-infinite number of diverse tailor-made organic 2D materials can be fabricated. Consequently, the structural and electronic properties of 2D polymers can be tuned to a great extent. [14–17] In addition, semiconductive 2D polymers, [18, 19] half-metals suitable for regular ordering of magnetic metal centers, [20] and 2D polymers as catalysts [21] have been theoretically investigated. Despite the myriad theoretical studies on 2D polymers, however, only few experimental investigations of their electronic properties are available. [22, 23] In contrast, throughout the last decade the library of on-surface synthesis protocols has increased immensely. [24–29] Still, almost all 2D polymers lack long-range order and crystallinity due to the irreversibility of the covalent bond formation process. Hierarchical growth concepts can improve the quality of 2D polymers. [30] However, they cannot overcome this inherent issue of covalent bond formation and the growth of long-ranged, crystalline organic 2D polymers is a challenge which has to be met in future. In addition to synthesis protocols, the electronic properties need also to be addressed to provide valuable insights into the interplay between structural and electronic properties and for the design of 2D polymers with tailored electronic structures. Since 2D polymer synthesis takes place on metal substrates acting as heterogeneous catalyst the intrinsic electronic properties of free-standing 2D polymers are generally not easily accessible. Post-growth procedures such as iodine intercalation [31] have already proved to be suitable for decoupling. In addition, the direct synthesis of 2D polymers on decoupling layers represents an alternative and is addressed in this work.

This thesis is divided into two parts. The first part deals with non-covalent 2D structures. It presents the synthesis and statistical analysis of an amorphous MOCN and it is instructively shown how the amorphous MOCN phase segregates at elevated temperatures exemplifying the limited stability of 2D supramolecular materials. The second part addresses covalently bonded 2D materials. The synthesis of 2D nanostructures on non purely metallic substrates is presented and the possibility of tailoring the 2D polymer by using a specially functionalized precursor molecule is demonstrated. In addition, the electronic properties of 2D nanostructures are studied on a single-molecule level by means of scanning tunneling spectroscopy (STS). In detail, the thesis is organized as follows:

---

In Chapter 2 the experimental techniques used in this thesis are elucidated. The basic theory behind the principle of STM and Photoelectron Spectroscopy (PES) are explained with the aid of experimental data. While STM gives very local information at the atomic and molecular level, the spatially averaging technique PES gives information about chemical species on the surface. In addition, the experimental apparatus (Ultra-High Vacuum (UHV) chamber, sample preparation methods, molecular and metal evaporator, etc.) used throughout this thesis is introduced and described.

Chapter 3 presents non-covalent 2D nanostructures. First, Ag growth on Ag(100) is shown to be influenced by the presence of self-assembled islands consisting of carboxylic acids. The technologically important terephthalic acid (TPA) was used as carboxylic acid. Furthermore, tip-induced step-edge manipulation resulting in finger-formation along step-edges of the Ag(100) surface in the presence of magnesium (Mg) atoms and TPA is investigated. Finally, the synthesis and thermal stability of an amorphous MOCN is analyzed and described while its segregation at elevated temperatures is characterized and explained by thermodynamic considerations.

Chapter 4 describes the formation and characterization of 2D covalent networks which are formed via different on-surface coupling reactions inspired mainly by organic solution chemistry. The on-surface Ullmann coupling, surface-assisted Glaser coupling and on-surface decarboxylation reaction are explored and described in further detail. Furthermore, since studies in literature are dominated by the on-surface synthesis on well-defined metal surfaces, the on-surface Ullmann coupling reaction is also studied on atomically thin decoupling layers such as hexagonal boron nitride (h-BN) and graphene. The one-atom thick layers were grown on Ni(111) and it is shown that 2D covalent nanostructures can also be formed on non purely metallic surfaces. On bare Ni(111) the precursor molecules merely decompose and no polymers can be formed. The electronic properties of 2D covalent polymers are also accessed by means of STS, which provides insights on a local (molecular and atomic) level.

Finally, Chapter 5 summarizes the thesis and gives an outlook for some prospective experiments. The fabrication and advantages of heterostructures consisting of graphene and 2D polymers are introduced.



## 2 Experimental Techniques

In this chapter the experimental techniques, their theoretical background and the experimental apparatus used throughout this thesis are presented. To begin with the theoretical background of the Scanning Tunneling Microscope (STM) is elaborated in further detail. Subsequently, the principles of the complementary space averaging technique photoelectron spectroscopy (PES) is illuminated and finally the principal experimental chamber and its various facilities are presented.

### 2.1 Scanning Tunneling Microscopy

This section covers the basics about the principal tool used as experimental technique in this thesis, the STM.

On December 29, 1959 the physicist Richard Feynman gave a lecture at an American Physical Society meeting at Caltech. The title of this lecture was 'There's Plenty of Room at the Bottom: An Invitation to Enter a New Field of Physics' [32] and Feynman considered in this lecture the possibility of direct manipulation of individual atoms and molecules. At that time, however, his considerations did not attract much attention: Only in 1981 Gerd Binnig, Heinrich Rohrer and E. Weibel presented the successful completion of their idea of the STM [1] and in 1986 it earned them the Nobel Prize in Physics. [2] It enabled researchers to follow through with Feynman's idea to observe and manipulate single atoms.

The STM consists of a sharp metallic tip that approaches vertically a flat conducting sample and is laterally scanned along the surface by piezoelectric actuators (indicated by black arrows in Fig. 2.1 a). Once both electrodes (sample and tip) are in contact a current can flow upon applying a voltage. However, already at a very small distance between sample and tip (some Å apart from each other), a tiny current (in the range of

## Chapter 2. Experimental Techniques

nanoamperes) can flow (indicated by the dashed lines in Figure 2.1 a). This so-called tunneling current is based on quantum tunneling and can be explained and described by quantum mechanics. Its theoretical description will be presented in the following sections. As it will be shown, the tunneling current depends exponentially on the small distance between sample and tip, which is a prerequisite for the high resolution of STM. Due to this dependence, only the terminating atom of the tip is significantly contributing to the tunneling current.

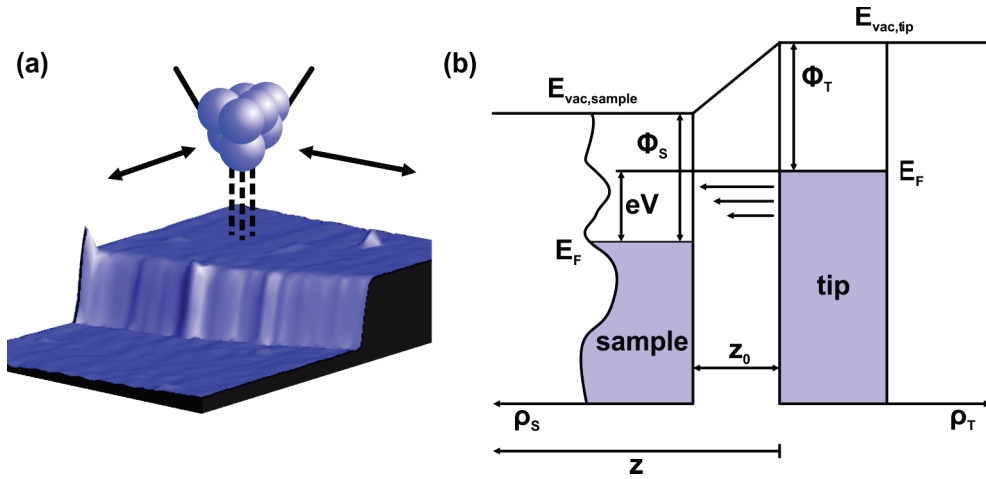


Figure 2.1: (a) Schematic view of a sample–tip tunnel junction. The tip is laterally scanned over the surface. The tunneling electrons flow between the terminating tip atom and the surface (indicated with dashed lines). The surface is a 3D plot of an experimentally obtained Cu(111) surface exhibiting a step-edge and some adsorbates. (b) Sketch of the tunneling process. A bias voltage  $V$  is applied to the sample, which shifts the Fermi energy  $E_F$  by  $eV$  relative to the Fermi energy of the tip. The electrons can tunnel through the vacuum (width  $z_0$ ) from occupied states from the tip (constant density of states  $\rho_T$ ) into empty states in the sample (density of states denoted by  $\rho_s$ ). Note that electrons close to the Fermi energy of the tip contribute most to the tunneling current (indicated by the lengths of black arrows) due to the tunneling matrix element  $M$ .

There are two main operation modes in STM. First, in the constant-current mode the tip is laterally scanned over the surface while the tunneling current is held constant at a set-point current  $I_0$ . Depending on the lateral position of the tip the tunneling current can deviate from  $I_0$ . In order to keep the current constant at  $I_0$  the distance between sample and tip has to be adjusted with the aid of a feedback loop. In the second, constant-height, mode the tip is simply scanned laterally over the surface while the tunneling current is recorded as a function of its lateral position  $I(x, y)$ . The distance between sample and tip is held constant at some position  $z_0$ . This is

usually accomplished by switching off the feedback loop. Images can be acquired faster in the constant-height scanning mode due to the needlessness of the feedback loop. However, if the surface is not flat enough there is the risk of crashing the tip into something on the surface that is higher than the previously set constant sample-tip distance  $z_0$ .

### 2.1.1 Quantum Tunneling

The basic principle behind the working mechanism of a scanning tunneling microscope lies already in its name. The quantum mechanical phenomenon where a particle possessing the energy  $E$  can conquer an energetic barrier  $V_0$  even though its energy  $E$  is smaller than  $V_0$ , that is  $E < V_0$ , is called *quantum tunneling*. Due to the wave-particle duality particles can also be described as waves with De Broglie's wavelength of  $\lambda = \frac{h}{p}$ , where  $h$  is Planck's constant and  $p$  the momentum of the particle. Therefore the particle's wavefunction can penetrate the energetic barrier even though it is  $E < V_0$ .

To understand quantum tunneling and the working principle of STM, Figure 2.2 shows schematically a tunneling junction consisting of tip, vacuum region and sample (from left to right). The vacuum region is approximated by a step barrier with width  $d$  and height  $V_0$ . The Schrödinger equation for this one-dimensional (1D) problem reads

$$\left( -\frac{\hbar^2}{2m} \frac{d^2}{dz^2} + V(z) \right) \psi(z) = E\psi(z), \quad (2.1)$$

where  $m$  is the mass of the particle and  $\hbar$  the reduced Planck constant.  $V(z)$  is  $V_0$  within the barrier and zero outside. The solution of this problem can be found in basic quantum mechanics textbooks. [33, 34] The interesting magnitude is the transmission probability, that is the probability of finding the particle behind the barrier depending on its energy  $E$ . After using the continuity condition on the wavefunction and its derivative for all three regions (tip, vacuum and sample) the result is

$$P_T(E) = \frac{1}{1 + V_0^2 (4E(V_0 - E))^{-1} \sinh^2(\kappa d)}, \quad (2.2)$$

where  $\kappa = \sqrt{2m(V_0 - E)/\hbar^2}$ . It is visible that even for the case of  $E < V_0$  the transmis-

## Chapter 2. Experimental Techniques

sion probability  $P_T(E)$  stays finite. In case of  $\kappa d \gg 1$ , the transmission probability simplifies to

$$P_T(E) \propto e^{-2\kappa d}. \quad (2.3)$$

This is the important *exponential dependence* on the barrier thickness  $d$  which means that the tunneling current (in case of charged particles) depends exponentially on the tip-sample distance and even a small change in barrier width  $d$  changes the tunneling current significantly. Furthermore, it implies that only the atom which terminates the tip contributes to the tunneling current and thus allowing for the high resolution of STM. Additionally, Figure 2.2 shows the wavefunction corresponding to the tunneling particle (with energy  $E < V_0$ ). Before (tip) and after (sample) the vacuum barrier the wavefunction of the particle has the same frequency, that is the energy is conserved (elastic tunneling). The amplitude of the wavefunction after the barrier is reduced, however, which represents the reduced probability for the particle to appear behind the barrier.

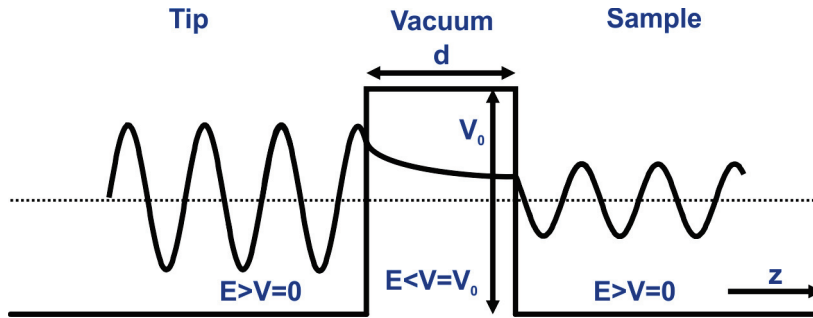


Figure 2.2: Sketch of quantum tunneling of a particle through a barrier of height  $V_0$ . Incident wavefunction with energy  $E > V$  can penetrate a classically forbidden barrier, where it is  $E < V_0$ , due to quantum tunneling. The tunneling process conserves energy (the frequency is the same for the wavefunction after the barrier). The wavefunction's amplitude behind the barrier is smaller revealing the reduced probability of finding the particle there.

### 2.1.2 Bardeen's Tunneling Theory

Bardeen's tunneling theory, also called the transfer Hamiltonian formalism, is a first-order time-dependent perturbation theory. However, it differs from the standard perturbation theory where usually an external field acts as perturbation driving the whole system out of equilibrium. Instead of solving the Schrödinger equation of the



combined system (whole tunneling junction), Bardeen divided it into two subsystems (two electrodes, the sample and the tip) separated by a vacuum region and solved the stationary Schrödinger equations for each subsystem (see Fig. 2.1 b). This is significantly simpler than solving the Schrödinger equation for the total system. When the stationary Schrödinger equation for each subsystem is solved the transmission rate of electrons going from one electrode to the other can be obtained by first-order time-dependent perturbation theory. Bardeen found that the amplitude of electron transfer (tunneling matrix element  $M$ , see its definition below) can be calculated by a surface integral of the unperturbed wavefunctions of each subsystem. The surface integral is an integral over a separation surface which is simply a surface (plane) lying entirely within the vacuum (barrier) region and its exact position in-between the two electrodes does not affect the results significantly.

As a result of Bardeen's tunneling theory the total (net) tunneling can be written as a sum over the discrete eigenstates of sample  $E_\mu$  and tip  $E_\nu$  as

$$I = \frac{4\pi e}{\hbar} \sum_{\mu\nu} [f(E_\mu - E_F) - f(E_\nu - E_F)] |M_{\mu\nu}|^2 \delta(E_\nu - E_\mu - eV), \quad (2.4)$$

where  $f(E) = (1 + \exp[(E - E_F)/(k_B T)])^{-1}$  is the Fermi-Dirac distribution, which gives the probability of occupation of a state with energy  $E$  at temperature  $T$ .  $E_F$  is the Fermi energy and  $k_B$  Boltzmann's constant.  $V$  is the voltage applied between sample and tip and  $e$  is the elementary charge. Therefore  $eV$  corresponds to the relative energy shift of the Fermi levels in sample and tip, see Fig. 2.1 b.  $M_{\mu\nu}$  is the tunneling matrix element and it is defined by

$$M_{\mu\nu} = \frac{\hbar^2}{2m} \int_S (\psi_\mu \nabla \chi_\nu^* - \chi_\nu^* \nabla \psi_\mu) \cdot d\vec{A}. \quad (2.5)$$

This surface integral is the integral over a separation surface  $S$  lying entirely within the vacuum region.  $\psi_\mu$  and  $\chi_\nu$  are the eigenfunctions of each subsystem, sample and tip, respectively. ( $m$  is the electron mass.)

In literature it is also often found the integral form of the total (net) tunneling current. Replacing the summation in Eq. 2.4 by an integral over energies and using the density of states (DOS) of sample  $\rho_S$  and tip  $\rho_T$  leads to

$$I = \frac{4\pi e}{\hbar} \int_{-\infty}^{\infty} [f(E_F - eV + \epsilon) - f(E_F + \epsilon)] \rho_T(E_F - eV + \epsilon) \rho_S(E_F + \epsilon) |M|^2 d\epsilon \quad (2.6)$$

## Chapter 2. Experimental Techniques

---

Furthermore, if the density of states of both electrodes, that is, sample and tip, does not change appreciably near the Fermi energy in the range of applied bias voltages, the tunneling current (Eq. 2.4) can be written as

$$I \propto \frac{2\pi e^2}{\hbar} |M_{\mu\nu}|^2 \rho_S(E_F) \rho_T(E_F) V \quad (2.7)$$

Finally, in order to be aware of the limitations of Bardeen's tunneling theory, the main assumptions of it are summarized. Firstly, the electron tunneling is treated as one-particle process, that is, mutual interaction between electrons during tunneling is neglected. This approximation holds in the small tunnel current regime, where only seldom electrons are tunneling. Secondly, hybridized states between tip and sample wavefunctions are not considered; only the eigenfunctions of tip and sample and their superposition are available and represent a complete set of eigenfunctions. Additionally, it is assumed that the eigenfunction of the two subsystems, sample  $\psi_\mu$  and tip  $\chi_\nu$ , are *approximately orthogonal* in a sense that  $\int \psi_\mu^* \chi_\nu d^3r \cong 0$ . While Bardeen's tunneling theory describes the tunneling process in STM theoretically quite well, there is still a lack of practical applicability because the density of states of the tip  $\rho_T$  as it appears in Eq. 2.6 is generally not known. The next section will present an approximation to circumvent this obstacle.

### 2.1.3 Tersoff-Hamann Model

Only around one year after the invention of the experimental apparatus STM, J. Tersoff and D.R. Hamann formulated a model based on Bardeen's tunneling theory. [35, 36] As it can be seen from Eq. 2.6 the tunneling current is a convolution of the states of the sample and the tip. The states of the tip are usually not known and therefore Tersoff and Hamann proposed an approximation in which the tip properties are approximated in such a way that the results do not depend on it anymore. They modeled the tip as a geometrical point and consequently, the tunneling current and thus STM image connects only to a property of the surface.

The Tersoff-Hamann model has proven to be extraordinary valuable in interpreting and understanding STM images with characteristic feature sizes greater than 1 nm. It could very well reproduce experimental data of linescan profiles of superstructures of surface reconstructions, scattered waves of surface states (Friedel oscillations), as well as defects, adsorbates and substitution atoms on the surface. However, it predicts the size of atomic-scale features ( $\approx 0.3$  nm) to be too small ( $\approx 1$  pm) so one has to keep in mind that the STM image experimentally is still a convolution of sample and tip electronic states.

According to Bardeen's tunneling theory the tunneling matrix element  $M_{\mu\nu}$  (Eq. 2.5) depends only on the wavefunctions of sample and tip at the separation surface. By assuming a spherically symmetric tip wavefunction, s-wave type, Tersoff and Hamann could evaluate Bardeen's tunneling matrix element  $M_{\mu\nu}$ . As integration surface they chose the sample surface. They found that the matrix element is proportional to the sample wavefunction  $\psi(\vec{r})$  read out at the center of the curvature of the tip,  $\vec{r}_0$ , that is  $M \propto \psi(\vec{r}_0)$ . With this result Eq. 2.7 can be written as

$$I \propto |\psi(\vec{r}_0)|^2 \rho_S(E_F) V \propto \rho_S(E_F, \vec{r}_0) V \quad (2.8)$$

If the tip wave function is s-wave like with its origin at  $\vec{r}_0$ , the tunneling current depends only on the *local* density of states (LDOS)  $\rho_S(E_F, \vec{r}_0)$  of the sample evaluated at the position  $\vec{r}_0$  underneath the tip and the Fermi energy  $E_F$ . As an approximation, the STM images can be interpreted as contour plots of the LDOS of the sample at the Fermi level.

### 2.1.4 Scanning Tunneling Spectroscopy

In the previous sections the basic theory behind the working principle of STM was presented. In this section the theoretical background of the possibility to obtain spectroscopic insights into a system with atomic accuracy as a great feature of STM is introduced. Scanning Tunneling Spectroscopy (STS) works as follows. While in STM the tip is scanned in the x-y-plane over the surface of the sample, in STS the tip is placed on top of a feature of interest on the sample surface such as an adatom, a molecule or a step edge. The (bias) voltage applied between sample and tip is then swept over an energy range of interest while the feedback loop is turned off (open feedback), that is the distance between sample and tip does not change and stays constant. With this procedure so-called I/V-curves are obtained and in the following it is shown that the derivative of the tunneling current with respect to the voltage, that is the differential conductance  $dI/dV$ , is proportional to the local density of states (LDOS) of the sample  $\rho_S(E_F, \vec{r}_0)$  (see Eq. 2.8).

With the assumption that the matrix element  $M$  in Eq. 2.6 changes negligibly in the energy range of interest, the density of states of the tip  $\rho_T$  is constant and being at zero temperature, the derivative of Eq. 2.6 with respect to the bias voltage  $V$  becomes [37]

$$\frac{dI}{dV} \propto \rho_T \int_{-\infty}^{\infty} \rho_S(E_F + \epsilon) \delta(E_F - eV + \epsilon) d\epsilon = \rho_T \rho_S(eV - E_F) \quad (2.9)$$

Note the agreement with Eq. 2.8, where it was assumed  $\rho_S(E_F - eV) \approx \rho_S(E_F)$ . Technically, the differential conductance can be obtained by acquiring I-V-curves and

differentiating them or by measuring the derivative of the tunneling current with the Lock-In technique directly. For a detailed derivation and explanation see Ref. [37].

### 2.2 Photoelectron Spectroscopy (PES)

In this section Photoelectron Spectroscopy (PES) is presented. In contrast to Scanning Tunneling Microscopy, which is a local technique due to its possibility of obtaining atomic resolution, PES is an experimental averaging method because it measures sample areas of around  $1 \text{ mm}^2$ . Photoelectron Spectroscopy (PES) is based on the photoelectric effect discovered by Heinrich Rudolf Hertz in 1887. [38] In 1905, approximately 20 years later, Albert Einstein could explain the effect theoretically as a result of light being quantized in form of photons [39] for which he was awarded the Nobel Prize in Physics in 1921. The photoelectric effect describes basically the observation that electrons leave a material upon illumination with electromagnetic light. Photoelectron spectroscopy is roughly divided into two sections depending on the wavelength of light used in the experiments. X-ray photoelectron spectroscopy (XPS) uses x-ray radiation. Laboratory sources most widely applied are Al  $K_\alpha$  and Mg  $K_\alpha$  lines with energies of 1487 eV and 1253.6 eV, respectively. Ultra-violet photoelectron spectroscopy (UPS) uses less energetic photons (between 10 eV and 100 eV) as light source. Commonly, gas discharge tubes are used for this purpose in laboratories. However, synchrotron-based radiation sources with the advantage of a continuous energy range are also frequently at work for photoelectron spectroscopy studies.

Figure 2.3 shows the energy relation between a metallic sample and the spectrometer. The Fermi energies are aligned because sample and spectrometer are in electrical contact. Incoming photons with energy  $h\nu$  trigger the emission of electrons and are detected in the spectrometer with a kinetic energy of

$$E_{\text{kin}} = h\nu - \Phi_{\text{Sp}} - |E_{\text{B}}|, \quad (2.10)$$

where  $|E_{\text{B}}|$  is the absolute value of the binding energy of the electron that was emitted from the material under study. Note that the electrons actually leave the surface with kinetic energy  $E'_{\text{kin}}$  (see Fig. 2.3, left side). However, since the emitted electrons are detected in the spectrometer, the work function of the spectrometer  $\Phi_{\text{Sp}}$  appears in the formula. The binding energy  $E_{\text{B}}$  is element specific and therefore PES can be used to reveal chemical composition of the material or to identify chemical species on the surface.

## 2.2. Photoelectron Spectroscopy (PES)

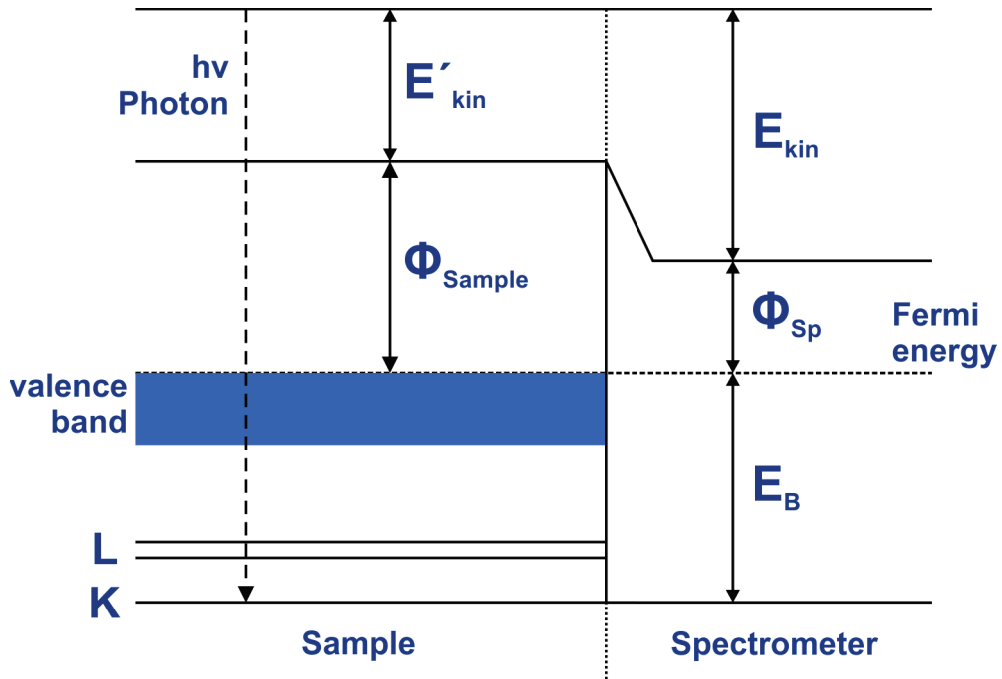


Figure 2.3: Relation between the energy levels of a metallic sample and the spectrometer. The Fermi energies are aligned and the work functions of sample and spectrometer are indicated (here:  $\Phi_{\text{Sample}} > \Phi_{\text{Sp}}$ ). The photons impinging the sample surface have energy  $h\nu$  and the emitted electrons which are detected in the spectrometer have kinetic energy  $E_{\text{kin}}$ . Note that electrons actually leave the sample surface with  $E'_{\text{kin}}$  and due to the work function difference it is measured  $E_{\text{kin}}$  in the spectrometer.

Figure 2.4 a shows a survey scan of a typical XPS spectrum of a clean Cu(111) surface taken with an excitation energy of 1253.6 eV (Mg  $K_{\alpha}$  line). Electrons emitted from 2p, 3s, 3p, and 3d levels can be detected. Note that the 2p core level emission is *spin-split* into two peaks namely  $2p_{1/2}$  and  $2p_{3/2}$  due to *spin orbit coupling*. The indices indicate the total angular momentum  $j_{\pm} = l \pm \frac{1}{2}$ , where  $l$  is the orbital angular momentum quantum number of the core level and the latter is the electron spin. Core level peaks with  $l = 0$  are thus not spin-split. In contrast, core level peaks of p-orbitals have an angular momentum of  $l = 1$  and it hence is  $j_{+} = \frac{3}{2}$  and  $j_{-} = \frac{1}{2}$ . Additionally, *Auger electrons* are observed between 300 eV and 500 eV. Auger peaks are a consequence of a three-electron process in which an electron is emitted by an incoming photon, the resulting hole is refilled by a second electron and the energy that is released by this refilling is transferred to a third electron that leaves the sample as an Auger electron and is detected in the spectrometer. In contrast to primary emitted core level electrons, the kinetic energy of Auger electrons does not depend on the excitation energy.

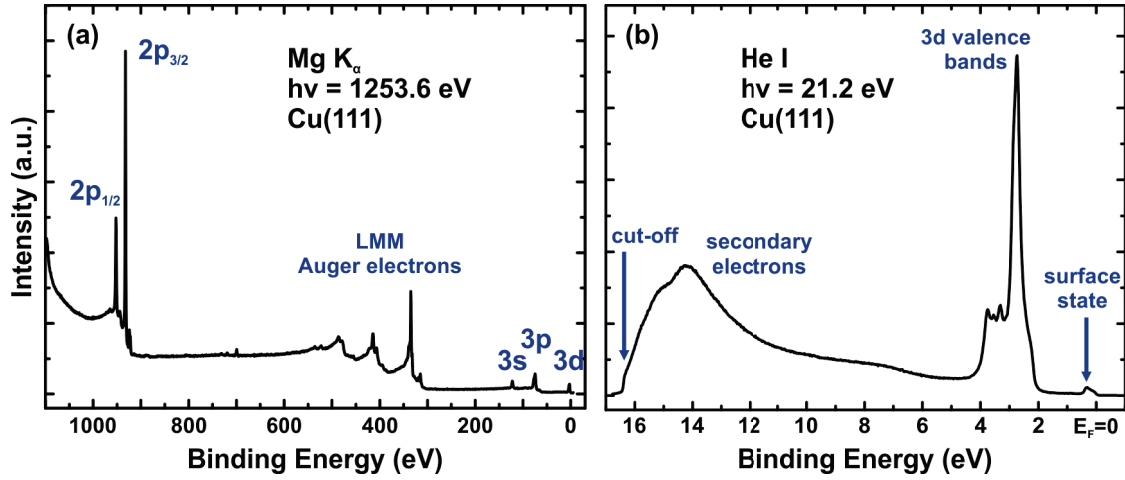


Figure 2.4: (a) Typical XPS spectrum of a clean Cu(111) surface. Excitation source was the Mg  $K_{\alpha}$  line at 1253.6 eV. Besides the primary electron peaks (2p, 3s, 3p and 3d), secondary LMM Auger electron peaks are visible. The 2p core level peak is split into  $2p_{3/2}$  and  $2p_{1/2}$  spin-orbit split states. (b) Typical UPS spectrum of a clean Cu(111) surface with an excitation energy of 21.2 eV (He I  $\alpha$  line). The surface state is visible at approximately 390 meV [40]. The structured 3d valence bands are situated around 2 eV below the Fermi level. The background signal due to secondary electrons is increasing with decreasing kinetic energy and the cutoff around 16.5 eV below the Fermi level marks the point where  $E_{\text{kin}} = 0$ .

Figure 2.4 b shows a typical ultra-violet spectroscopy spectrum of clean Cu(111) taken with an excitation energy of 21.2 eV (He I  $\alpha$  line). While in the XPS spectrum the 3d valence bands were only one peak, in the UPS spectrum they appear structured. In general high energy photons come along with a limitation of resolution. [41] Fig. 2.4 b also reveals the surface state of Cu(111) situated around 390 meV. [40] The broad tail at high binding energies (low kinetic energies) originates from secondary scattered electrons which contribute to the background. The cut-off energy with electrons of zero kinetic energy (approximately at 16.4 eV) can also be recognized. The corresponding work function  $\Phi_{\text{Sample}}$  can be calculated as  $21.2 \text{ eV} - 16.4 \text{ eV} = 4.8 \text{ eV}$ , which is in agreement with 4.94 eV reported in literature. [42] The origin of the small discrepancy lies most likely in the calibration of the work function of the spectrometer  $\Phi_{\text{Sp}}$ . Due to contaminations it can change and needs to be recalibrated from time to time.

Photoelectron spectroscopy is a very surface sensitive technique. At first glance this is counterintuitive because photons (of high energy) penetrate the sample farther than

some nanometers. The surface sensitivity stems from the fact that only electrons near the surface can actually leave the sample due to their small mean free path. [41] The dependence of the mean free path on the kinetic energy of electrons can be described by the *universal curve* with a minimum of 2 Å to 5 Å for kinetic energies between 50 eV and 100 eV. Even at kinetic energies of 1000 eV the mean free path accounts only for around 1 nm to 2 nm. [41]

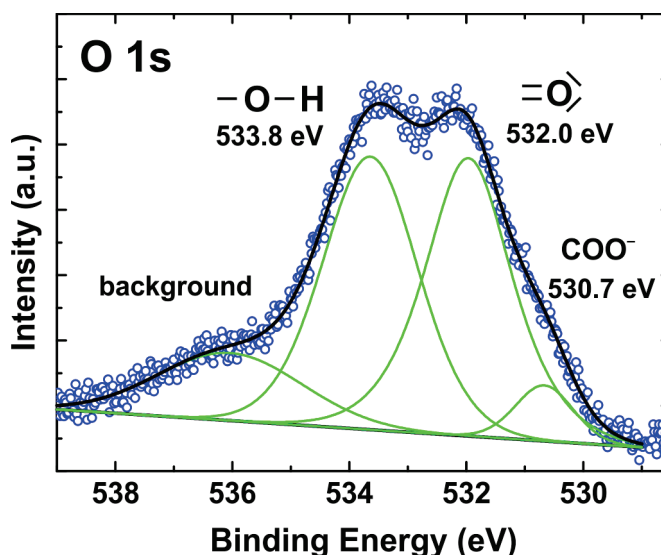


Figure 2.5: Chemical shifts of O 1s core levels in tricarboxylic acid on Cu(111). The chemical shifts arise due to different partial charges on oxygen atoms and electronegativity differences. The lowest partial charge is on oxygen atoms in carboxyl groups (C–O–H) resulting in a high binding energy. Contrarily, the lowest binding energy prevails for oxygen atoms in deprotonated carboxyl groups (COO<sup>-</sup>). Oxygen atoms within carbonyl groups (C=O) constitute an intermediate with mediocre binding energy.

Besides the analysis of chemical composition of samples studied by XPS it allows also for the determination of oxidation and binding states. The binding energies of core levels are not directly involved in bonds but the electronic surrounding of an atom has an influence on the exact energy position of the corresponding core level. Therefore, the so-called *chemical shift* can give information about the chemical environment of an atom, its oxidation or bonding state. An example for the chemical shift and the recognition of different bonding states is shown in Figure 2.5. It presents the 1s core level of oxygen within a carboxylic acid. The peak with a binding energy situated around 533 eV consists of three oxygen atoms each in a different bonding environment. One high binding energy peak corresponding to oxygen in hydroxyl groups (C–O–H), one low binding energy peak corresponding to deprotonated carboxyl groups (COO<sup>-</sup>)



and one peak with intermediate binding energy that can be assigned to oxygen atoms in carbonyl groups ( $\text{C}=\text{O}$ ). The partial charge is lowest on oxygen atoms in hydroxyl groups and thus the binding energy is highest for those atoms. Contrarily, deprotonated carboxyl groups are negatively charged and hence the binding energy is lowest for oxygen atoms in deprotonated carboxyl groups (carboxylates). Oxygen atoms of carbonyl groups inhere some intermediate partial charge and the corresponding peak can be found in between the oxygen of hydroxyl groups and carboxylates.

### 2.3 Experimental Apparatus

In this section the experimental apparatus used during this doctoral thesis is presented. Figure 2.6 shows a photograph of the experiment. It consists of one main chamber with a base pressure of  $1 \times 10^{-10}$  mbar. Sample preparation is carried out in a manipulator which can be linearly moved in the ultra-high vacuum (UHV) chamber. A sputter gun enables sputtering with noble gas ions and the sample is heated via electron bombardment with high-voltage applied to the sample. In this thesis argon (Ar) atoms were used for sputtering. The manipulator can also be cooled with liquid helium or nitrogen. Thermocouples of type K connected to the sample and manipulator allow for easy temperature monitoring during sample preparation. Via a load lock samples and STM tips can be exchanged without venting the system. All STM measurements presented in this thesis were acquired with a tungsten (W) tip which was set to ground (bias is applied to the sample). Additionally, two fast entry mounts facilitate the interchange of loadings of metal evaporators (Omicron) as well as molecular-beam epitaxy evaporators (Dodecon Nanotechnology). A quartz crystal microbalance at disposal allows for calibration of deposition rates. Furthermore, the main chamber is equipped with surface sensitive analysis tools such as Low Energy Electron Diffraction (LEED) for surface structure investigations and Auger Electron Spectroscopy (AES) for chemical characterization of the samples. The Variable-Temperature Scanning Tunneling Microscope (VT-STM) was designed and implemented by Sessi [43] and significantly improved by Krotzky [44] (both are previous PhD students). The STM is based on the Wilson Ho design [45] with a Besocke 'Beetle' type STM head. [46, 47] The STM slightly deviates from Wilson Ho's design. The tip can be exchanged via a tip-exchange tool and the Eddy current damping is not inside the cooling shields (see Fig. 2.7 (a)). The STM can be operated at variable temperatures in the range from 10 K to 300 K with liquid helium and a continuous flow cryostat. In principle, the STM could also be heated up to temperatures slightly higher than room temperature with the aid of the heating element in the cryostat.



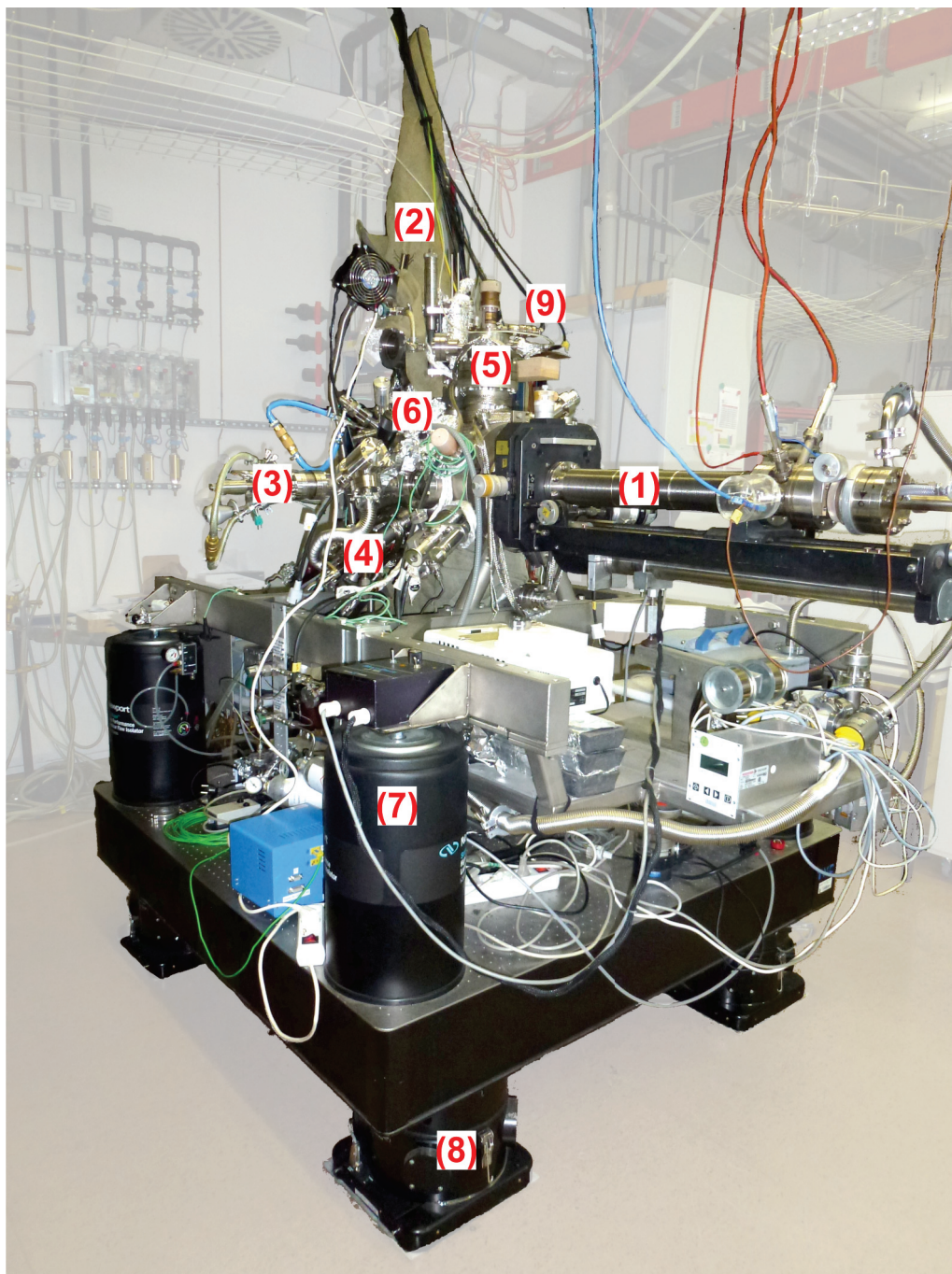


Figure 2.6: Photograph of the experimental apparatus. The main chamber is situated on an optical table and the labels in red are as follows: (1) Manipulator, (2) Loadlock, (3) Evaporator (molecules), (4) E-beam evaporator (metals), (5) Auger, (6) STM, (7) Passive damping, (8) Active damping, (9) Electric cables for STM.

Figure 2.7 depicts a technical drawing of the STM in (a) and the head in (b). Figure 2.7 c

## Chapter 2. Experimental Techniques

shows a photographic image of the Besocke ‘Beetle’ type STM head. The three outer piezos for coarse motion and the inner ‘scanning’ piezo with the tungsten (W) tip are visible. Note that only the outer shield was mounted when this image was taken. Additional information can be found in the theses of Dr. Violetta Sessi [43] and Dr. Sören Krotzky. [44]

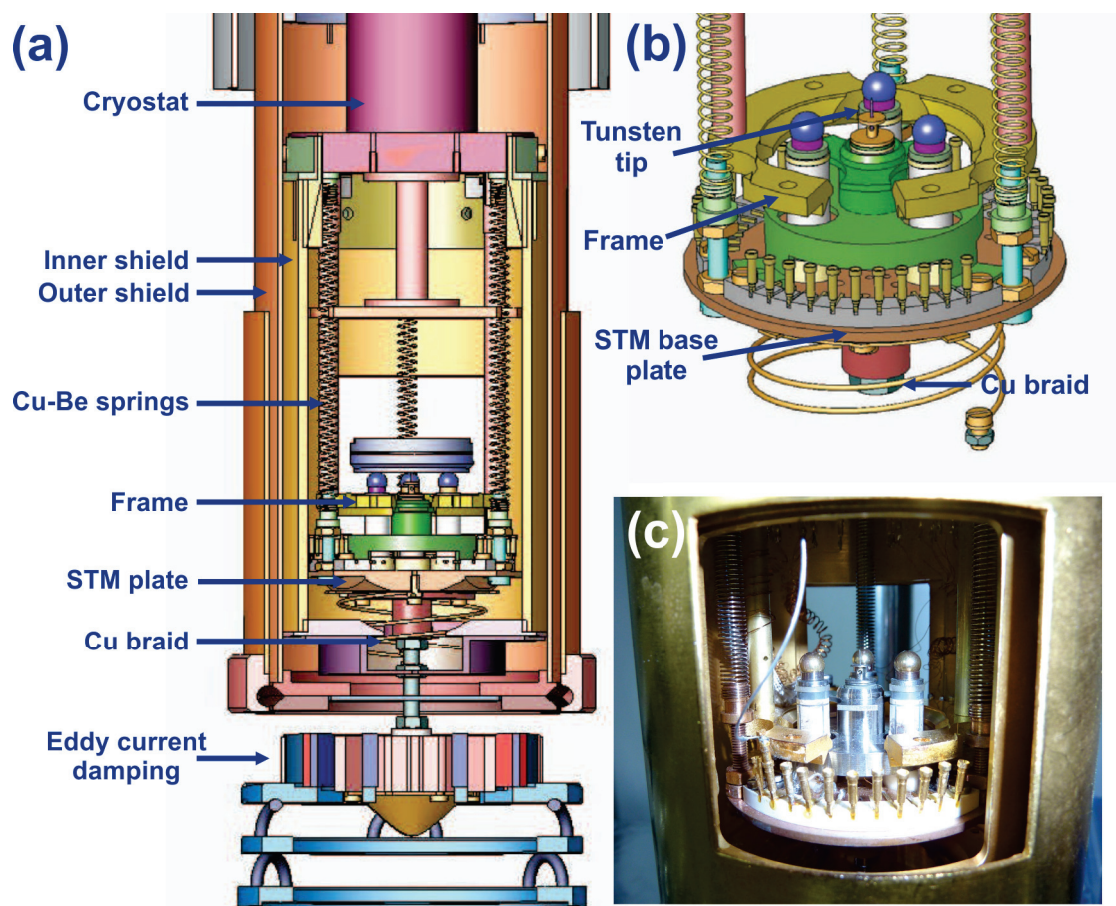


Figure 2.7: (a) Technical drawing of the STM and captions of the main parts. (b) Technical drawing of the Besocke ‘Beetle’ type STM head (without shields). (c) Photograph of the STM head. The three outer piezos for coarse motion and the inner ‘scanning’ piezo with a tungsten (W) tip can be seen.

**XPS and UPS Measurements** All XPS and UPS measurements have been carried out at the in-house facilities at the Max Planck Institute for Solid State Research in Stuttgart. The analysis chamber is equipped with a hemispherical SPECS PHOIBOS 150 energy electron analyzer with an energy resolution of approximately 15 meV. The analyzer axis is normal to the sample surface and the x-ray beam has an incident angle

### 2.3. Experimental Apparatus

---

of approximately  $45^\circ$  relative to the sample surface normal. XPS measurements were performed using photons from a non-monochromatic Mg  $K_\alpha$  source with photon energy of  $h\nu = 1253.6$  eV. UPS data were acquired using monochromatic He I radiation ( $h\nu = 21.22$  eV) from a UV discharge source. The size of the spot on the sample surface accounts approximately for  $1 \text{ mm}^2$ . Prior to XPS and UPS measurements, the samples were similarly prepared as in the STM experiments. A preparation chamber with a base pressure of  $1 \times 10^{-10}$  mbar connected to the analysis chamber (base pressure  $2 \times 10^{-10}$  mbar) via a transfer system with a base pressure of  $1 \times 10^{-9}$  mbar was used for  $\text{Ar}^+$  sputtering (1 keV, 20 min) and annealing at  $500^\circ\text{C}$  (773 K). Besides a thermocouple (type K, chromel-alumel), a pyrometer (LumaSense Technologies, IMPAC IGA 740, sensitivity = 10 %) was used for temperature measurements to guarantee high reproducibility and consistency with sample preparations used for STM measurements. XPS and UPS measurements were performed at room temperature (300 K). The preparation chamber is also equipped with LEED (low-energy electron diffraction) optics which was additionally used to characterize the sample.



## 3 Synthesis and Characterization of Non-Covalent 2D Structures\*

This chapter covers two-dimensional (2D) supramolecular structures stabilized and built up by non-covalent bonds. The first part deals with the self-assembly of a dicarboxylic acid and how its presence on the Ag(100) surface influences the homoepitaxial growth of silver on Ag(100). Subsequently, tip-induced reshaping of step-edges by the deposition of two materials, magnesium atoms as well as dicarboxylic acid molecules, is discussed in further detail and a tentative mechanism explaining the experimental observations is suggested. Finally, an amorphous metal–organic coordination network, formed out of iron (Fe) atoms and dicyano-functionalized organic semiconductor molecules on Ag(111) is presented. This amorphous network phase segregates at elevated temperatures and instructively highlights one major drawback of 2D materials consisting of non-covalent bonds which is their limited stability against temperature.

### 3.1 Homoepitaxial Growth on Ag(100) in Presence of an Organic Surfactant

In this section the homoepitaxial growth in presence of organic molecules is presented. The system under study is Ag on Ag(100), which has been intensively investigated by means of scanning tunneling microscopy, (mathematical) lattice gas models and kinetic Monte-Carlo simulations around the turn of the century. [49–55] The growth of Ag on Ag(100) happens in a layer-by-layer fashion, which means that only after completing the first layer, growth of the second layer sets in. However, when an island of the first layer is large enough second layer growth can already start regardless of the completion of the first layer. This *quasi* layer-by-layer growth leads to kinetic roughening when growing multiple layers. [51, 52] The main reason for this is the

---

\*Parts of this chapter are based on publication #3 [48] of the CV publication list.



### Chapter 3. Synthesis and Characterization of Non-Covalent 2D Structures

presence of an increased diffusion barrier (Ehrlich-Schwöbel barrier [56,57]) for Ag atoms going down a step-edge. Surfactants can alter the magnitude of the Ehrlich-Schwöbel barrier and can thus change the underlying growth mechanism. [58–63] Surfactants are usually impurity atoms such as indium (In) or antimony (Sb) atoms. Usually they are difficult to remove after growth. Here an organic molecule which forms densely packed islands upon deposition on Ag(100) at room temperature (RT) is used as surfactant. Additionally, it desorbs easily from the surface at elevated temperatures and thus does not contaminate the sample.

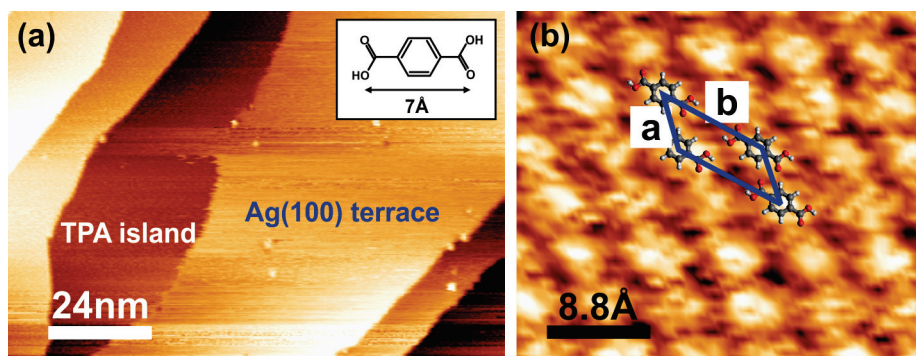


Figure 3.1: STM images after TPA deposition on Ag(100) at RT. (a) Overview STM image. A TPA island running vertically along a step-edge is observed. Clean Ag(100) terraces are also visible ( $U = 0.7\text{ V}$ ,  $I = 0.3\text{ nA}$ ). The inset shows the structural formula of TPA. (b) High-resolution STM image of TPA island. Single molecules are resolved and scaled ball-and-stick models are superimposed ( $U = 0.7\text{ V}$ ,  $I = 0.3\text{ nA}$ ). The unit cell is indicated in blue:  $a = 6.2\text{ Å}$ ,  $b = 9.2\text{ Å}$  and  $\gamma = 40^\circ$ .

Figure 3.1 a shows an overview STM image of Ag(100) after deposition of approximately 0.2 monolayers of terephthalic acid (TPA, 1,4-dicarboxylic acid) on Ag(100) at RT. The inset shows the structural formula of TPA. It consists of a phenyl ring with two carboxylic acids in para positions. The molecules self-assemble upon deposition at RT into densely packed islands. One island is observed with darker contrast in Fig. 3.1 a on a terrace running vertically along the step-edge. Fuzzy features at the island border are assigned to mobile TPA molecules due to low molecule–substrate and molecule–molecule interactions. Free Ag(100) terraces are also visible. Figure 3.1 b presents a high-resolution STM image with molecular resolution. An accordingly scaled ball-and-stick model is superimposed and the unit cell is indicated in blue. The molecules are most-likely still hydrogenated due to the low reactivity of Ag. Benzene-1,3,5-tribenzoic acid starts only deprotonating after annealing at  $150^\circ\text{C}$  (420 K) on Ag(111). [64] The self-assembly is stabilized via hydrogen bonding between hydrogen atoms of hydroxyl groups and oxygen atoms of carbonyl groups building up a

### 3.1. Homoepitaxial Growth on Ag(100) in Presence of an Organic Surfactant

chain-like structure. In addition, the chains are stabilized by hydrogen bonding of hydrogen atoms of the phenyl rings and oxygen atoms of the carbonyl groups of an adjacent TPA molecule. The unit cell accounts for approximately  $a = 6.2\text{\AA}$ ,  $b = 9.2\text{\AA}$  and  $\gamma = 40^\circ$ . These values and the self-assembly pattern are in agreement with values reported for TPA on Au(111). [65]

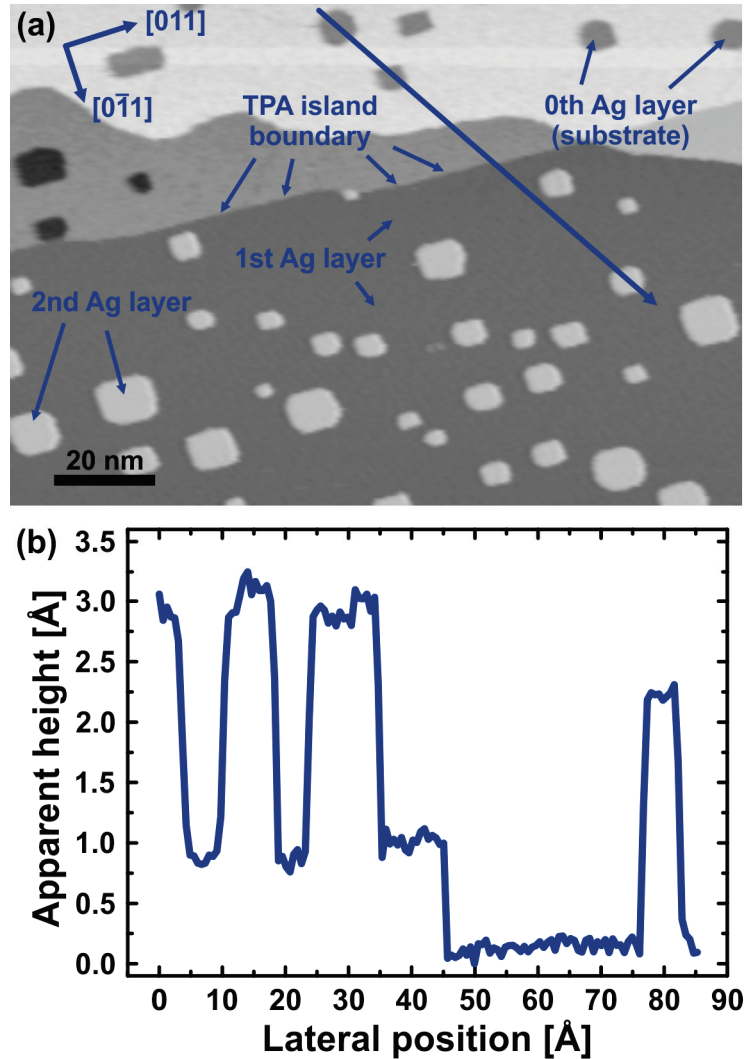


Figure 3.2: (a) STM image after homoepitaxial Ag growth on Ag(100) in the presence of a molecular layer consisting of terephthalic acid (TPA). The molecular layer is covering the top part of the STM image and a step-edge runs roughly in the [001]-direction across the image ( $U = -0.6\text{ V}$ ,  $I = 1.1\text{ nA}$ ). (b) Linescan along the blue line drawn in (a). The apparent height of the molecular layer is approximately  $1\text{ \AA}$ ; the step-edge as well as vacancy and Ag islands appear with a height of roughly  $2.1\text{ \AA}$ .

Now the influence of such TPA islands on the homoepitaxial growth of Ag is discussed.

### Chapter 3. Synthesis and Characterization of Non-Covalent 2D Structures

---

Figure 3.2 a shows an STM image approximately 90 min after the growth of nominally 1.1 layers of Ag on Ag(100). Silver atoms have been deposited at room temperature (RT) in the presence of molecular islands consisting of TPA (nominally 20% coverage). In the upper part of Figure 3.2 a a step-edge is running along the [001] direction. The step-edge is undulated due to the coalescence of Ag islands at the step-edge after growth. [55] While on the free terrace in absence of TPA molecules second layer Ag islands are visible, on the TPA covered area first layer growth has not yet been completed and vacancy islands can be observed. A detailed analysis gives a post-deposition layer coverage of Ag on TPA covered areas of approximately  $\theta_1 = 0.9$  monolayers and on the free terrace the coverage accounts for  $\theta_2 = 0.13$ . The sum of both accounts for a coverage of approximately  $\theta = 1$ . However, the same deposition conditions yield a coverage of approximately  $\theta = 1.1$  monolayers on completely clean Ag(100). Assuming that the Ag deposition beam is homogeneous over the whole sample, the same amount of Ag atoms are arriving on the surface irrespective of whether it is covered with TPA islands or not. However, by inspecting Fig. 3.2 a and as stated above, there is less material (Ag atoms) on the TPA covered area of the Ag(100) surface. This observation can be explained by two possible mechanisms which will be discussed in the following. First, as mentioned, the same amount of Ag atoms is arriving on both areas – TPA covered and clean terraces. Subsequently, Ag atoms can be diffusing on the surface and will eventually nucleate as islands. If Ag atoms and islands are energetically favored on clean Ag(100) terraces there will be a net diffusion from TPA layer to free areas present which will result in less material on TPA covered terraces as observed in the experiment. The second and probably more likely mechanism at work is that the TPA islands reduce the sticking coefficient compared to clean terraces and therefore less Ag atoms are adsorbed on areas with molecules. This is consistent with the observation that nominally 1.1 monolayers were deposited but the total post-deposition coverage accounts only for 1 monolayer. Additionally, if there was a favored net diffusion from molecular islands to free terraces present, one should observe a higher island density or more material close to the border of the TPA islands which is not observed in the experiment (see Fig. 3.2 a). In conclusion, it is more likely, that molecular islands consisting of TPA reduce the sticking coefficient of Ag on Ag(100) and therefore less material is observed on surface areas that are covered with molecules. Figure 3.2 b shows a linescan along the blue line in Fig. 3.2 a. The step-edge as well as vacancy and Ag islands have an apparent height of approximately 2.1 Å. The molecular layer running across the upper part in the STM image of Fig. 3.2 appears with an height of 1 Å. While the molecular island runs across vacancy islands, no TPA molecules are present on top of an Ag island. Since the post-deposition coverage on TPA covered terraces accounts for  $\theta_1 = 0.9\%$  (see Fig. 3.2 a), one could expect that second layer island growth should already set in. However, no second layer islands



### 3.1. Homoepitaxial Growth on Ag(100) in Presence of an Organic Surfactant

can be observed on TPA covered regions (see Fig. 3.2 a). Therefore, tentatively the molecular layer might reduce the Ehrlich-Schwöbel barrier thus making the Ag growth on Ag(100) smoother. However, more detailed experiments and calculations have to be carried out in order to obtain a quantitative value for the barrier. [52, 66, 67]

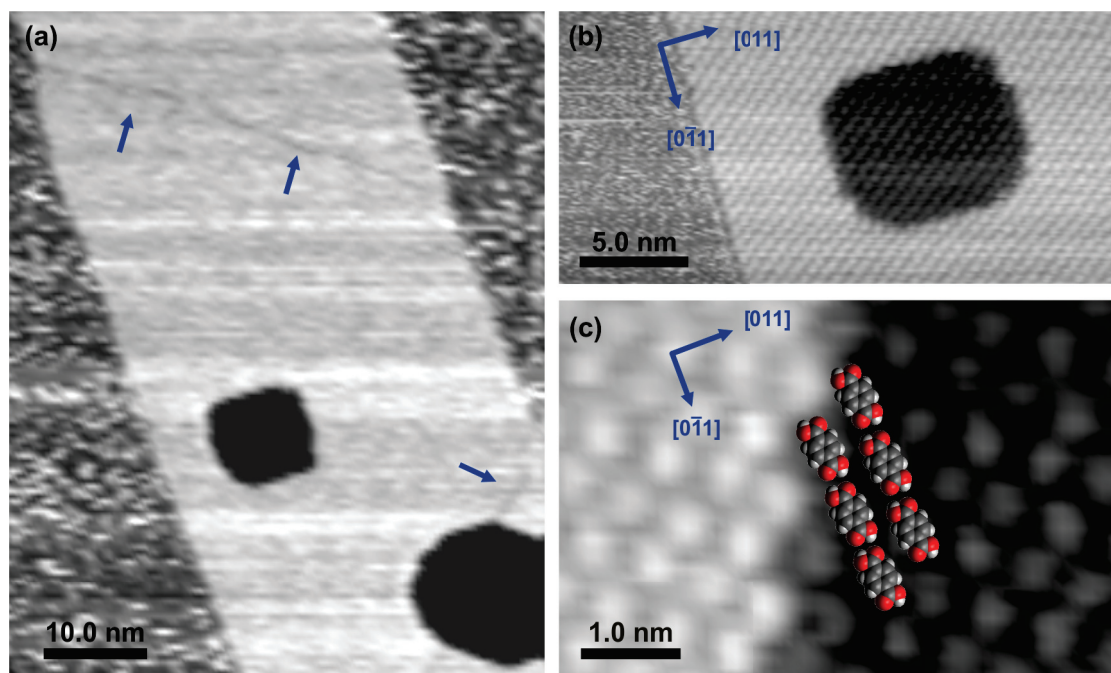


Figure 3.3: STM images of Ag vacancies covered with TPA. (a) Overview STM image of a molecular layer of TPA. Two vacancy islands of different shapes are present. The border of the TPA island runs along the  $[0\bar{1}1]$ -direction. Grain boundaries within the TPA layer due to coalescence of Ag islands during growth are indicated with blue arrows ( $-0.9$  V,  $0.25$  nA). (b) Zoom of square-shaped vacancy island within the molecular layer shown in (a). The self-assembly seems not to be interrupted by the presence of the vacancy islands ( $-0.9$  V,  $0.25$  nA). (c) High-resolution STM image of the hexagonal-shaped vacancy island shown in (a). Single TPA molecules are resolved and run across the vacancy island without being interrupted. Equilibrium directions of square-shaped Ag islands are indicated in blue ( $0.9$  V,  $0.25$  nA).

In the following the influence of homoepitaxial growth on the TPA islands is discussed and whether the TPA self-assembly pattern is altered or islands are disrupted by the arrival of Ag atoms during homoepitaxial growth. Figure 3.3 shows a molecular island with two vacancy islands of different shape. The blue arrows indicate grain boundaries that have formed due to the coalescence of Ag islands underneath the TPA layer. Consistently, the grain boundaries run along the  $[001]$  and  $[010]$  directions.

Fig. 3.3 b and c show a high-resolution STM image of the square-shaped island in (b) and the hexagonal-shaped island in (c). Fig 3.3 c presents also scaled ball-and-stick models of TPA to indicate their adsorption geometry. Interestingly, the arrangement of TPA within the molecular island is not interrupted by the arrival of Ag atoms during deposition, their intercalation and formation of Ag and vacancy islands. Only coalescence of islands leads occasionally to some grain boundaries as observed in Fig. 3.3 a. Moreover, the step-edge of the vacancy island is defined by single molecules and no TPA molecules run across a step-edge. The unit cell of the self-assembly pattern is the same as in Fig. 3.1 b and they form stripes along the equilibrium directions of square-shaped Ag islands,  $[011]$  and  $[0\bar{1}1]$ .

To conclude, the observation of less material on top of TPA covered Ag(100) regions (compared to clean terraces) might be explained by two possible mechanisms. A net diffusion of Ag atoms towards non-covered regions or the more likely mechanism a reduction of the sticking coefficient due to the presence of TPA islands can explain the experimental observations. In addition, Ag atoms intercalate and penetrate the molecular layer at room temperature and the TPA islands are not disrupted or interrupted by the growth of Ag islands underneath except for formation of grain boundaries. The self-assembly islands are stabilized by hydrogen bonds and the unit cell remains the same.

## 3.2 Tip-Induced Finger Formation on Ag(100)

In this section tip-induced finger formation at step-edges of Ag(100) in presence of alkaline earth metal atoms (Mg) and organic molecules (TPA) is presented. TPA, 1-4-dicarboxylic acid, has already been introduced in the previous section. The dicarboxylic acid forms metal-organic coordination networks with a variety of different metal atoms such as the transition metal iron (Fe) [68] or alkali metal sodium (Na). [69] In order to grow a metal-organic coordination network consisting of Mg atoms or ions as metal centers and TPA molecules as ligands, both materials have to be coadsorbed on the surface. TPA on its own forms molecular islands stabilized by hydrogen bonds when deposited on Ag(100) at RTt as presented above. Therefore, Mg deposition on Ag(100) is briefly discussed in the following.

Figure 3.4 a shows an STM image of Ag(100) after submonolayer deposition of Mg at RT. At this temperature Mg grows in the Stranski-Krastanov growth mode. [70] The growth of Mg on Ag(100) has mainly been studied by averaging techniques such as electron diffraction [70] or Spot Profile Analysing Low Energy Electron Diffraction (SPA-LEED). [71] Figure 3.4 b presents a linescan along the blue line shown in Fig. 3.4 a. The

### 3.2. Tip-Induced Finger Formation on Ag(100)

atomic step-edges of Ag(100) appear with a height of approximately  $2.1 \text{ \AA}$  consistent with the theoretical value of  $a_0/2$  ( $a_0$  is the lattice constant of Ag). The linescan runs across two bright protrusions which are assigned to Mg clusters/islands. Their apparent heights account for approximately  $2.5 \text{ \AA}$ . Statistical analysis lead to a Mg coverage of around 5 % to 6 %. Figure 3.4 c to e are discussed further below in the context of tip-induced finger formation.

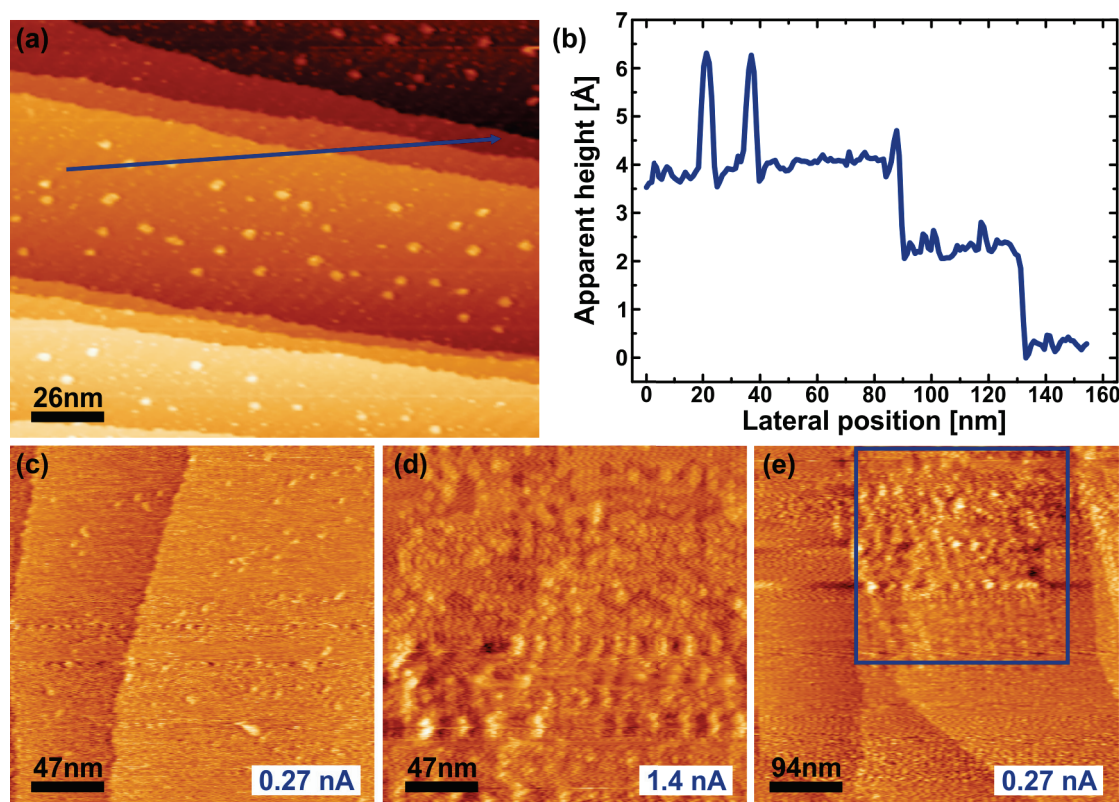


Figure 3.4: Submonolayer coverage, approximately 5 % to 6 %, of Mg on Ag(100). (a) Overview STM image with Ag(100) terraces covered with Mg atoms/clusters ( $-1 \text{ V}$ ,  $52 \text{ pA}$ ). (b) Linescan along the blue line shown in (a). Atomic step-edges of Ag(100) have an apparent height of approximately  $2.1 \text{ \AA}$ . Mg atoms and clusters appear with an height of around  $2.5 \text{ \AA}$ . (c) to (e) The same area has been scanned multiple times with a bias voltage of  $-1 \text{ V}$ . However, the setpoint tunneling current has been changed. While in (c) the target tunneling current was set to  $0.27 \text{ nA}$ , it was increased to  $1.4 \text{ nA}$  during the recording of (d). (e) Setpoint tunneling current was again reduced to  $0.27 \text{ nA}$ . Blue rectangle indicates the scanned area with higher setpoint current. No finger formation can be observed in absence of TPA molecules.

As already mentioned, both materials (Mg atoms and TPA molecules) have to be

coadsorbed on the surface in order to form metal–organic coordination networks. However, if both materials are adsorbed on Ag(100) some peculiar observations are made which will be presented in the following.

When acquiring multiple STM images of the same area, with each scan the surface seems to be consequentially changing. Figure 3.5 shows consecutively taken STM images of Ag(100) covered with nominally 20% TPA molecules and 5 % to 6 % Mg atoms. Acquiring time for one STM image accounts for 336 s. During deposition and subsequent STM measurements the sample was held at RT. Figure 3.5 a shows an STM image with a size of 470 nm × 470 nm. Elongated features along almost horizontally running step-edges can be observed. The elongated features (henceforth referred to as *fingers*) form an angle of approximately 30° with the step-edges. With increasing time of rastering the tip over the same region, the fingers become longer and thinner (see Fig. 3.5 a to e). The longest finger observed is approximately 138 nm long but it seems that in principle the length is only limited by the terrace width. Fingers are thicker at the connection point to step-edges where the thickness accounts for approximately 25 nm. As they become longer they thin out towards their end where they are only a few nm thick. Very long and thin fingers lead to fuzzy features in STM images indicating that they are less stable compared to thicker fingers. In all STM images the blue rectangle highlights an area where the growth of a finger is instructive and can be well tracked and identified. Finally, Figure 3.5 f shows a larger area with size of 940 nm × 940 nm comprising the previously scanned region (indicated by the black rectangle). It is apparent that only the previously repeatedly scanned surface area shows fingers along step-edges. The STM tip is thus needed for the creation of fingers. Areas on the surface that have not been subject to tip scanning have no or only small indentations at step-edges. In addition, considerably 'gentle' scanning parameters, that is tunneling currents as low as 10 pA and bias voltages around −0.7 V, result in tip-induced finger formation. Moreover, it could not be achieved by providing thermal energy in form of some post-annealing treatment. Post-annealing did not lead to well ordered growth of fingers along step-edges. Furthermore, it only occurs when both components, that is Mg atoms and TPA molecules, are present on the surface. On the other hand the deposition order is not a crucial factor. Figures 3.4 c to e show STM images of Ag(100) with submonolayer coverage of Mg. Two vertically running step-edges can be observed. If the setpoint tunneling current is increased from 0.27 nA to 1.4 nA the tip scanning process destroys the rastered surface area (see Fig. 3.4 d). However, no finger formation due to scanning with low or high set-point tunneling currents can be achieved in presence of only Mg atoms and absence of TPA molecules. Similarly, no finger formation can be observed if only TPA molecules are present on the surface (see previous section).



### 3.2. Tip-Induced Finger Formation on Ag(100)

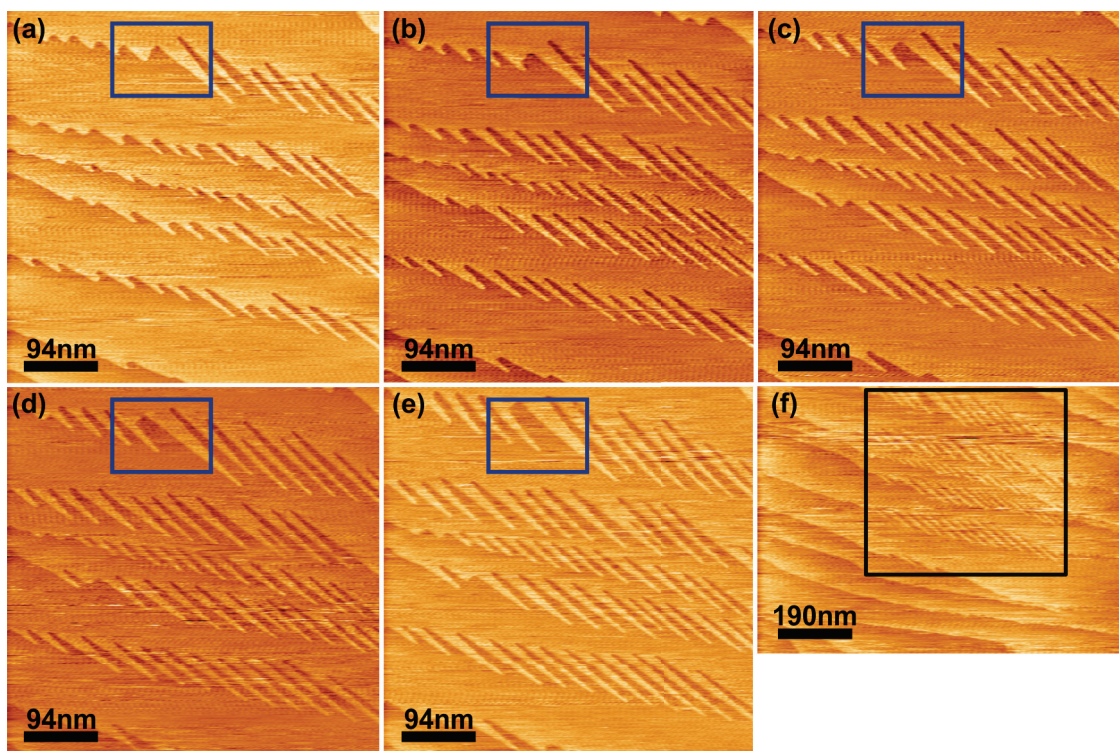


Figure 3.5: Tip-induced finger formation in presence of Mg atoms and TPA molecules on Ag(100) surface. (a) to (e) The same area was consecutively scanned and each time elongated features at step-edges increase and fingers are formed. Acquiring time for one STM image amounts to 336 s ( $-720$  mV, 10 pA). Overview STM image after having scanned multiple times the area indicated with a black rectangle. Finger formation owing to STM tip is clearly visible ( $-837$  mV, 10 pA).

To propose a tentative mechanism explaining the tip-induced finger formation it is advisable to list what has been observed in other systems and to understand the corresponding underlying mechanism. It has been shown that on clean Au(111) the STM tip can induce reorganization of the surface and finger formation. This is, however, only accomplished when using high tunneling currents ( $\sim 30$  nA) and bias voltages not smaller than 1.5 V. [72–74] Typical finger widths are 3 nm to 10 nm, with an average width of 4 nm and the length is limited by the terrace size. High tunneling currents and bias voltages trigger the removal of gold atoms at step-edges and lead to the formation of fingers along  $[110]$  directions.

Similarly, Wilson et al. [75] observed that in presence of (S)-Lysine the formation of gold nanofingers on Au(111) is facilitated. In their study considerably smaller tunneling currents ( $\leq 2$  nA) were needed for surface reorganization. Due to the interaction of

### Chapter 3. Synthesis and Characterization of Non-Covalent 2D Structures

---

lysine with Au(111), Au atoms can be displaced from step-edges and thus contribute to the growth of nanofingers. While they grow along [110] directions on clean Au(111), in presence of lysine they grow almost perpendicularly to the step-edges.

Another study showed that surface reshaping can also be induced by thermal post-annealing. [76] In this study 4-[trans-2-(pyrid-4-yl-vinyl)] benzoic acid (PVBA) was deposited at RT on Ag(110) and subsequent post-annealing lead to a dramatic restructuring of the surface. Step-edges appeared with a sawtooth pattern. The surface rearrangement was mediated by metal-ligand interactions between Ag atoms at microfacets and PVBA carboxylate moieties. Low temperature STM could resolve single molecules arranged in some self-assembly structure along reorganized sawtooth patterned step-edges probably stabilizing and driving the reorganization process.

In the present study tip-induced finger formation occurs only when both materials (Mg atoms and TPA molecules) are available on the surface. In addition, Mg cannot be replaced by Ag. As in the previous section discussed, Ag deposition followed by or prior to molecular deposition does not result in tip-induced finger formation but homoepitaxial Ag growth in presence of molecular islands. Therefore, Mg plays a crucial role for observing a reshaping of the surface. However, Figures 3.4 c to e show Ag(100) covered with Mg atoms and no reshaping can be observed without TPA molecules either. One possible explanation can thus be that TPA molecules form indeed a metal-organic coordination network which is highly mobile on the rather noble Ag(100) surface. Mg atoms are more ignoble than Ag atoms and thus give most likely electrons to the substrate upon arrival on the surface. Hence, the metal-organic coordination network is stabilized by alkaline earth-carboxylate ionic bonds. Similar networks have been observed with Na atoms on Cu(100). [69] Since the network-substrate interactions are rather weak, the electric field of the STM tip can easily interact with the dipoles of the 2D network resulting in a tip-induced reshaping of the surface. However, to illuminate the underlying mechanism in further detail, low temperature STM measurements might be able to unravel where Mg atoms and TPA molecules remain on the surface and whether a 2D network has been formed. Furthermore, XPS measurements will clarify the oxidation state of Mg atoms. In addition, it will be possible to shed light on whether carboxyl groups are deprotonated or still intact which cannot easily be resolved by STM measurements.

### 3.3 Amorphous 2D Metal-Organic Coordination Network

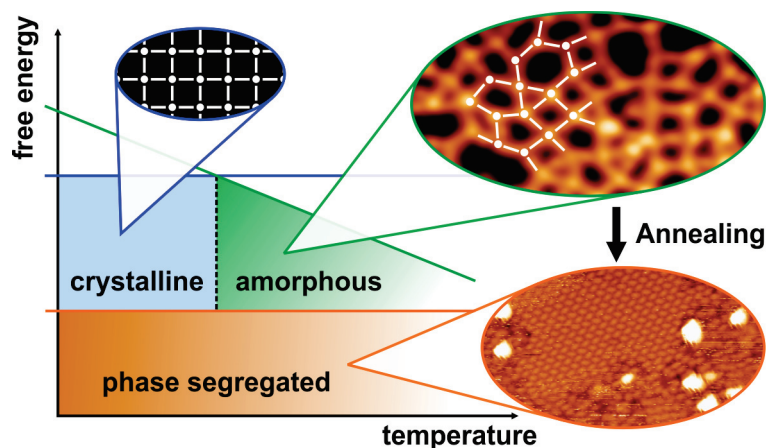


Figure 3.6: Phase diagram which shows the free energy against temperature of the system presented in this section. The amorphous metal–organic coordination network (top right) consisting of cBTBT molecules and Fe atoms is favored over the crystalline network (top left) at RT. Upon annealing the amorphous 2D MOCN phase segregates into pure domains consisting of molecular islands (cBTBT) and Fe clusters (bottom right).

In this section the on-surface synthesis and analysis of an amorphous metal–organic coordination network (MOCN) is presented. It consists of 2,7-dicyano[1]benzothieno[3,2-b]-benzothiophene (cBTBT), which is a derivative of [1]benzothieno[3,2-b]benzothiophene (BTBT), an important organic semiconductor, [77] and coadsorbed Fe atoms. It is formed at room temperature (RT) and upon annealing the amorphous metal-organic coordination network phase segregates into molecular islands and iron clusters. Figure 3.6 shows the phase diagram of the system. The free energy is plotted against temperature. At RT the amorphous 2D MOCN is favored (green, top right) over the crystalline structure (blue, top left) and upon annealing the amorphous 2D MOCN phase segregates into pure domains (orange, bottom right). In addition, statistical analysis such as the pair correlation function of the amorphous 2D MOCN are used to characterize and compare it with other amorphous 2D networks found in literature. Furthermore, the thermodynamics of the phase segregation upon annealing is investigated.

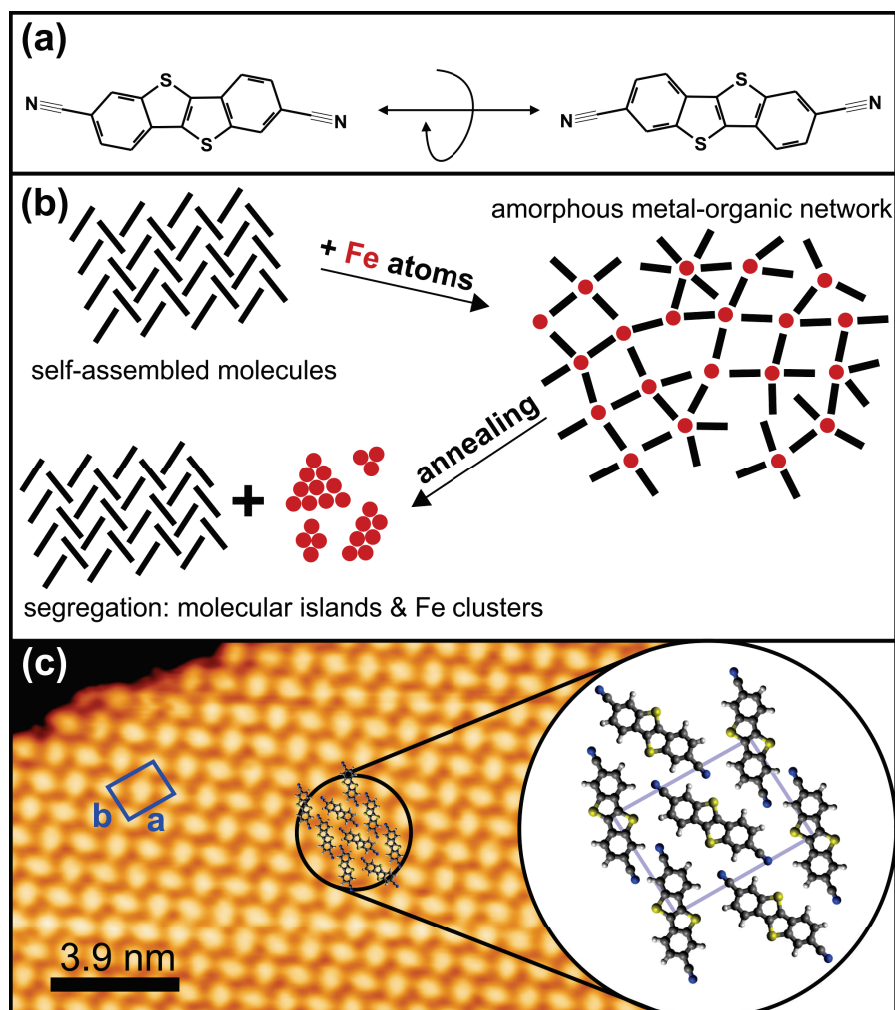


Figure 3.7: (a) Chemical structure of pro-chiral cBTBT and its two enantiomers. Rotation along the long axis transforms the enantiomers into each other as indicated by the arrow. (b) Scheme of experimental sequence: Self-assembly of cBTBT, formation of amorphous network through addition of Fe atoms, and its segregation upon thermal annealing. (c) Self-assembled structures of cBTBT on Ag(111) formed after room temperature deposition ( $U = -842$  mV,  $I = 120$  pA). Unit cell is depicted in blue. The right inset shows a zoom of the self-assembly (unit cell in light blue). Carbon atoms are shown in gray, nitrogen in blue, sulfur in yellow, and hydrogen in white.

### 3.3.1 Synthesis of an Amorphous 2D MOCN

In the following the synthesis of the amorphous 2D MOCN is described. Figure 3.7 a shows the organic semiconductor molecule used in the experiments presented in this section. It is a pro-chiral molecule. The two different enantiomers (shown on



### 3.3. Amorphous 2D Metal-Organic Coordination Network

---

the left and right side in Figure 3.7 a) can only be transformed into each other by flipping the molecule. Figure 3.7 b shows schematically the reactions which happen in the system presented in this section. First, deposition of cBTBT by molecular beam epitaxy on Ag(111) at RT leads to self-assembled crystalline islands. Subsequent introduction of Fe atoms results in the formation of an amorphous metal-organic coordination network and finally, annealing ends up in phase segregated molecular islands and Fe clusters. Figure 3.7 c shows an STM image of the self-assembly at RT. The chevron-like structure contains both enantiomers of cBTBT and the structure is stabilized by intermolecular hydrogen bonding between terminal nitrogen atoms in the cyano groups as well as the electron-rich sulfur atoms and hydrogen atoms of the aryl groups of adjacent molecules. The unit cell is shown in blue and measures  $a = 1.6\text{ nm}$ ,  $b = 1.1\text{ nm}$ , and  $\gamma = 96^\circ$ . Ball-and-stick models are depicted as an overlay on top of the STM image (a zoom is shown on the right). Carbon atoms are shown in gray, nitrogen in blue, sulfur in yellow, and hydrogen in white. The unit cell is highlighted in light blue. Similar close-packed chevron self-assembly patterns can be observed with linear terphenyl-dicarbonitrile molecules ( $\text{NC}-\text{Ph}_3-\text{CN}$ ). [78, 79]

In a second step, the introduction of iron atoms on the surface containing the self-assembled molecular layer results in the formation of disordered metal-organic networks. Figure 3.8 a shows an overview STM image with the amorphous metal-organic coordination network formed. Figure 3.8 b shows a zoom of the black rectangle depicted in Fig. 3.8 a. In previous studies of linear cyano-functionalized molecules with cobalt atoms the formation of ordered networks with hexagonal unit cells where each Co atom coordinates to three molecules that form an angle of  $120^\circ$  between each other were reported. [79, 80] Irregularities in the networks can be enforced through the deposition of more molecules than required for a saturated honeycomb mesh, resulting in 4-, 5-, and 6-fold coordination of the Co atoms and leading to pores of various shapes. [79] In the system at hand, an apparent random tessellation of the surface with differently shaped polygons is observed. Four different polygon sizes are indicated in Figure 3.8 b. Triangular, quadrangular, pentagonal, and hexagonal pores are mainly observed while heptagonal and octagonal pores were observed with low abundance.

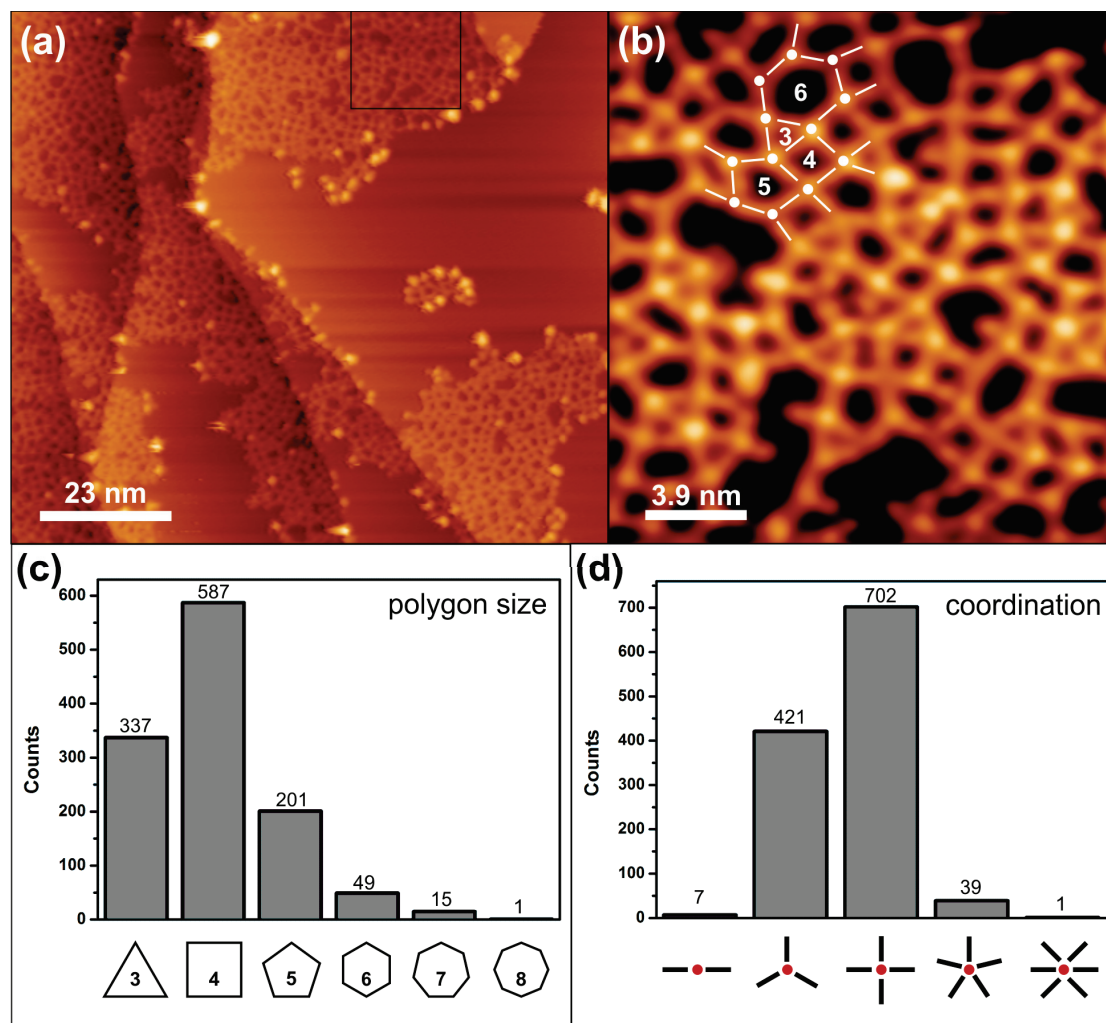


Figure 3.8: STM images of amorphous metal-organic coordination network formed by cBTBT molecules and Fe atoms and statistical analyses of the network. (a) Overview STM image ( $U = -1$  V,  $I = 0.1$  nA). (b) High-resolution STM image of the black rectangle drawn in (a). cBTBT molecules (white bars) and Fe atoms (white circles) can be observed forming polygons of different size ( $U = -1$  V,  $I = 0.1$  nA). (c) Polygon edge number distribution with a mean value of 4.01. (d) Distribution of the number of cBTBT molecules coordinating to a Fe atom. The mean coordination number is 3.66.

### 3.3.2 Characterization of Amorphous 2D MOCN

For further insight and comparability with other 2D amorphous networks, a statistical analysis of over 1000 pores within the network was performed. For discrete random variables, theory of probability provides us with the general equation for the central

moments

$$\mu_k = \sum_n (n - 4)^k p_n, \quad (3.1)$$

where  $n$  is the discrete random variable (ring size),  $p_n$  the probability distribution of the ring sizes, which is given by the histogram in Figure 3.8 c and  $k$  is the  $k$ -th moment about the mean (which is set to 4). The mean value of the number of edges can be calculated by

$$\mathbb{E}[X] = \mu = \sum_n n \cdot p_n. \quad (3.2)$$

Using the distribution shown in Figure 3.8 c leads to a mean number of edges of 4.01. The distribution of polygon occurrences is depicted in Figure 3.8 c as a histogram and it is visible that the edge number does not follow a normal (Gaussian) distribution around the mean value but rather shows a positive skewness (third central moment). The second central (variance;  $\mu_2$ ) and third central moment (skewness;  $\mu_3$ ) of the distribution give values of  $\mu_2 = 0.74$  and  $\mu_3 = 0.61$ , respectively. As compared to other 2D amorphous materials, [81] the variance as a measure of spread around the mean of a distribution falls in the middle of the two extremes of  $\text{Cu}_2\text{O}$  [82] ( $\mu_2 = 0.42$ ) and amorphous  $\text{SiO}_2$  [81] ( $\mu_2 = 1.06$ ) and is close to amorphous graphene [83] ( $\mu_2 = 0.78$ ).

The skewness as a measure of asymmetry of the distribution about its mean is large as compared to other amorphous materials, the largest value being in amorphous  $\text{SiO}_2$  ( $\mu_3 = 0.67$ ) and the smallest in  $\text{Cu}_2\text{O}$  close to zero. The origin of the large skewness in this sample is due to the small mean value of 4, which results in the triangle being the only possible smaller polygon. The distribution of polygons is skewed to the right due to the presence of pentagons, hexagons, and larger polygons, which outweigh the rather large number of triangles. The different 2D amorphous materials characterized in Ref. [81] have a mean value of 6 for the polygon edge number, with at least two possible polygons with smaller edge number (pentagons and tetragons) that can make the distribution more symmetric. The maximum in the histogram is found for the four-sided polygon, which together with the mean value of 4.01 implies a preference for rhombi or square tessellation of the surface. This remarkably singularizes this network from other glassy networks, in which 3-fold coordination is the most reported motif. Here, it is found that 4-fold tessellation is possible if the coordination number

of each Fe atom within the network is also equal to 4. Note that also metal dimers, [68] trimers, [84] and possibly larger clusters could constitute the coordination nodes, and that the coordination number could depend on cluster size. However, there is little experimental evidence to support this hypothesis, and literature reports unanimously agree that cyano ligands coordinate to only one metal center. [79,80,85,86]

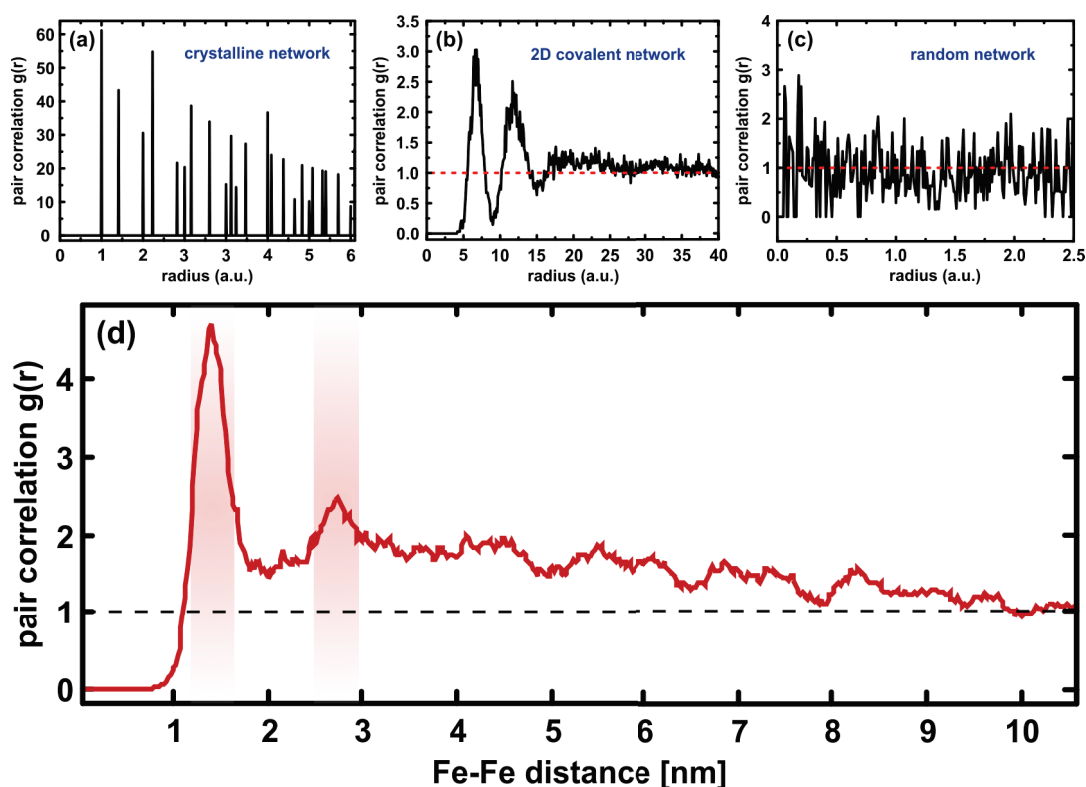


Figure 3.9: Pair correlation functions (PCFs) of four different two-dimensional (2D) networks. (a) PCF of a synthetic crystalline network with lattice constant of unity. Sharp peaks at distances corresponding to positions of atoms can be observed. (b) PCF of a 2D covalent network formed out of TBPB (see References [81, 87]). The pair correlation between connection points is calculated. (c) Purely random 2D network and its pair correlation function. The white noise around  $g(r) = 1$  is typical for uncorrelated structures. (d) Pair correlation function of the amorphous metal-organic network presented in this section. A first sharp peak lies at 1.4 nm corresponding to the length of one cBTBT molecule and constituting the nearest distance between two Fe atoms. The second peak arises at 2.8 nm, which belongs to the third-nearest distance between two Fe atoms. The second-nearest distance between two Fe atoms is not present as a clear peak due to the angular flexibility of CN-Fe bonds.

The distribution of coordination numbers is shown in Figure 3.8 d from which a

### 3.3. Amorphous 2D Metal-Organic Coordination Network

---

mean value of 3.66 can be calculated with Equation (3.2). Variance ( $\mu_2$ ) and skewness ( $\mu_3$ ) are 0.42 and  $-0.37$ , respectively. The occurrence of a smaller experimental mean value as compared to the theoretically predicted value of 4 is largely influenced by the Fe centers found at the boundary of the islands, which is commonly made up of metal centers to which only three molecules are coordinated, two making up the border and one pointing inward into the metal-organic structure. A large number of 3-fold coordinated metal centers as compared to 4-fold centers within the metal-organic network excludes the shortage of metal atoms as a possible cause of the disordered structure of the network. Additional iron clusters found on the surface alongside the amorphous network support the hypothesis that sufficient iron atoms are always available for the formation of crystalline structures. The non-crystalline nature of the network is rather a consequence of similar coordination energies for 3-fold and 4-fold coordination of the Fe atoms, which is apparent from the mere 2-fold increased occurrence of 4-fold nodes as compared to the 3-fold nodes. The relative energetic stability of the 4-fold node can be calculated assuming a Boltzmann distribution for the coordination number, yielding larger stability of the 4-fold coordination by only 13 meV. For cobalt atoms coordinated to cyano-functionalized polyphenylene molecules, the 3-fold coordination bond is stronger by 90 meV than the 4-fold coordination motif. [80] This energy difference is sufficient to significantly favor one binding motif (3-fold) over the other (4-fold), leading to ordered hexagonal networks. Another reason for the amorphous structure is the large geometric flexibility of the coordination nodes, which is manifested in angles different from  $90^\circ$  between two molecules in 4-fold coordinated centers, and angles different from  $120^\circ$  in 3-fold coordinated centers. The interplay between the two contributions, variable coordination number and structural flexibility within the node, results in the noncrystalline nature of the network.

In the following the amorphous metal-organic network is described by a pair correlation function which basically correlates pairwise every position (x-y-coordinates) of Fe atoms within the network. It is a concept derived from statistical physics and it is useful to get an idea about the (short-range) order in a gas, liquid or crystal.

**Pair correlation function** The pair correlation function  $g(\vec{r}_1, \vec{r}_2, t_1, t_2)$  gives the conditional probability density of finding a particle at position  $\vec{r}_1$  and time  $t_1$  while there is another particle at  $\vec{r}_2$  and  $t_2$  present. If the same particle is considered, the pair correlation function becomes an auto-correlation function. Here, only the stationary pair correlation function is needed and thus the time is constant. Furthermore, in homogeneous (translation invariant) systems only the relative coordinate  $\vec{r} = \vec{r}_1 - \vec{r}_2$  is relevant and due to isotropy it follows the dependence only on the absolute value

$r = |\vec{r}|$ . The pair correlation function is thus defined as

$$g(r) := \frac{V}{4\pi r^2 N^2} \left\langle \sum_{i=1}^N \sum_{j=1, j \neq i}^N \delta(\vec{r} - (\vec{R}_i - \vec{R}_j)) \right\rangle \quad (3.3)$$

where  $V$  is the volume and  $N$  the number of particles. The normalisation is such that for large  $r$ , i.e. for  $r \rightarrow \infty$ , the correlation disappears in a liquid or gas and thus  $g(r) \rightarrow 1$ . The pair correlation function  $g(r)$  describes the short-range order in amorphous materials such as fluids and glasses. For crystalline structures it shows distinct peaks. Figure 3.9 presents the PCFs for three different two-dimensional (2D) networks. As mentioned, Figure 3.9 a displays the PCF for a crystalline network exhibiting sharp peaks at atomic positions while Figure 3.9 b shows the pair correlation function of a 2D covalent network that has been formed out of TBPB monomers. [87] The PCF between all connections points is calculated and only two broad peaks corresponding to nearest and next-nearest connection points are visible. For longer distances  $r$  the pair correlation function approaches 1, which means there is no correlation anymore between connection points far away from each other. Finally, Figure 3.9 c reveals the PCF of a purely random network. As expected only uncorrelated white noise oscillating around  $g(r) = 1$  is observable.

Figure 3.9 d shows the normalized PCF of the amorphous MOCN formed out of cBTBT molecules as ligands and Fe atoms as coordination centers. Only two broad peaks can be observed: One positioned at 1.4 nm, the expected Fe–Fe distance between two coordination nodes connected by one molecule, and the other at 2.8 nm, corresponding to third-nearest neighbours  $2 \times 1.4$  nm. Due to the randomness of the network in polygon size and angle between molecules forming the same coordination node, no additional clear peaks are visible in the PCF except for the minor modulation for Fe–Fe distances larger than 4 nm. The absence of the second-nearest neighbour peak expected at  $1.4 \times \sqrt{2}$  nm in a square grid is particularly surprising and stems from the angular flexibility of CN–Fe bonds. Even minor deviations from the optimal  $90^\circ$  angle in a 4-fold coordination node alter the diagonal distance within a square to sufficiently eliminate its contribution to the PCF. This is also the reason for the absence of a correlation hole ( $g(r) < 1$ ) after the first peak situated at 1.4 nm as observed for instance for liquids and other amorphous structures such as 2D covalent networks (see Figure 3.9 b). Usually the pair correlation function  $g(r)$  can be measured by means of averaging experiments such as x-ray or neutron scattering due to its close relation to the structure factor  $S(q)$  which is measured in scattering experiments. However, real space images on different lengths scales such as optical microscopy or scanning tunneling microscopy make it also possible to obtain the pair correlation function directly as presented above.



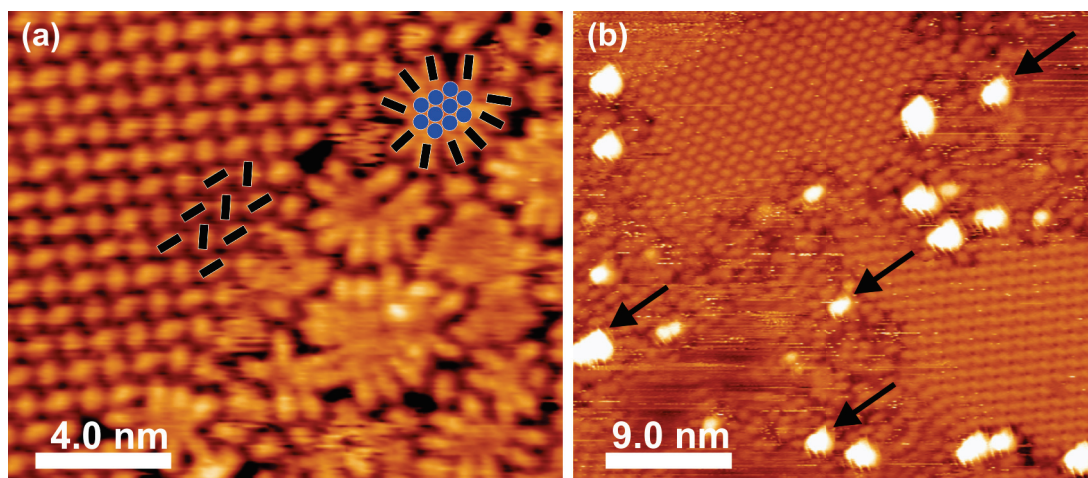


Figure 3.10: (a) Annealing at 420 K results in the segregation of the network into regions of pure metal islands (Fe atoms indicated by blue dots) surrounded by cBTBT in a radial geometry (black bars). The self-assembled structure of cBTBT can be observed in the upper left part ( $U = 0.99\text{ V}$ ,  $I = 0.1\text{ nA}$ ). (b) Self-assembled molecular domains and large Fe clusters (white protrusions pointed out by black arrows) are spatially separated after annealing at 370 K ( $U = 0.75\text{ V}$ ,  $I = 0.1\text{ nA}$ ).

The absence of long-range order as observed here is typical for glassy systems and can be interpreted as a sign of a kinetically trapped structure. This poses the question whether a thermodynamically more stable crystalline structure can be created by applying thermal energy to overcome kinetic barriers. Interestingly, annealing the sample does not lead to a more ordered crystalline metal-organic network or the reorganization in an amorphous state, but the segregation of the two components into pure domains. Annealing at temperature higher than 370 K results in the rearrangement of Fe atoms in the network into small all-metal clusters surrounded by molecules (Figure 3.10 a) and larger clusters (Figure 3.10 b, black arrows). Supramolecular networks of cBTBT self-assemble in the remaining parts of the surface. The metal clusters formed after the separation of metal and organics shown in Figure 3.10 a measure a few nanometers in diameter and are surrounded by cBTBT. The molecules bind almost perpendicular to the tangent of the metal clusters, allowing as many cyano-metal (CN–Fe) contacts as sterically possible, thus stabilizing the energetically unfavorable metal atoms at the periphery of a cluster. The second cyano group of thus coordinated cBTBT molecules is likely binding to the substrate. [88] The metal clusters in Figure 3.10 b extend spatially into the third dimension away from the surface as indicated by their large contrast in the STM image. Contrary, the smaller clusters in Figure 3.10 a radially surrounded by molecules appear flat and are probably built up from a single layer of Fe atoms. These clusters are likely intermediate structures in the

transition from amorphous metal-organic coordination network to phase-segregated islands that are stabilized and separated from the surround by cBTBT molecules. The small number of metal atoms renders 2D cluster growth energetically favorable. Island growth into the third dimension only dominates upon adding additional Fe atoms.

Metal-organic networks with 'metal-cyano' coordination motifs are usually imaged at low temperature due to their limited thermal stability [79, 80, 89] with some notable exceptions. [90, 91] More stable networks are based on metal-carboxylate coordination bonds and can readily be studied at room temperature (RT) [68, 92, 93] and even higher temperatures. [69] In addition, the dissolution of Co clusters upon reacting with carboxylated molecules can be followed in real time at RT. [94] Thermal annealing steps can be required to force the networks into their thermodynamic most stable state. [95] It is thus clear that an intricate interplay between molecular functionalization and metal center within the network governs thermal stability and the formation of a given crystal structure. Although the phase segregation is not addressed in the literature of surface-supported metal-organic coordination networks, the organic phase is commonly deposited before metal sublimation to ensure the growth of networks. The deposition of the metal prior to the molecules in a first instance leads to metal clusters, which often cannot be broken up through thermal annealing, and thus no metal-organic phase can be formed. In the following, this observation on the basis of thermodynamic arguments is rationalized.

### 3.3.3 Thermodynamics of Phase Segregation

To understand the disordered morphology and the segregation of the metal-organic phase, entropic and enthalpic contributions in both amorphous and phase-segregated structures can be estimated. The segregated structure appears to be thermodynamically favored over the amorphous state as it prevails at room temperature after thermal annealing. Additionally, the entropy gain, which compensates the enthalpic fee, due to disorder in the amorphous compared to the crystalline network is calculated. Entropy enters the thermodynamic description as configurational entropy  $S_{\text{conf}}$  of the amorphous structure as well as vibrational entropy  $S_{\text{vib}}$  of the amorphous, crystalline and phase segregated structure. Translational and rotational entropies are zero for immobile species on the surface and are thus neglected in the following discussion.

First, the configurational entropy is discussed, which reflects the number of ways molecules and metal atoms can arrange on the surface. For a given and fixed probability distribution  $p_n$  (for example  $p_n$  from Figure 3.8 d), where  $n$  is the number of coordinated molecules, any possible geometric realization (the distribution  $p_n$  is not affected) of 2-, 3-, or 4-fold and higher coordination sites on the surface has the same



### 3.3. Amorphous 2D Metal-Organic Coordination Network

internal energy and entropy. The configuration entropy  $S_{\text{conf}}$  can be written as

$$S_{\text{conf}} = -k_B \sum p_n \log(p_n) \quad (3.4)$$

where  $k_B$  is Boltzmann's constant and  $\log(x)$  the natural logarithm. The internal energy  $U = -\sum p_n \varepsilon_n$  of the network can be used to express the Helmholtz free energy  $A = -TS_{\text{conf}} + U$  of the network as

$$A = -TS_{\text{conf}} + U = k_B T \sum p_n \log(p_n) - \sum p_n \varepsilon_n \quad (3.5)$$

where  $\varepsilon_n$  is the energy of one coordination node with  $n$  ligands and  $T$  the temperature. The first term in the equation corresponds to the entropic contribution to the Helmholtz free energy, and the second represents the average internal energy per coordination node, which becomes only  $\varepsilon_4$  for the crystalline network (besides vanishing configurational entropy). Using Boltzmann weights the relative energies with the arbitrarily chosen and fixed reference energy  $\varepsilon_4$  can be calculated

$$\varepsilon_n = \varepsilon_4 - k_B T \log \frac{p_4}{p_n}. \quad (3.6)$$

The internal energy per coordination node thus becomes (with probability distribution  $p_n$  from Fig. 3.8 d)

$$U = -(\varepsilon_4 - 0.0081 \text{ eV}). \quad (3.7)$$

The amorphous state is hence always accompanied by a non-favorable internal energy as compared to the crystalline state with 4-fold coordination nodes. Using Equation (3.4) the configurational entropy  $S_{\text{conf}}$  of the amorphous network equals (with probability distribution  $p_n$  from Fig. 3.8 d)  $0.071 \text{ meVK}^{-1}$  and for temperatures greater than 115 K compensates the reduced internal energy rendering the amorphous network more stable. Derived from  $0.071 \text{ meVK}^{-1} \cdot T = 0.0081 \text{ eV}$ , which results in  $T = 114.08 \text{ K}$ . At room temperature,  $TS_{\text{conf}} = 0.021 \text{ eV}$ , which is roughly 2.5 times larger than the internal energy penalty caused by disorder. The amorphous network is stabilized by a small but relevant entropic contribution. An additional entropic stabilization from the angular flexibility within the coordination nodes further favors the disorder over crystallinity, which was not taken into account here. [96]

As mentioned, vibrational entropy  $S_{\text{vib}}$  has not been considered so far. It can have contributions from (i) intermolecular vibrations,  $S_{\text{vib,intermol}}$ , in the self-assembled molecular islands (after phase segregation) and from metal-organic coordination nodes,  $S_{\text{vib,coord}}$ , in case of (amorphous and crystalline) metal-organic network. (ii) Vibrations normal to the surface and finally (iii) intramolecular vibrations. The last

two vibrational contributions, vibrations normal to the surface and intramolecular vibrations, are unaltered in crystalline and amorphous networks and after phase segregation as the number of molecules stays constant. Only contributions from  $S_{\text{vib,intermol}}$  and  $S_{\text{vib,coord}}$  are relevant as they interchange upon phase segregation. The mean coordination numbers are almost the same in the crystalline and amorphous network (3.66 and 4, respectively) and therefore both vibrational entropy terms cancel each other and only configurational entropy is relevant as mentioned above. Contrarily, the amorphous network constitutes vibrational modes in metal-organic coordination nodes  $S_{\text{vib,coord}}$  while after phase segregation these vibrations are replaced by intermolecular vibrations  $S_{\text{vib,intermol}}$  in the self-assembled islands of cBTBT. Intermolecular vibration modes have a higher energy contribution to entropy ( $TS_{\text{vib,intermol}} \approx 0.045$  eV), which favors phase-segregation upon thermal annealing (see below). Vibrations in metal-organic coordination nodes constitute approximately one order of magnitude less entropic energy ( $TS_{\text{vib,intermol}} \approx 0.001$  eV).

For the segregation to be feasible, the Helmholtz free energy of the phase-segregated state  $A_{\text{phase-segregated}}$  needs to be lower than that in the disordered state  $A_{\text{amorph}}$ . In the crystalline and phase separated state with hypothetically defect-free structures, the configurational entropy is zero and  $A_{\text{cryst}} = U_{\text{molecules}} + U_{\text{metal}}$ , where  $U$  is the internal energy in the molecular layer and the metal clusters. Typical coordination bond energies of  $\epsilon_{\text{coord}}$  range from 0.3 eV to 0.6 eV, [97–99] while energies for hydrogen bonds range from 0.05 eV to 0.7 eV in self-assembled molecular monolayers, and from 1 eV to 5 eV for metal-metal bonds. [98, 100] Iron within a metal cluster has a binding energy of about 4.4 eV, which clearly suggests that the segregation is strongly enthalpic in origin, driven by the very large binding energy within a metal cluster. Removing one iron center from a coordination node (energy penalty < 1 eV) and adding it to a metal cluster (energy gain  $\approx 4$  eV) significantly lowers the free energy, while additional stability is expected from the newly formed hydrogen bonds within the molecular layer. This remains valid when the entropic penalty of segregating the amorphous metal-organic network is accounted for, which in the present system is the sum of configurational and metal-organic coordination node vibrational entropy  $TS_{\text{conf}} + TS_{\text{vib, coord}}$ . Both terms are negligible as compared to enthalpic contributions. On the other hand, soft intermolecular vibrational modes expected in the self-assembled molecular structure can be well below 10 meV (order of 1 meV in molecular crystals, [101] with  $TS_{\text{vib,intermol}}$  well above 0.05 eV), and can thus substantially contribute to the entropic stabilization of the segregated structure. The annealing is necessary to overcome the kinetic barrier that hinders segregation, and the amorphous network is kinetically trapped at room temperature. Kinetic trapping has recently been reported for different disordered [96] and ordered [102] surface-supported molecular structures and can stabilize intermediate phases in a crystalline-to-amorphous-to-crystalline transition in coordination

polymers. [103]

A possible explanation for the amorphous structure can be found in the synthesis procedure of the network. During sublimation of iron onto the surface covered with the molecular layer, single Fe atoms arrive at the surface with a spatially homogeneous profile at the local level. After adsorption, the metal atoms diffuse on the surface, interrupting and dissociating the self-assembled organic network and subsequently coordinating to the cyano groups. Thermal energy seems to be insufficient for the formation of a crystalline network with either three or four coordination bonds per metal atom, resembling a diffusion-limited process in which the diffusion of the metal atoms is hindered by the formation of coordination bonds (besides their interaction with the substrate metal atoms). For the same reason, no phase separation into purely organic and metallic islands occurs at RT. As discussed above, similar binding energy of 3- and 4-fold coordination nodes along with the angular flexibility of the molecules within one node leads to the non-zero configurational entropy and is partly responsible for the non-crystalline nature of the network. The entropy compensates for the energy penalty that arises from the different coordination environment and stabilizes the glassy network. The amorphous structure of the network may also be due to the nature of the molecules, which are non-linear and pro-chiral, thereby tentatively inhibiting the formation of symmetric rhomboidal or hexagonal pores. In addition, the sulfur atoms in the molecule can interact strongly with the surface, possibly favoring three equivalent adsorption sites on the 3-fold symmetric Ag(111) surface rotated by 120°, which consequently can partially override the favored 4-fold symmetry of the coordination node. All of these factors will contribute to the frustrated growth of well-ordered metal-organic coordination networks.

Nevertheless, the limited thermal stability of the amorphous 2D MOCN is shown. The limited thermal stability of (amorphous) 2D MOCNs is a general drawback of non-covalently bonded 2D materials and motivates the study of 2D nanostructures and materials consisting of only covalent bonds since their stability is increased. The next chapter deals with on-surface synthesis of covalent 2D materials.



## 4 Synthesis and Characterization of 2D Covalent Nanostructures\*

In the previous chapter non-covalently stabilized two-dimensional (2D) materials on metal surfaces were investigated and presented. The structures consisted mainly of metal-organic coordination networks which formed out of metal atoms acting as coordination centers while organic molecules acted as ligands. The networks are thus stabilized by non-covalent interactions namely metal-ligand interactions. In addition, van der Waals and dipole interactions, hydrogen-bonding and  $\pi - \pi$  stacking can all lead to 2D structures that are stabilized via non-covalent bonds. A great disadvantage of 2D materials built by these non-covalent interactions is their limited stability. As it was shown in the previous chapter, for instance, metal-organic coordination networks can disintegrate at elevated temperatures and thus are not very temperature robust. The situation changes for 2D materials which are formed by covalent bonds. Due to the nature of covalent bonds, 2D structures built up only by inherent covalent bonds are much more robust against external influences such as temperature and are therefore promising materials for potential implementations and applications. In 2007 Grill et al. formed covalent nanostructures on a metal surface via on-surface Ullmann coupling [106] for the first time. Since then many different on-surface synthesis reactions mainly inspired by solution chemistry have been investigated. Dehydration and esterification of boronic esters [107], imine formation [108, 109], acylation [110, 111], dimerization of N-heterocyclic carbenes [112] or dehydrogenative coupling of alkanes [113] are only a small excerpt of the myriad on-surface synthesis protocols that have since been reported in literature. A comprehensive overview of on-surface reactions in UHV can be found in Ref. [24]

In this chapter the on-surface Ullmann reaction, [114–116] on-surface Glaser coupling [117–119] and on-surface decarboxylation [120] reaction for 2D nanostructure synthesis in the bottom-up fashion will be presented. In addition, the experimental as

---

\*Parts of this chapter are based on publication #2 [104] and #4 [105] of the CV publication list.

well as theoretical investigation of the electronic properties of 2D nanostructures are presented at the end of this chapter.

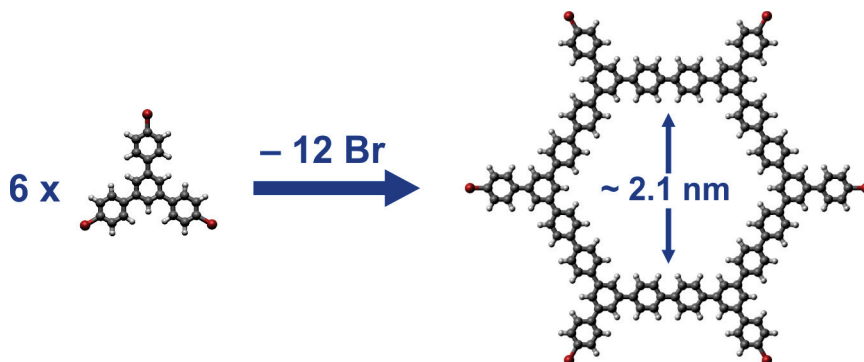


Figure 4.1: Sketch of on-surface Ullmann reaction to grow two-dimensional nanostructures. Ball-and-stick models of 1,3,5-tris(4-bromophenyl)benzene (TBPB) and a hexagon that forms out of six TBPB precursor molecules.

### 4.1 2D Nanostructures via On-Surface Ullmann Coupling

In this section the on-surface Ullmann reaction is presented. The dehalogenation reaction catalyzed by copper (Cu) atoms was originally studied by Ullmann in solution. [121] In the course of on-surface synthesis of covalent nanostructures and polymers, metal surfaces act as catalyst to drive the dehalogenation of organic precursor molecules. [122, 123] Approximately 90 years later the study of this reaction on surfaces under ultra-high vacuum conditions has been launched. To begin with it has been studied with averaging techniques such as Auger electron spectroscopy. [124, 125] The first observation of the on-surface Ullmann reaction on the atomic level by STM was in 2000. Iodine was separated from iodobenzene using tunneling electrons. Bringing two resultant phenyls close to each other by lateral manipulation results in biphenyl molecules. [114] The first 2D polymer created out of brominated precursor molecules was reported by Grill et al. in 2007. [106] Besides a lot of one-dimensional structures grown with the on-surface Ullmann coupling, [126] graphene nanoribbons are also grown with suitable brominated precursor molecules and take advantage of the selective splitting of C–Br bonds. [127] Since the growth via Ullmann coupling needs metals as catalyst, as-grown 2D nanostructures and polymers reside usually directly on top of the metal substrates and the intrinsic electronic properties of the reaction products are strongly influenced by the metal. Therefore it is difficult to access the intrinsic electronic properties of 2D polymers experimentally if they remain on metal substrates. Attempts have been made to decouple 2D polymers from the metal substrates for instance by means of iodine intercalation. [31] An alternative might be the

growth directly on top of bulk insulating substrates such as calcite. [128,129] At the end of this section the study of the dehalogenation and covalent coupling of aryl halides on Ni(111) supported boron nitride and graphene is presented. This represents an intermediate step between totally metallic and insulating substrates and the influence of metallic substrates can be gradually investigated.

### 4.1.1 2D Polymer Formation on Au(111)

In this section the formation of extended-porous graphene which is a polyphenylene with a pore size of approximately 2.1 nm on Au(111) is presented as an example of 2D polymer formation on a metallic substrate. [130] The polymer forms out of 1,3,5-tris(4-bromophenyl)benzene (TBPB). This organic molecule has already been studied on various metallic substrates such as Cu(111), [130] Ag(110), [130] Ag(111) [131] or Au(111). [132] The polymers have all in common that they lack long-range order and exhibit a lot of defects (non-hexagonal structures). [81] Figure 4.1 shows a schematic of the on-surface Ullmann reaction. Six TBPB molecules form one hexagonal ring by the abstraction of 12 bromine (Br) atoms. The size of the pore is indicated. Obviously the size of the pore can be tuned by the choice of precursor molecule.

Figure 4.2 a shows an overview STM image of 1,3,5-tris(4-bromophenyl)benzene (TBPB) deposited on Au(111) at room temperature and subsequent annealing at 250 °C (523 K). TBPB reacted with each other via debromination and subsequent covalent coupling. The reaction products cover both terraces. Figure 4.2 b shows a smaller area where hexagonal structures can clearly be observed. However, defects such as pentagonal structures are also present within the 2D network. The white circle highlights an area without covalent polymers and lines with 5 Å spacing are faintly visible. They can be attributed to split-off Br atoms consistent with literature. [133] Figure 4.2 c shows a high-resolution STM image of the area highlighted by the black rectangle in Fig. 4.2 b with an accordingly scaled ball-and-stick model superimposed. The pore-to-pore distance of approximately 2.1 nm (blue line and arrows in Fig. 4.2 c) matches well with extended-porous graphene. [130, 134] Figure 4.2 d presents the data of the linescan along the blue line in Fig. 4.2 c. The molecular polymer appears with an apparent height of approximately 1 Å and the size of the pore accounts for 2.1 nm in agreement with gas-phase DFT calculations and experimentally obtained values in literature.



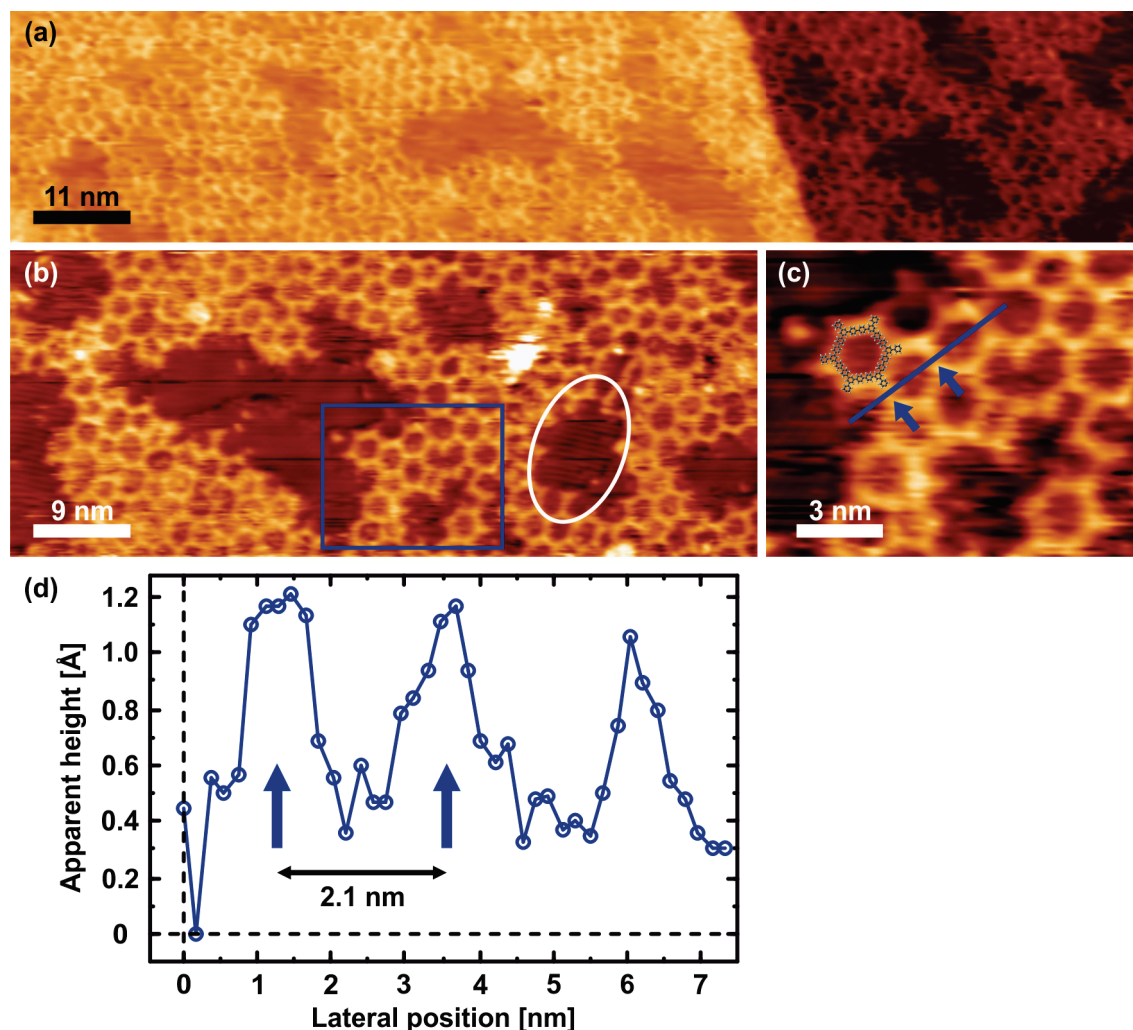


Figure 4.2: On-surface Ullmann coupling reaction of 1,3,5-tris(4-bromophenyl)benzene (TBPB) on Au(111). (a) Overview STM image of reaction products after post-annealing at 250 °C (523 K). Hexagonal structures can be observed on both terraces as well as along the step-edge ( $U = -2.3\text{ V}$ ,  $I = 20\text{ pA}$ ). (b) STM image of a smaller area with higher resolution. Hexagonal pores reminiscent of extended-porous graphene can be observed. However, defects in form of pentagonal structures are also present. White circle indicates a surface area that is not covered with polymers but close inspection reveals lines with 5 Å spacing which can be attributed to split-off bromine (Br) atoms ( $U = -1.8\text{ V}$ ,  $I = 34\text{ pA}$ ). (c) High-resolution STM image of the area indicated by blue rectangle in (b). Scaled ball-and-stick model of extended porous graphene fits well with the size of the experimentally observed features ( $U = -1.8\text{ V}$ ,  $I = 34\text{ pA}$ ). (d) Linescan along the blue line shown in (c). Polymer has an apparent height of 1 Å and the pore size accounts for 2.1 nm in agreement with theory and literature.



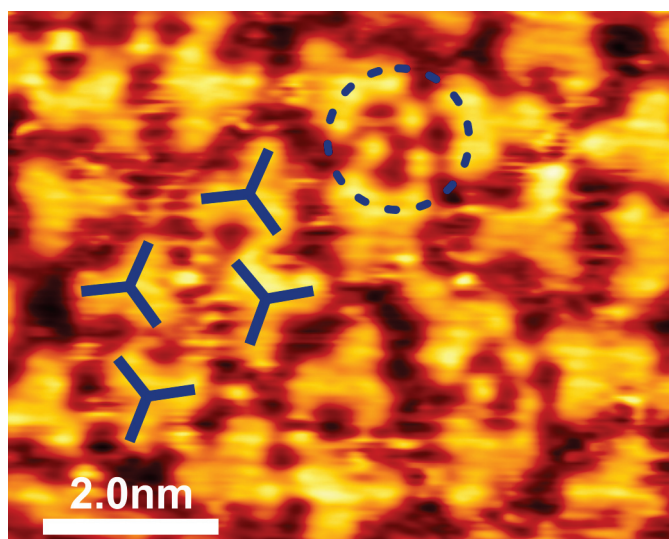


Figure 4.3: High-resolution STM image of TBPB on Ni(111) at RT. The molecules (indicated in blue) order locally with an absence of long-range order. At RT TBPB molecules stay intact despite partial debromination. Split off Br atoms (blue circle) reside on the surface ( $U = -1.4\text{V}$ ,  $I = 52\text{pA}$ ).

#### 4.1.2 Halogenated Molecules (TBPB) on Ni(111)

The previous section showed the Ullmann coupling reaction on Au(111). This coupling reaction has also been intensively studied on other metal surfaces such as Ag(111) [30] and Cu(111) [130, 131] and with various precursor molecules to form covalently bonded polymers. [127, 135, 136] However, as it is shown in this section, on more reactive metal surfaces such as Ni(111) no covalent coupling can be achieved. The precursor molecules merely degrade and decompose when thermal energy via annealing is applied. Figure 4.4 shows STM images after annealing the Ni(111) surface at different temperatures. The surface is covered with approximately one monolayer of TBPB molecules and upon annealing no oligomers or polymers are observed. The molecules start degrading and decomposing at  $150\text{ }^{\circ}\text{C}$  (423 K) and higher temperatures. Figure 4.3 shows a high-resolution STM image of TBPB deposited at RT on Ni(111) at high coverage (approximately one monolayer). Single molecules are indicated in blue and arrange in two different binding geometries with respect to the surface without long-range order (see also Fig. 4.4) suggesting that the molecule–substrate interaction is dominating. Circular bright protrusions (blue circle) are observed in the STM image and are tentatively attributed to bromine atoms that have split off the precursor molecules. Apart from dehalogenation, the TBPB seems to stay intact on Ni(111) at RT and no C–C bond breaking is observed. The absence of long-range order

can be explained by the strong interaction between reactive Ni and surface-stabilized radicals.

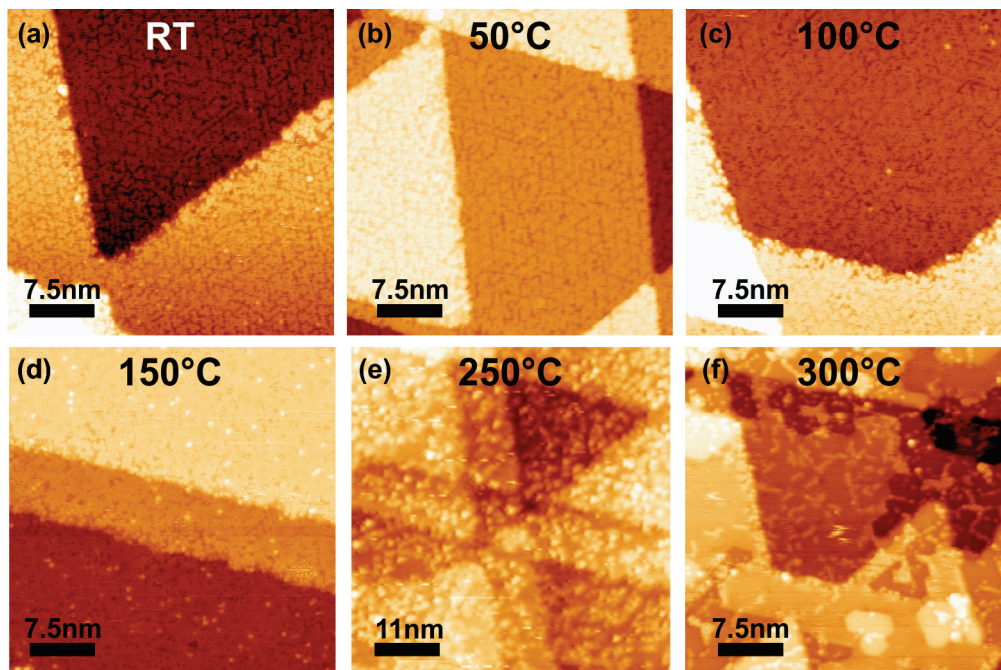


Figure 4.4: Successive annealing of TBPB on bare Ni(111). Annealing temperatures are indicated. TBPB monomers start degrading and decomposing at approximately 150 °C (423 K). No oligomers or polymers are observed. (a) to (e) originate from the same sample and (f) was measured on a different sample with initially less TBPB molecules deposited. (a)  $U = -1.5\text{V}$ ,  $I = 52\text{pA}$ ; (b)  $U = -1.4\text{V}$ ,  $I = 54\text{pA}$ ; (c)  $U = -0.4\text{V}$ ,  $I = 280\text{pA}$ ; (d)  $U = -1.3\text{V}$ ,  $I = 550\text{pA}$ ; (e)  $U = -1\text{V}$ ,  $I = 68\text{pA}$ ; (f)  $U = -1.5\text{V}$ ,  $I = 86\text{pA}$ .

### 4.1.3 Covalent Coupling on Ni(111) Supported Hexagonal Boron Nitride and Graphene

The previous sections showed that the brominated precursor molecule TBPB reacts to 2D polymers on Au(111) while on the more reactive Ni(111) surface the molecule merely decomposes upon annealing. In this section the on-surface coupling reaction of aryl halides on hexagonal boron nitride (h-BN) and graphene both grown as a single layer on Ni(111) is presented. In general the polymers are strongly coupled to the metal substrates which also act as template. However, this makes it difficult to study the intrinsic (electronic) properties of the as-grown nanostructures. One approach is to switch to insulating surfaces such as calcite [128,129] which makes, however, scanning tunneling microscopy not usable anymore. Recently it has been shown that post-synthetic decoupling can be achieved by intercalation of iodine (I) atoms. [31] Another

#### 4.1. 2D Nanostructures via On-Surface Ullmann Coupling

approach is the use of decoupling layers on metal surfaces on which nanostructures are directly grown. [137] In this section this second approach is presented. Both graphene and h-BN function as model decoupling layers from the highly reactive Ni surface. Due to the non-negligible interaction with the Ni surface the reactivity is shown to remain sufficiently large for debromination of the precursor molecule. However, apart from the debromination the molecules stay intact. Interestingly, the scission of C–Br bond exhibits strong similarities despite the different electronic structure of conductive graphene and insulating h-BN.

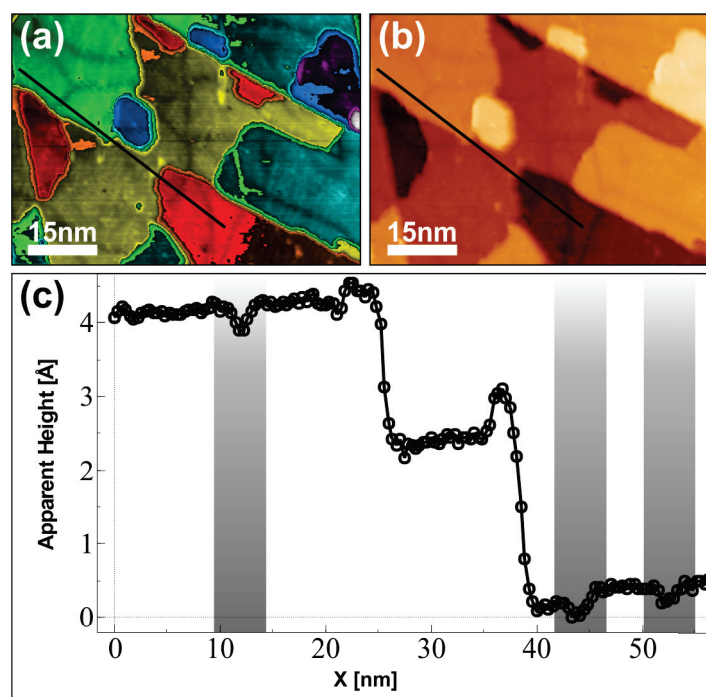


Figure 4.5: Monolayer of h-BN grown on Ni(111). (a) and (b) show the same STM data displayed with different color coding. Typical grain boundaries of the h-BN layer are visible as darker, branched features on the terraces ( $U = -0.8\text{ V}$ ,  $I = 0.22\text{ nA}$ ). (c) Linescan profile along the black line shown in (a) and (b). Monoatomic steps with an apparent height of approximately  $2\text{ Å}$  are observed. The grain boundaries appear with an height of less than  $1\text{ Å}$  (grey shades).

##### TBPB on h-BN/Ni(111)

A monolayer of h-BN can be grown in-situ by exposing the clean and hot Ni(111) surface held at  $750\text{ °C}$  ( $1023\text{ K}$ ) to  $360\text{ L}$  of borazine ( $\text{B}_3\text{H}_6\text{N}_3$ ). [138] The reaction rate drops by multiple orders of magnitude after completion of the first layer and therefore offering more borazine molecules than needed still results in the growth of a

monolayer (*self-limited growth*). Figure 4.5 a and b show a typical STM image with different color coding after the growth of h-BN on Ni(111). On free terraces darker, branched features can be nicely observed. Figure 4.5 c shows the linescan profile along the black line in Fig. 4.5 a and b. Besides monoatomic steps with an apparent height of approximately 2 Å, small indentations with an apparent height of less than 1 Å are observed (grey shades). The latter correspond to the darker, branched features observed in the STM images. They are assigned to grain boundaries and represent meeting points of h-BN islands which started growing at different nucleation sites on the surface. The grain boundaries can be used to check for successful h-BN growth on Ni(111).

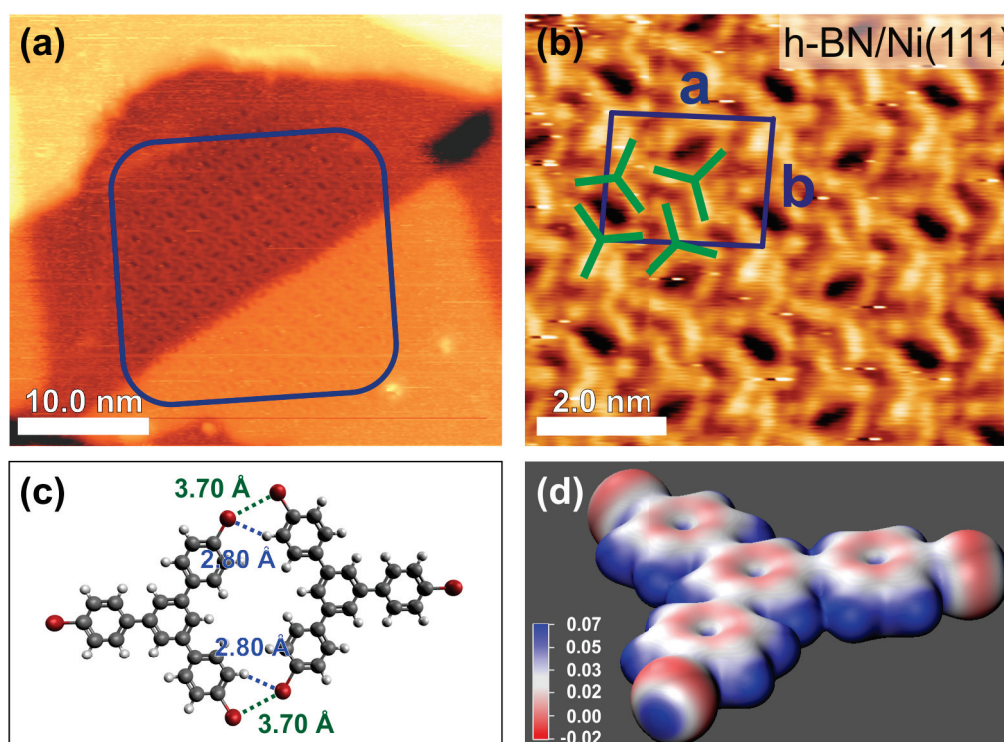


Figure 4.6: 1,3,5-tris(4-bromophenyl)benzene (TBPB) adsorbed on h-BN/Ni(111) at 140 °C. (a) Overview STM image: Bare h-BN/Ni(111) as well as a self-assembled island of TBPB (blue rectangle) are visible. (b) High-resolution STM image of the self-assembly island in (a). Precursor molecules are represented by green tripods. The unit cell is shown in blue ( $a = 2.5$  nm,  $b = 2.0$  nm,  $\theta = 92^\circ$ ). Dimers of alternating chirality run along vertical lines. (c) Ball-and-stick model of a dimer formed by two TBPB molecules. The gas phase DFT optimized distances are 2.8 Å, 3.7 Å for H...Br, Br...Br respectively. (d) Electrostatic potential map of intact TBPB. Electropositive holes at the periphery of Br atoms as well as electronegative belt around it are visible. Units of colorscale in Rydberg  $e^{-1}$



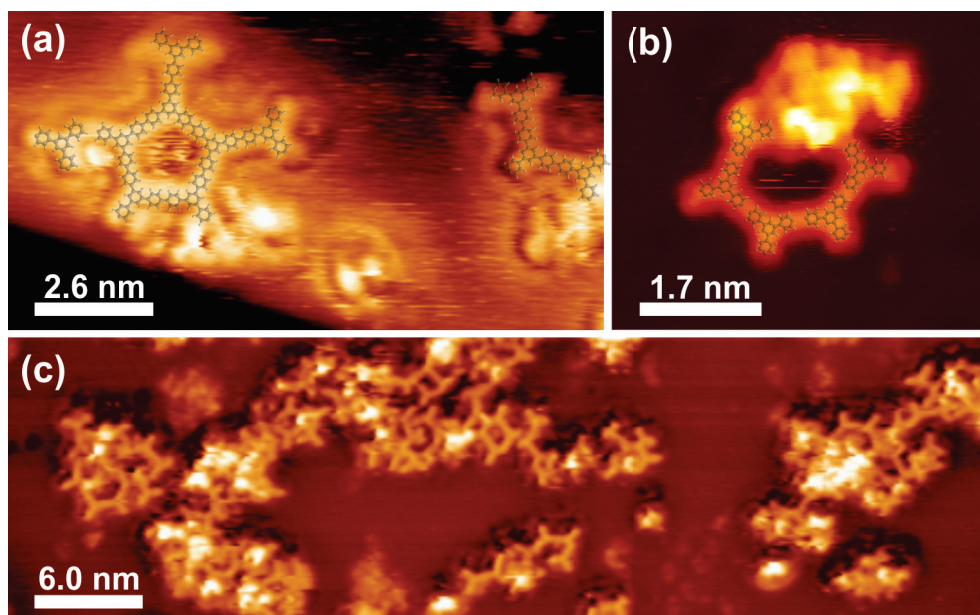


Figure 4.7: Reaction products of TBPB on h-BN/Ni(111) after annealing between 250 °C and 300 °C (523 K and 573 K). (a) High-resolution STM image of a pentagon-shaped oligomer (left) and a trimer (right). A single molecule pinned to the surface is also visible (left). Scaled ball-and-stick models are superimposed and corroborate the covalent coupling ( $U = -1$  V,  $I = 46$  pA). (b) High-resolution STM image of a quasi-hexagon with a bright protrusion in the upper right part ( $U = -1.5$  V,  $I = 330$  pA). (c) Overview STM image of reaction products. Oligomers of different size and shape are visible. Bright protrusions appear with an height of approximately 3 Å, while oligomers and molecules have an apparent height of only 1 Å ( $U = -1.4$  V,  $I = 52$  pA).

After the growth of a monolayer h-BN on Ni(111) the precursor molecules for on-surface 2D polymer synthesis are introduced on the surface. Figure 4.6 a shows a self-assembled island of intact 1,3,5-tris(4-bromophenyl)benzene (TBPB) that forms after deposition onto a hot surface held at 140 °C (413 K) at sub-monolayer coverage (blue rectangle). The domain of about 340 nm<sup>2</sup> is surrounded by the bare h-BN/Ni(111) surface, where no self-assembly is observed (outside the blue rectangle in Fig. 4.6 a). Figure 4.6 b shows a close up STM image of an area within the island. Each triangular protrusion is assigned to a TBPB molecule. The oblique unit cell shown in blue ( $a = 2.5$  nm,  $b = 2.0$  nm,  $\theta = 92^\circ$ ) contains four molecules (green tripods) and the packing arrangement is similar to self-assembled structures of TBPB reported on Au(111). [132] For additional insight into the intermolecular interactions, a dimer of two planar TBPB molecules is calculated (Fig. 4.6 c, Gaussian 09, DFT, M06-2X functional, 6-31G(d,p) basis set), resembling two of the four molecules found in the unit cell. Note that these dimers are pro-chiral in the sense that once confined to two

dimensions they are non-superimposable mirror-images of each other. To transform a dimer of one chirality into the other dimer, either the halogen bonds between two molecules have to be split or the dimer has to flip. Both are accompanied by an energy penalty. Four close contacts can be found, two Br...Br (3.70 Å) and two Br...H bonds (2.80 Å). The electrostatic potential map of the precursor molecule (shown in Fig. 4.6 d) reveals the typical  $\sigma$ -hole at the Br atom (blue), resulting in attractive interactions between this electropositive hole (blue) and the electronegative circumference (red) between two Br atoms of adjacent molecules, and the electronegative belt (red) and H atoms. [139, 140]

In order to induce debromination and covalent coupling samples covered with sub monolayer coverage of TBPB were annealed between 250 °C and 300 °C (523 K and 573 K, respectively) for 15 min. At these elevated temperatures C–Br bonds are cleaved and oligomers are observed on the surface. Figure 4.7 a shows an STM image of two oligomers: a heptamer and a trimer; a single TBPB molecule is visible at the left end of the heptamer that is not connected to other molecules. Intermolecular distances of 1.3 nm within the oligomers which is in accordance with previous studies [87, 130] and scaled molecular ball-and-stick models confirm the formation of covalent bonds. Figure 4.7 b shows an STM image of a quasi-hexagon with a bright protrusion at the upper part. Finally, an overview STM image is given in Figure 4.7 c, where oligomers of different sizes can be observed. Dimers, trimers, and larger oligomers are clearly visible. Long-range order and extended oligomers/polymers are not observed, and many terminal sites of the oligomers are apparent. These terminal sites are presumably dehalogenated, based on geometric considerations of the size of the monomeric units in the oligomers, and bind to the underlying h-BN layer. Bright features in the STM topograph are found close to the oligomers. As these features appear to be higher than the oligomers (approximately 3 Å compared to 1 Å) they are tentatively assigned to upright standing molecular fragments. The origin of the upright adsorption geometry will be discussed below. Large polymers are not observed for different annealing temperatures and times as well as coverages.

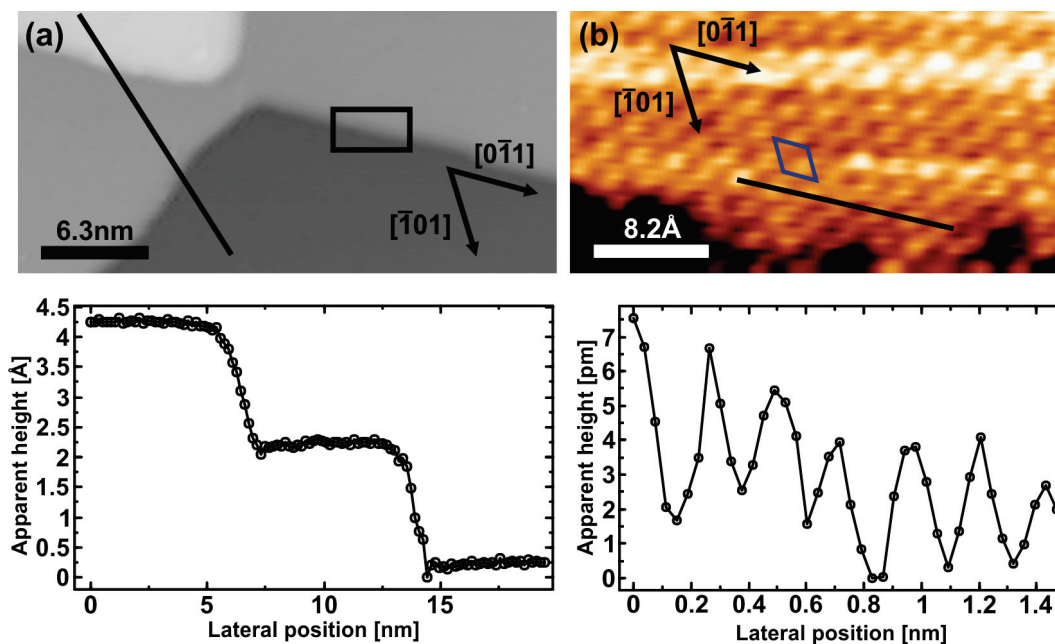


Figure 4.8: Monolayer of graphene grown on Ni(111). (a) Typical overview STM image of graphene/Ni(111). The high symmetry directions are indicated ( $U = -0.1$  V,  $I = 53$  pA). Bottom: Linescan along black line in (a). Monoatomic step-edges with an apparent height of approximately  $2 \text{ \AA}$  are observed. (b) High-resolution STM image with atomic resolution ( $U = -0.1$  V,  $I = 0.1$  nA). The unit cell of graphene is shown in blue. Only C atoms residing on top sites are visible. Bottom: Linescan along black line in (b). Periodic corrugation with an apparent height of approximately  $4 \text{ pm}$  is visible. The protrusions are periodically separated by around  $2.5 \text{ \AA}$  which is in agreement with the lattice constant of graphene and Ni.

### TBPB on Graphene/Ni(111)

Graphene was used as an alternative decoupling layer to examine whether extended polymers can be synthesized. Similarly to the h-BN growth on Ni(111), a monolayer of graphene can be grown in-situ by exposing the clean and hot Ni(111) surface held at  $580^\circ\text{C}$  ( $853 \text{ K}$ ) to  $225 \text{ L}$  of ethylene ( $\text{C}_2\text{H}_4$ ). [141, 142] Also for graphene growth the reaction rate drops by multiple orders of magnitude after completion of the first layer and therefore offering more ethylene molecules than needed for a monolayer does still result in the growth of one layer. Figure 4.8 a shows a typical overview STM image at RT after growth of a monolayer of graphene on Ni(111). Three clean terraces are visible. The high-symmetry directions are indicated and the linescan profile along the black line is shown on the bottom. Monoatomic step-edges with an apparent height of approximately  $2 \text{ \AA}$  are observed. Figure 4.8 b shows a high-resolution STM image of



the area indicated by the black rectangle in Fig. 4.8 a. Single C atoms of the graphene layer are observed and the unit cell is shown in blue. The linescan along the black line is shown below the STM image. A periodic corrugation with an apparent height of around 4 pm and a periodicity of approximately 2.5 Å are visible. The distance between the protrusions is in line with the nearest-neighbor distance of Ni and the unit cell of graphene. Both materials have almost the same lattice constant. [143] Graphene can have different adsorptions sites on Ni(111) which lead to different contrast in atomic resolution STM images. [141, 144] In the top-fcc adsorption configuration, which is the most abundant (60 %) [144] and also energetically most favorable geometry, [145] one graphene sublattice (A) resides on top of Ni surface atoms while the other sublattice (B) sits on fcc hollow sites. Due to this different environment underneath only C atoms sitting on top sites are observed in STM measurements. [144, 146]

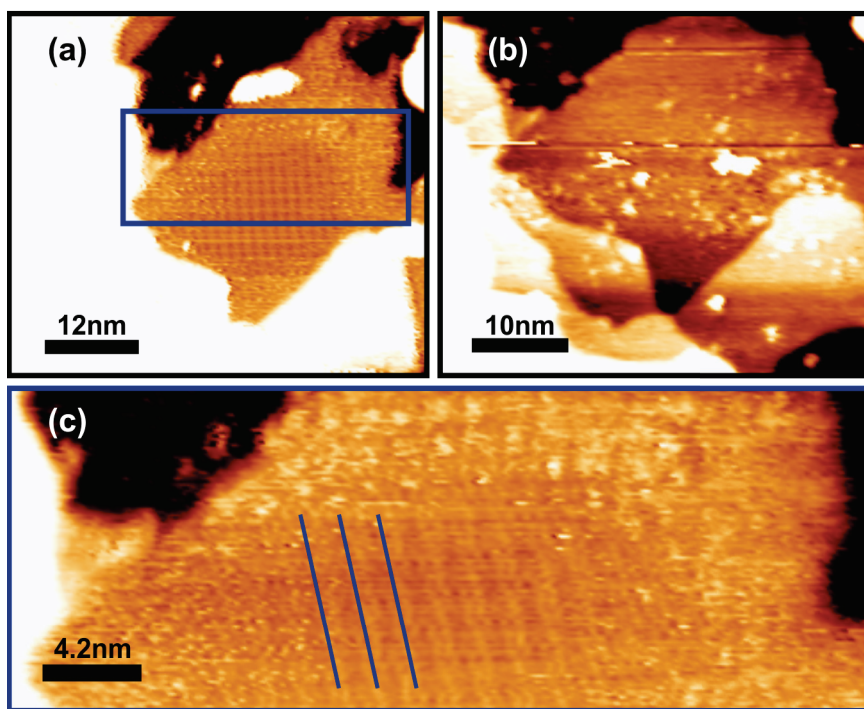


Figure 4.9: Self-assembly of TBPB on graphene/Ni(111) after annealing at 100 °C (373 K) for 15 min. (a) Typical overview STM image. An island of TBPB on a graphene/Ni(111) terrace is visible ( $U = -1.2\text{ V}$ ,  $I = 90\text{ pA}$ ). (b) The same area after small voltage pulses (1 V to 2 V) for tip preparation purposes which resulted in desintegration of the molecular network. ( $U = -0.07\text{ V}$ ,  $I = 0.1\text{ nA}$ ). (c) Zoom of the area indicated by blue rectangle in (a). Vertically running lines with 1.9 nm spacing are visible and indicated in blue ( $U = -1.2\text{ V}$ ,  $I = 90\text{ pA}$ ).

Deposition of the precursor molecules TBPB at RT leads to a similar self-assembled

#### 4.1. 2D Nanostructures via On-Surface Ullmann Coupling

structure as observed for TBPB on h-BN/Ni(111). However, it was easy to decompose the self-assembled islands with relatively small voltage pulses and thus it was difficult to obtain high-resolution STM images at RT due to the low stability. Figure 4.9 a shows a typical STM image of TBPB on graphene/Ni(111) after a gentle annealing at 100 °C (373 K) for 15 min. A self-assembled island can be observed on top of a terrace. Figure 4.9 c shows a zoom of the area indicated by the blue rectangle in Fig. 4.9 a. Vertically running lines are observed and separated by approximately 1.9 nm. The size of the spacing is similar to the size of the unit cell of TBPB self-assembled on h-BN/Ni(111) (see Fig. 4.6). Therefore, it is likely that TBPB molecules self-assemble similarly on graphene/Ni(111) and islands are also stabilized by halogen bonds. Figure 4.9 b shows the same terrace which was covered with an island of TBPB molecules in Fig. 4.9 a after small voltage pulses were applied (1 V to 2 V). The voltage pulses were applied for tip preparation purposes and already these comparatively small pulses lead to the desintegration of the molecular network. This highlights once again the limited stability of supramolecular structures.

Upon annealing between 250 °C and 300 °C (523 K and 573 K, respectively) for 15 min covalently bonded oligomers are also formed on graphene/Ni(111). The temperature range is identical to the range used for inducing covalent coupling on h-BN/Ni(111). Figure 4.10 a shows an STM image of a kinked hexamer as well as a scaled-ball-and-stick model, confirming the formation of covalent bonds between the precursor molecules TBPB. A pentamer as well as a dimer (top) and an isolated monomer are shown in Fig. 4.10 b. Figure 4.10 c shows an overview STM image of oligomers of different sizes as reaction products. Again, no long-range order is observed and only small oligomers are formed.

#### DFT Calculations and Discussion

On h-BN/Ni(111) as well as on graphene/Ni(111), frequently irregular features appearing higher than the flat oligomers were observed, which are tentatively assigned to upright standing molecules or fragments. The absence of long-range order and large polymer size on h-BN/Ni(111) and graphene/Ni(111) stands in contrast to the coinage metals, on which the same precursor molecule forms extended polymeric networks, and on which dehalogenation and C–C coupling occurs at lower temperatures. Limited mobility of the dehalogenated molecules due to a strong interaction with the surface is likely responsible for this observation, which also explains the occurrence of single molecules pinned to the surface (Fig. 4.10 b (top right) and Fig. 4.7 a (left)).

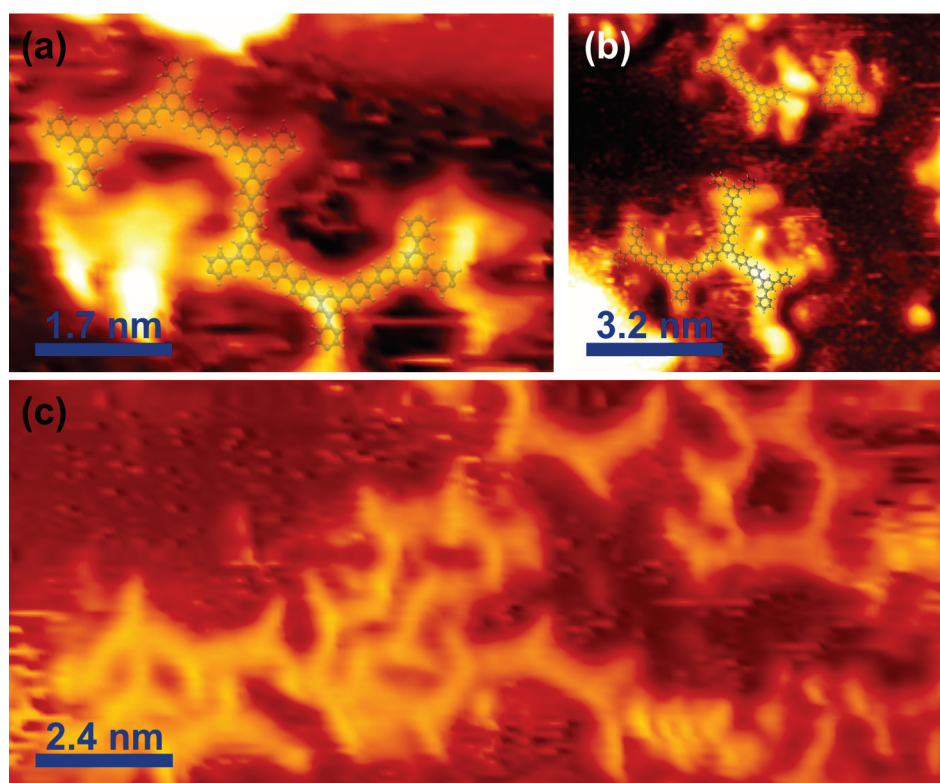


Figure 4.10: Oligomers of TBPB on graphene/Ni(111) after annealing between 250 °C and 300 °C (523 K and 573 K). (a) High-resolution STM image of a hexamer with a scaled ball-and-stick model superimposed confirming covalent bond formation ( $U = -1.3$  V,  $I = 55$  pA). (b) High-resolution STM image of different oligomers ( $U = -0.8$  V,  $I = 55$  pA). (c) Overview STM image of covalent reaction products. Oligomers of different sizes are visible with a lack of long-range order ( $U = -1.3$  V,  $I = 32$  pA).

To substantiate this hypothesis of a diffusion limited growth process Density Functional Theory (DFT) calculations were performed on the debromination of the model compound bromobenzene adsorbed on the two interfaces h-BN/Ni(111) and graphene/Ni(111). (Calculations for the actual molecule TBPB are computationally much more expensive and therefore a smaller model compound was used). Figure 4.12 presents the initial state (IS), transition state (TS), intermediate state (IntS) and final state (FS) for the dehalogenation of bromobenzene on h-BN/Ni(111). Note that the actual dehalogenation takes place between the IS and IntS, while the steps between IntS and FS are merely the diffusion of the phenyl ring and/or the bromine atom, which were not explicitly calculated. Already in the TS a boron atom (pink) is slightly lifted out of the plane of the h-BN layer and binds to the brominated carbon atom. The plane of the phenyl ring tilts away from the surface. In the IntS the split-off bromine atom binds to a neighbouring boron atom, which is also slightly lifted. In the FS, the

#### 4.1. 2D Nanostructures via On-Surface Ullmann Coupling

phenyl ring and the bromine atom are well separated, enabling both species to adapt a more favorable adsorption configuration. The dehalogenation reaction is exothermic (an energy of 0.41 eV is released) with an energy barrier of 1.51 eV. This value is higher than the energy values calculated for bromobenzene on Cu(111), Ag(111) and Au(111), which range between 0.66 eV and 1.02 eV. [122] The dehalogenation barrier correlates with the annealing temperatures used to induce C–C coupling of TBPB on h-BN/Ni(111). Taking the Arrhenius equation  $k = \nu \cdot \exp(-E_A / (k_B T))$ , where  $k$  is the reaction rate,  $\nu$  a pre-exponential factor assumed to be  $1 \times 10^{13} \text{ s}^{-1}$ ,  $E_A$  the activation energy (energy barrier) and  $k_B T$  is the thermal energy with Boltzmann's constant  $k_B$  and  $T$  the applied temperature, 312 °C (585 K) is required to achieve a reaction rate of  $k = 1 \text{ s}^{-1}$ , close to the maximum annealing temperatures of 300 °C (573 K). Figure 4.11 a shows the reaction rate as a function of temperature. The range of annealing temperatures used in the experiments is indicated by the blue shaded area. The temperatures result in reasonable high reaction rates considering the experimental annealing times of approximately 15 min. The calculated barrier is three times larger than the experimentally obtained activation energy of TBPB on Cu(111), [147] presumably a consequence of the damping of the Ni d levels due to the decoupling layer. Notably, DFT calculations showed that following a similar path as on the Ni-supported surface, the reaction is not possible on the free standing h-BN sheet, demonstrating the active role of the underlying metal surface in the catalytic dissociation reaction.

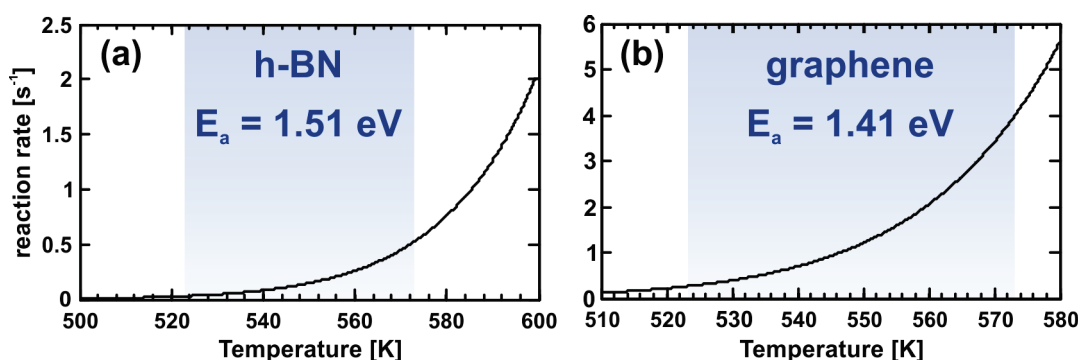


Figure 4.11: Arrhenius plots for debromination with barriers calculated for bromobenzene on (a) h-BN/Ni(111) and (b) graphene/Ni(111). The temperature range used in the experiments is highlighted in blue. The reaction rates were obtained assuming a pre-exponential factor of  $1 \times 10^{13} \text{ s}^{-1}$ . The energy barriers for debromination of bromobenzene on h-BN/Ni(111) and graphene/Ni(111) obtained by DFT calculations are indicated.

The perpendicular adsorption of the dehalogenated molecule (Fig. 4.12 a, FS) is an indicator of a strong chemical coupling between carbon and boron atoms (approx-

imately 2.5 eV, see below). This strong interaction results in a significantly reduced mobility of the molecules on the surface and explains the absence of large polymers. The diffusion barrier is calculated to be approximately 1.90 eV for the fully debrominated TBPB on the h-BN/Ni(111) surface. This barrier is smaller by 0.3 eV than the barrier of the cyclohexa-*m*-phenylene radical on Cu(111), for which larger polymers than those observed here are formed. [136] Debrominated phenyl has a diffusion barrier of 1.70 eV on h-BN/Ni(111) and is substantially larger than on the coinage metal surfaces, which range between 0.05 eV and 0.20 eV. [122] The large diffusion barrier stems from the highly unfavorable binding of the phenyl rings to boron (B) atoms in the TS. It was previously pointed out that a balance of diffusion and coupling rates governs the formation of branched oligomers or regular polymers. [30, 136] In a diffusion-limited process, where the coupling rate is much larger compared to the diffusion rate, [148] disordered, branched oligomers dominate. Taking into account the large diffusion barrier for the dehalogenated molecules calculated by DFT, a diffusion-limited growth process on the decoupling layer leading to small oligomers as observed in the experiments is very likely. Based on the upright adsorption geometry of the phenyl unit in the FS, the observed unusual bright (and high) protrusions can tentatively be attributed to vertically standing molecular fragments.

The DFT calculations for bromobenzene on graphene/Ni(111) show very similar results. Figure 4.12 c (red) sketches the reaction pathway for debromination. The carbon atom of graphene that binds to bromobenzene is also slightly lifted and the reaction is endothermic by 0.07 eV. The energy barrier of 1.41 eV is comparable to the value of bromobenzene on h-BN/Ni(111), and is in line with the theoretical annealing temperature of 273 °C (546 K) suggested by the Arrhenius equation to achieve a reaction rate  $k$  of  $1 \text{ s}^{-1}$ . Figure 4.11 b shows the reaction rate as a function of temperature. The blue shaded area indicates the range of annealing temperatures used in the experiments. The experimental annealing times of approximately 15 min thus result in sufficiently high reaction rates. The DFT calculations also show a strong interaction between the phenyl unit and graphene/Ni(111), which again explains the absence of larger oligomers/polymers due to the significantly reduced diffusion of debrominated TBPB molecules. For the bromobenzene dissociation on both h-BN/Ni(111) and graphene/Ni(111), the phenyl ring in the TS interacts strongly with the respective surface in the absence of any substantial bromine-surface interaction (see Fig. 4.12 (a) and (c), TS side view). Reminiscing the comparable energy barriers for the two surfaces, also the adsorption energies of phenyl are very similar (−2.52 eV and −2.54 eV on h-BN/Ni(111) and graphene/Ni(111), respectively). This indicates that the strength of the phenyl-surface bond formation drives the debromination, and thus controls the energy barrier of the reaction. Furthermore, the origin of diverging reaction energies between the surfaces – exothermic by −0.41 eV for h-BN/Ni(111) versus slightly



#### 4.1. 2D Nanostructures via On-Surface Ullmann Coupling

endothermic by 0.07 eV for graphene/Ni(111) – can be found in different adsorption energies of bromine;  $-2.43$  eV on h-BN/Ni(111) and  $-1.85$  eV on graphene/Ni(111), illustrating the importance of the interaction of both the phenyl as well as the split-off bromine atoms with the surface in the FS. Additional calculations reveal that the cleavage of the C–Br bond on freestanding graphene has a barrier of 2.85 eV, 1.4 eV larger than on graphene/Ni(111). This underlines the catalytic relevance of the supporting Ni(111) crystal for the dehalogenation reaction on both h-BN and graphene, respectively.

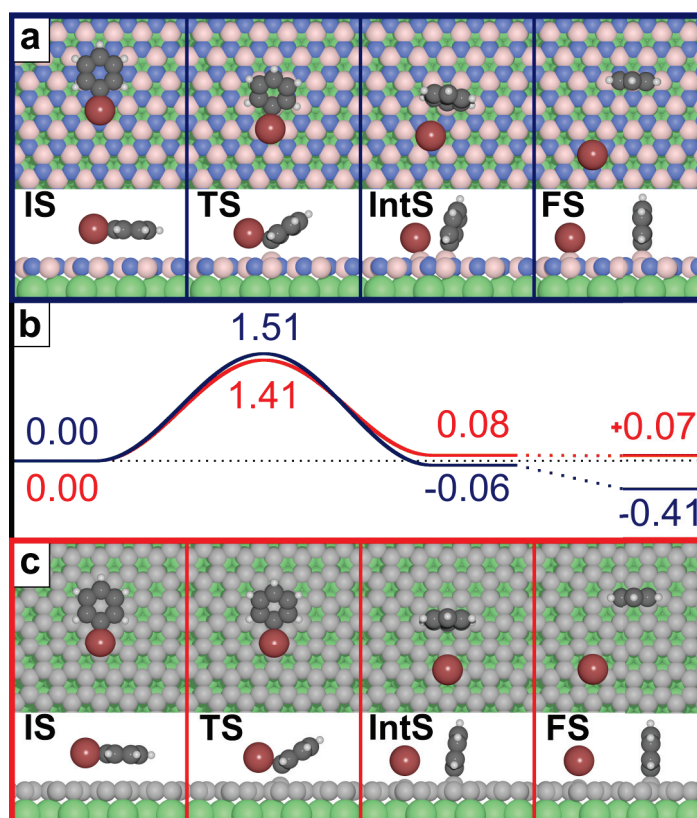


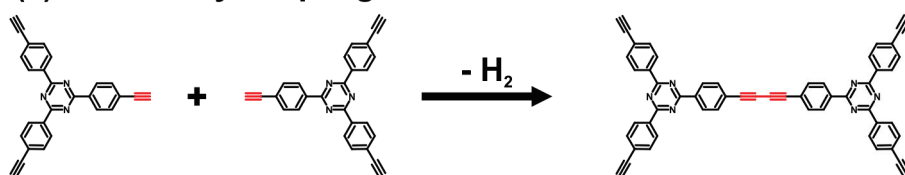
Figure 4.12: Debromination reaction pathway of the model compound bromobenzene. Initial state (IS), transition state (TS), intermediate state (IntS) and final state (FS) of debromination on (a) h-BN/Ni(111) and (c) graphene/Ni(111). (b) Energy diagram of the reaction on h-BN/Ni(111) in blue and on graphene/Ni(111) in red. Both substrates exhibit a debromination barrier between approximately 1.4 eV and 1.5 eV. Values in eV. (Grey: carbon, white: hydrogen, brown: bromine, blue: nitrogen, light pink: boron, green: nickel.)

In summary, in this section h-BN and graphene single layers grown on Ni(111) are presented as substrates for the growth of covalent 2D nanostructures in the form of



oligophenylene. A strong interaction between dehalogenated molecules and decoupling layer results in limited mobility and inhibits the growth of polymers with large spatial extension. The large diffusion barrier of surface-stabilized radicals might be a fundamental limitation for the growth of (ordered) polymers on h-BN and graphene in UHV. However, a suitable choice of supporting metal surface for h-BN and graphene or solution-based approaches might improve the order and spatial extension of the polymers.

**(a) Glaser-Hay coupling:**



**(b) Cyclotrimerization:**

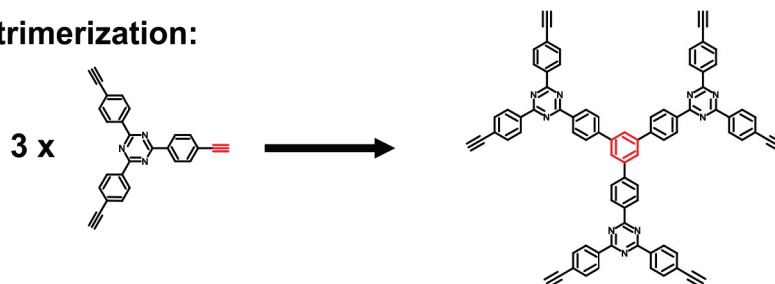


Figure 4.13: Reaction scheme of (a) Glaser-Hay coupling and (b) Cyclotrimerization of terminal alkynes. The precursor molecule TEPT consists of a triazine core connected with three ethynylphenyl groups at carbon atoms of position 1, 3 and 5. The ethynyl group which forms a new bond is highlighted in red.

## 4.2 Homo-(Glaser)-Coupling and Cyclotrimerization of Alkynes on Au(111)

In the previous section the surface-assisted Ullmann reaction was presented. Upon annealing C–Br bonds are cleaved due to their lower stability and the carbon atoms left behind serve as reactive sites for C–C bond formation. Split-off halogen atoms usually stay on the surface and can potentially contaminate it. In this section an alternative on-surface coupling reaction is presented. In this reaction precursor molecules are arylalkynes and alkynyl groups act as reactive sites. Figure 4.13 shows schemes of two reaction mechanisms which occur on Au(111). First, in the Glaser coupling [149, 150] alkynyl groups are dehydrogenated and volatile H<sub>2</sub> is produced along with the conjugated polymer as main reaction product. The second reaction

## 4.2. Homo-(Glaser)-Coupling and Cyclotrimerization of Alkynes on Au(111)

mechanism, cyclotrimerization, uses three alkynyl groups to form a new phenyl ring (bonds/atoms participating in the reaction are highlighted in red). Klappenberger et al. published recently a comprehensive review on surface-assisted reactions based on terminal alkynes. [151] In the following both on-surface reactions are presented with the non-commercially available precursor molecule 1,3,5-tris(4-ethynylphenyl)-s-triazine (TEPT). [152] A chemical formula of this molecule is also shown in Fig. 4.13.

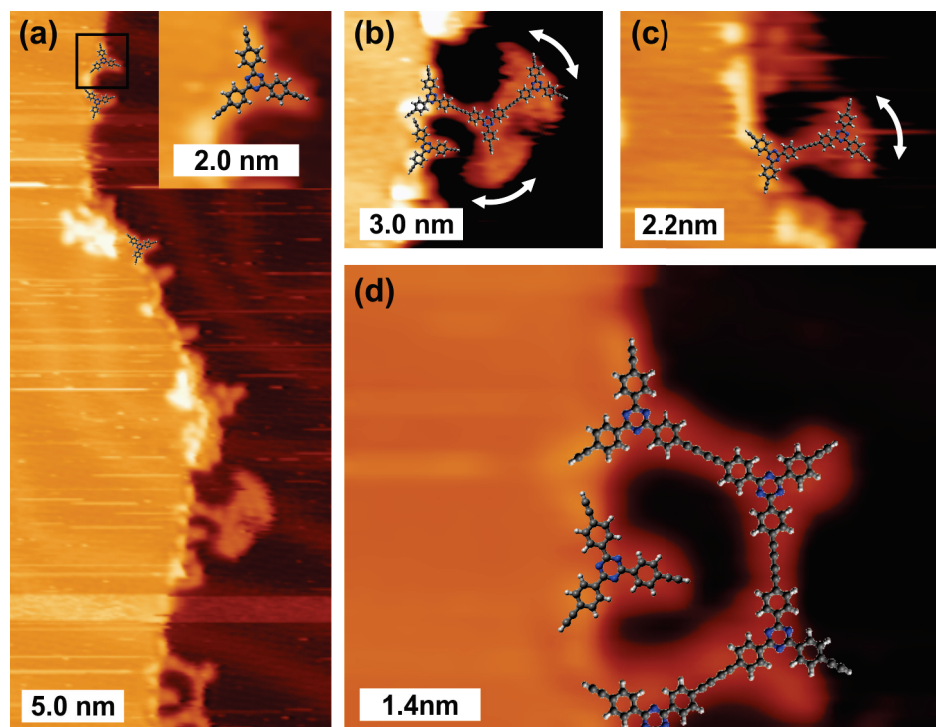


Figure 4.14: Glaser-Coupling of TEPT on Au(111). (a) Step-edge decoration of molecules. Reaction products are visible in the lower part. A trimer and a tetramer can be observed. Inset shows a high-resolution STM image of the adsorption of TEPT at the Au(111) step-edge. (b) and (c) High-resolution STM images of reaction products of TEPT after deposition on Au(111) held at 200 °C (473 K). Small interaction with the substrate and flexible butadiyne bridges ( $-C\equiv C-C\equiv C-$ ) allow for motion of oligomers anchored at the step-edge (white arrows). (d) A tetramer is adsorbed at a step-edge (also visible in (a)). A scaled ball-and-stick model fits well and confirms covalent bond formation. ( $U = -0.86\text{ V}$ ,  $I = 0.1\text{ nA}$ ).

### 4.2.1 Homo-(Glaser)-Coupling of Arylalkynes

Since historically the Glaser-coupling is based on cuprous salts like copper(I) chloride or copper(I) bromide, strictly speaking the on-surface reaction of arylalkynes should not be called Glaser-coupling due to the absence of salts. In the following,

however, the homo-coupling of arylalkynes is still called Glaser-coupling because the reaction educts and products are very similar. Zhang et al. reported the on-surface Glaser-coupling reaction on Ag(111) under ultra-high vacuum conditions for the first time in 2012. [153] They used a trigonal precursor molecule with three terminal alkynyl groups to form conjugated 2D polymers. Eichhorn et al. used a linear precursor molecule, 1,4-diethynylbenzene (DEB), to synthesize polymeric structures on Cu(111), [117] while Gao et al. tried to optimize the reaction yield of alkynes on various metal surfaces with the help of steric hindrance to suppress side reaction pathways. [118] It turns out that on Ag(111) highest selectivity for on-surface Glaser coupling can be achieved while on Au(111) also cyclotrimerization occurs. [154, 155] Cyclotrimerization is presented in more detail in the next section. Finally, there are also attempts to induce homo-coupling reactions of arylalkynes (Glaser-coupling) with light, [119] since photochemical approaches represent orthogonal processes to thermally induced on-surface reactions.

In this study a non-commercial precursor molecule 1,3,5-tris(4-ethynylphenyl)-s-triazine (TEPT) consisting of a s-triazine core with three ethynylphenyl side-groups (see Fig. 4.13 for chemical formula) was used. The s-triazine core, which is a phenyl ring with three carbon atoms replaced by three nitrogen atoms, results in a vanishing dihedral angle between the central triazine core and peripheral phenyl rings. [156] Furthermore, this leads to polymers with better  $\pi$ -conjugation. [17] Additionally, due to the heteroatomic precursor molecule the electronic structure of the polymers formed out of TEPT will also be altered. Especially the polymers formed by cyclotrimerization have alternating connections consisting of ordinary phenyl rings and nitrogen doped triazine cores (see next section, Fig. 4.15 d).

Depositing a submonolayer amount of TEPT onto Au(111) held at 200 °C (473 K) induces homo-coupling of TEPT. Figure 4.14 a shows an overview STM image of the reaction products. Besides the herringbone construction of Au(111), [157] precursor molecules as well as oligomers can be observed. Single molecules are preferentially adsorbed at step-edges (inset of Fig. 4.14 a). Furthermore, the interaction between reaction products (oligomers) and the gold substrate is small which becomes visible in Fig. 4.14 b and c. Since the scanning speed of the STM tip is slow compared to the movement of the oligomer leg a superposition of the whole movement is observed which results in a cone-like feature in STM images. [158] Additionally, butadiyne bridges ( $-C\equiv C-C\equiv C-$ ) are flexible which facilitates the motion. Fig. 4.14 d shows a close-up STM topographic image of a tetramer (an almost complete hexagonal ring). Two TEPT molecules are missing to form a hexagon. The opening is connected to a step-edge and two molecules are adsorbed at it. Close inspection reveals that the half hexagonal ring is subject to a small compression. The exact adsorption site could not

## 4.2. Homo-(Glaser)-Coupling and Cyclotrimerization of Alkynes on Au(111)

be resolved. However, atomic resolution STM image should resolve this issue. In the next section the second pathway – cyclotrimerization – is presented.

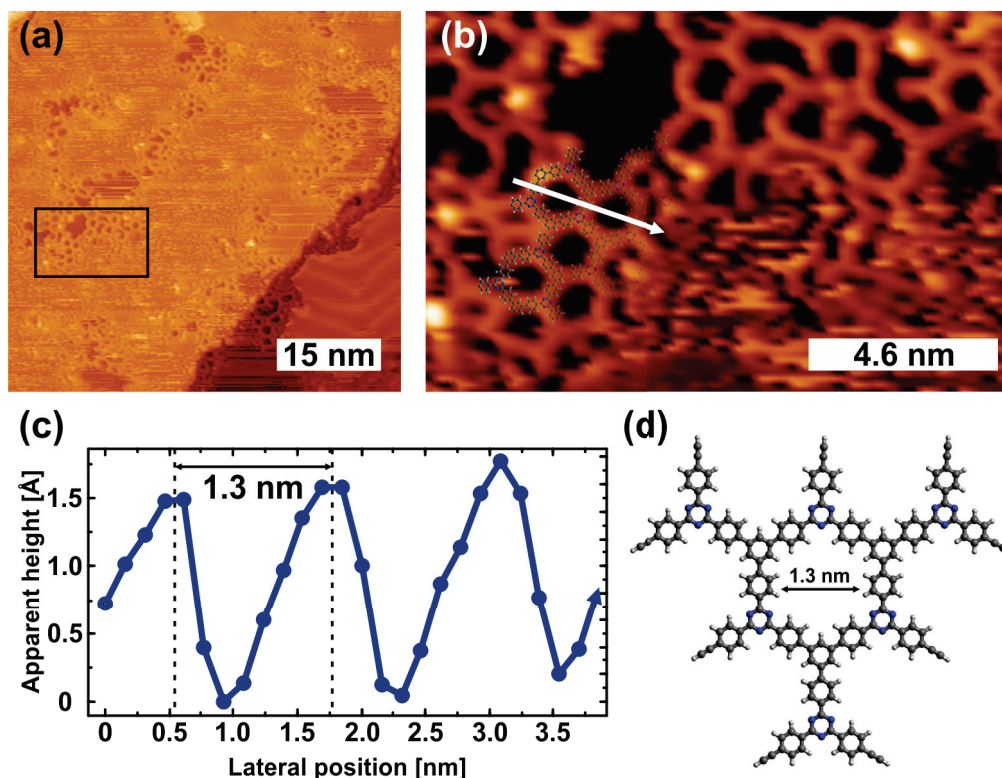


Figure 4.15: Cyclotrimerization of TEPT on Au(111). (a) Overview STM image of reaction products after deposition of TEPT onto the surface held at 200 °C (473 K). Herringbone reconstruction of Au(111) is also visible on the right. (b) High-resolution STM image of polymers. Scaled ball-and-stick model is superimposed ( $U = -0.9$  V,  $I = 32$  pA). (c) Linescan along the white line/arrow in (b) confirms the cyclotrimerization and covalent nature of the bonds. A pore-to-pore distance of 1.3 nm agrees well with gas-phase DFT calculations. (d) Ball-and-stick model of parts of 2D polymer, which forms out of TEPT via cyclotrimerization. The pore size is also indicated.

### 4.2.2 Cyclotrimerization of Terminal Alkynes

When the coverage of TEPT molecules is increased, reaction products due to cyclotrimerization (see Fig. 4.13 b) can also be observed. Figure 4.15 shows reaction products of TEPT after deposition onto Au(111) held at 200 °C (473 K). Due to the higher coverage of precursor molecules reaction products originating from cyclotrimerization as reaction pathway can be observed on Au(111). Fig. 4.15 a shows an overview STM image while Fig. 4.15 b shows a zoom of the area indicated in Fig. 4.15(a), black

rectangle. A scaled ball-and-stick model of the polymer fits well and confirms the covalent bonds that are formed. Additionally, Figure 4.15 c presents a linescan along the white line/arrow shown in Fig. 4.15 b. A pore-to-pore distance of approximately 1.3 nm can be measured and is in good agreement with gas-phase DFT calculations. Figure 4.15 d shows part of the 2D polymer that forms out of TEPT via cyclotrimerization. As already mentioned, three alkynyl groups react and form a new phenyl ring. This results in a 2D polymer, which has connection points consisting of these newly formed phenyl rings as well as triazine cores present because of the backbone of the precursor molecules. With the STM data at hand no differences within the 2D network could be observed. However, by functionalizing the STM tip it might be possible to obtain submolecular resolution and triazine cores can be differentiated from phenyl rings. Additionally, it could be interesting to introduce specific guest molecules, which are Lewis acids (electron pair acceptor) and bind preferentially to nitrogen (N) atoms within the triazine cores resulting in highly selective host-guest interactions. Furthermore, mapping the local density of states (LDOS) might also provide insight into the location of triazine cores. Similar heteroatomic 2D polymers have recently been synthesized by Sánchez-Sánchez et al. in the context of porous graphene. [159]

### 4.3 2D Polymer Synthesis via On-Surface Decarboxylation Reaction

As mentioned in the previous sections, on-surface Ullmann coupling is widely used for surface-assisted synthesis of two-dimensional (2D) polymers. However, other coupling mechanisms mainly inspired from solution chemistry are investigated on various metal surfaces in ultra-high vacuum conditions. The on-surface Glaser-coupling has been shown in the previous section. In this section the metal surface-assisted decarboxylation reaction is presented. The on-surface decarboxylation reaction was first studied by Gao et al. in the context of one-dimensional (1D) conjugated polymers. [120] They used 2,6-naphthalenedicarboxylic acid as precursor molecule and studied reaction products by means of STM. They find that the reaction works most efficiently (best reaction yield) on Cu(111). In this section complementary experimental tools are used to illuminate the surface-assisted decarboxylation of a commercially available precursor molecule in a comprehensive way. STM, XPS and DFT calculations are used to understand the reaction mechanism thoroughly while the electronic properties of monomers as well as polymers are accessed by STS, UPS and DFT calculations. The precursor molecule is similar to the one used in Section 4.1. 1,3,5-tris(4-carboxyphenyl)benzene (TCPB) is a carboxylic acid consisting of a benzene



### 4.3. 2D Polymer Synthesis via On-Surface Decarboxylation Reaction

core with three legs each containing one carboxyl group. A chemical formula is shown in Fig. 4.16 a.

When a sub-monolayer amount of the precursor molecule TCPB is deposited onto Cu(111) at room temperature (RT) the molecules self-assemble and form islands constituting a  $(3\sqrt{3} \times 3\sqrt{3})R30^\circ$  superstructure. Each molecule can be recognized as a trigonal protrusion. Figure 4.16 a shows a typical STM topograph of the self-assembly. Taking into account the well-known deprotonation of carboxylic acids on copper surfaces at RT, [92, 97, 160] one tripodal protrusion can be assigned to a deprotonated molecule. The self-assembled structure is stabilized by ionic hydrogen bonds between deprotonated and (partially) negatively charged oxygen atoms and hydrogen atoms of neighboring molecules. [161, 162] In addition, Figure 4.17 shows the LEED pattern of clean Cu(111) as well as of a monolayer of TCPB on Cu(111). One can observe the typical diffraction pattern for a  $(3\sqrt{3} \times 3\sqrt{3})R30^\circ$  superstructure.

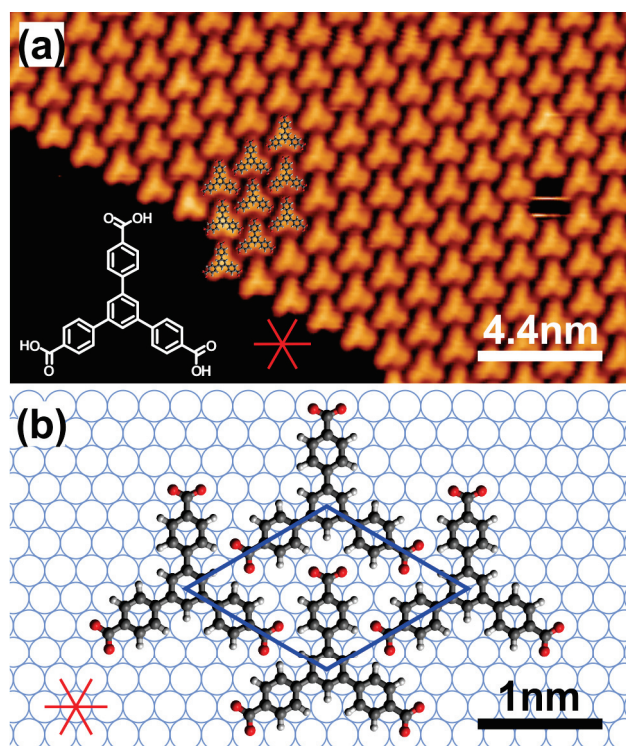


Figure 4.16: Self-assembly of 1,3,5-tris(4-carboxyphenyl)benzene (TCPB) on Cu(111) after deposition at room temperature. (a) STM topograph of TCPB (chemical formula in lower left corner). Tripodal features can be assigned to deprotonated TCPB molecules. High-symmetry directions of Cu(111) surface are indicated in red ( $U = -1$  V,  $I = 0.1$  nA). (b) Ball-and-stick model of TCPB arranged as  $(3\sqrt{3} \times 3\sqrt{3})R30^\circ$  superstructure on Cu(111) (blue circles represent accordingly scaled Cu atoms).



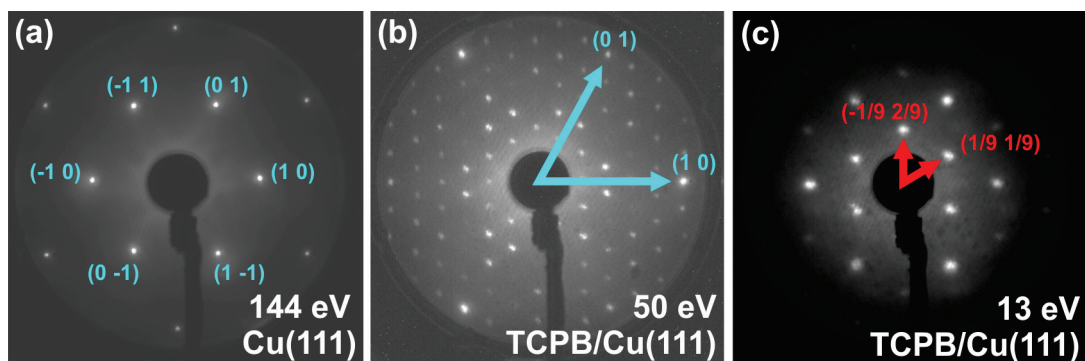


Figure 4.17: Low Energy Electron Diffraction (LEED) pattern of (a) clean Cu(111) taken with an incident electron energy of 144 eV, and (b) a monolayer of TCPB adsorbed on Cu(111) at room temperature taken with 50 eV electron energy. The spots of the  $(3\sqrt{3} \times 3\sqrt{3}) R30^\circ$  superstructure are visible as well as the pattern of Cu(111) (indicated in cyan). (c) Low-energy LEED pattern observed with incident electron energy of 13 eV. The reciprocal lattice of the superstructure formed by TCPB is indicated in red.

To promote coupling reactions the Cu(111) surface with sub-monolayer coverage of the precursor molecule TCPB was annealed at 180 °C for 15 min. Figure 4.19 a and b show STM images of the resulting reaction products. With a bias voltages of –1.5 V, hexagonal structures (lower left) as well as heptagonal and pentagonal structures (upper right) are visible without any substructure (Fig. 4.19 a). However, for a bias voltage of –0.5 V, circular protrusions between the linear connections of the molecules become visible (Fig. 4.19 b). Geometric considerations suggest that the carboxylate groups of the monomers have split off (most-likely in form of volatile CO<sub>2</sub>) and that the bright protrusions can be assigned to copper (Cu) adatoms resting in between two decarboxylated TCPB molecules in an organometallic network. The same organometallic structures are observed on Cu(111) [130, 163] and Ag(111), [164] where Cu/Ag adatoms likewise appear as circular protrusions. Notably, one covalent bond between two precursor molecules is observed – indicated by an absence of the circular protrusion (white arrow in Fig. 4.19 a and b) – highlighting the statistical occurrence of a covalent-bond formation at the given temperature. The sample was annealed at higher temperatures namely at 220 °C (493 K) for 15 min to create additional covalent bonds between the decarboxylated molecules. Figure 4.19 c shows an overview STM image of the reaction products in the form of hexagonally ordered structures. A ball-and-stick model of the corresponding 2DP [130] (polyphenylene, extended porous graphene) is superimposed and fits well with the observed features (Fig. 4.19 d). A pore-to-pore distance of 2.2 nm is in agreement with DFT calculations and values reported in literature [30, 130] and thus confirms the covalent nature of the obtained polymers. Alongside the ordered oligomers, disordered reaction products

### 4.3. 2D Polymer Synthesis via On-Surface Decarboxylation Reaction

can be observed (Fig. 4.19 c). Figure 4.19 e shows a high-resolution STM image of these structures, in which pores can be observed both shape and size resembling those of fused polyphenylene rings in porous graphene (pore-to-pore distance of 7.3 Å). [135] The formation of these structures can be understood by assuming a chemical modification of the original reactive site (where a carboxyl group was originally connected to the molecule) through either C–H activation of phenyl rings or by tautomerization of hydrogen atoms along the rim of phenyl rings. [165] Figure 4.19 f depicts a ball-and-stick model in which precursor monomers are coloured in alternating grey and red, and on which hydrogen atoms from meta-positions on the peripheral phenyl rings have changed their location to para-positions. For comparison, aryl-aryl coupling via C–H activation of quarterphenyl on Cu(110) takes place at 227 °C (500 K), [166] and intra-molecular cyclodehydrogenation of polyanthylenes on Cu(111) takes already place at 200 °C (473 K). [167] Hydrogen abstraction on the phenyl rings at 220 °C (493 K) annealing temperatures is thus a viable hypothesis that explains the frequent observation of undesired side products.

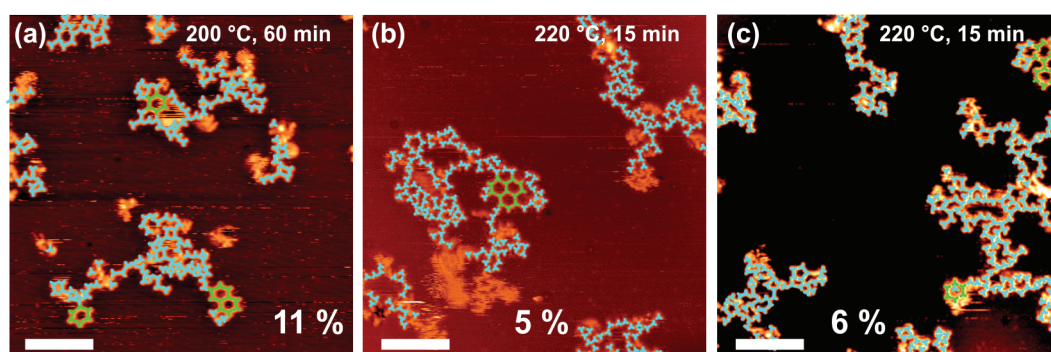


Figure 4.18: STM images of reaction products with single TCPB molecules superimposed for the derivation of reaction yields. Cyan tripods indicate molecules that do not participate in the desired reaction products while green tripods highlight molecules that are involved in polyphenylene as desired reaction product. The corresponding reaction yields are indicated. (a) Reaction yield accounts for 11 %. (b) 5 % of total TCPB molecules are involved in polyphenylene formation. (c) Reaction yield constitutes 6 %. The average reaction yield accounts for 7 %. The scale bar is 5 nm in each STM image.

Statistical analyses of STM images give insight into the reaction yield. Figure 4.18 shows three STM images with reaction products after annealing TCPB molecules on Cu(111). The annealing temperatures and times are shown. The total number of molecules in each STM image was counted. Subsequently the number of molecules participating in the desired structures (polyphenylene, extended porous graphene) was also counted. Finally, with the numbers in hand the reaction yield was calculated.

They are indicated in Fig. 4.18. The analysis gives an average reaction yield of 7 %.

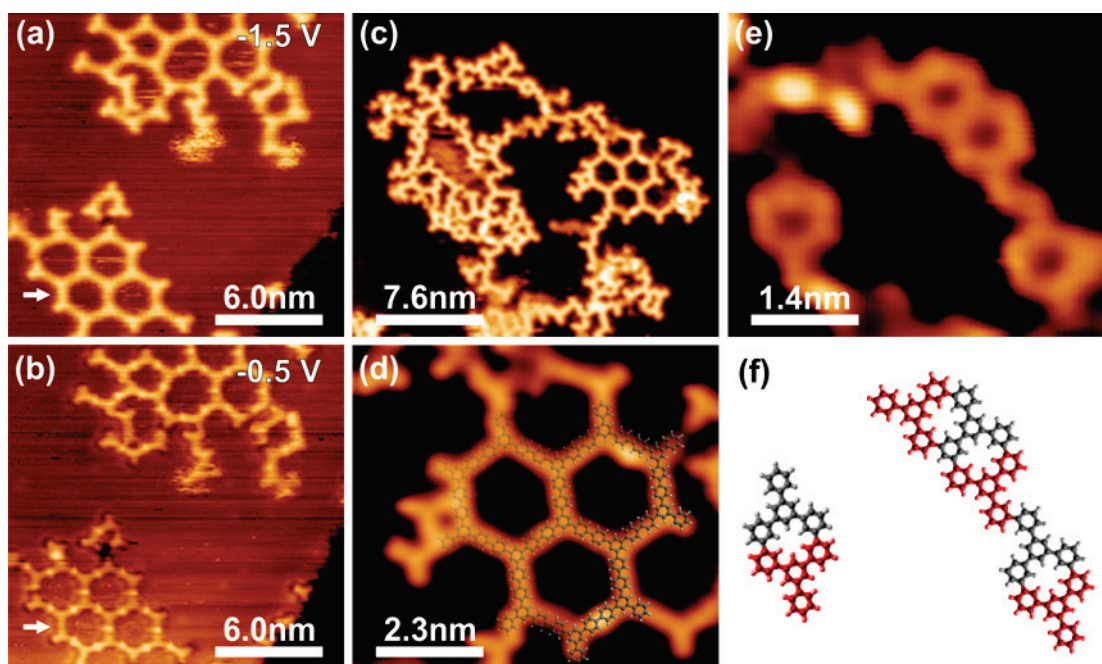


Figure 4.19: STM images of organometallic and covalent structures. (a) and (b) show organometallic structures after annealing at 180 °C (453 K) for 15 min. (a)  $U = -1.5$  V,  $I = 60$  pA and (b)  $U = -0.5$  V,  $I = 60$  pA. Cu adatoms are visible as circular protrusions. The white arrow indicates a covalent bond. (c) Covalent nanostructures obtained after annealing at 220 °C (493 K) for 15 min ( $U = -1$  V,  $I = 10$  pA). (d) High-resolution STM image of extended-porous graphene with a scaled ball-and-stick model superimposed confirming the covalent bond formation. (e) High-resolution STM image of side products resembling fused polyphenylene rings ( $U = -1.5$  V,  $I = 60$  pA). (f) Hypothetical ball-and-stick model of polyphenylene structures that form out of TCPB monomers (shown in red and grey alternatingly).

The hypothesized decarboxylation of TCPB prior to polymerization is further evidenced by X-ray photoelectron spectroscopy (XPS) measurements. Figure 4.20 shows the carbon (C) 1s region of a (sub)monolayer TCPB deposited onto Cu(111) at RT. The experimental data points are shown as blue circles and the corresponding fit is shown in black. It consists of two Voigt functions (green) whereby one peak lies at high binding energy (287.5 eV) and the other has its maximum at 284.3 eV. The low binding energy peak is assigned to the carbon atoms in the phenyls and the high binding energy peak is related to the carbon atoms in the carboxylates. This is consistent with calculated core-level shifts of the model compound biphenyl-4-carboxylic acid

### 4.3. 2D Polymer Synthesis via On-Surface Decarboxylation Reaction

and with XPS studies on other carboxylic acids. [160, 161, 168–170] After annealing the sample at 220 °C (493 K) for 15 min the high binding energy peak at 287.5 eV disappears (Fig. 4.20 b) and the integrated intensity of the low binding energy peak at 284.3 eV is reduced only by 0.5 %. This implies that carbon atoms of the carboxylate leave the surface. Figure 4.20 c shows the corresponding oxygen (O) 1s spectra. Only one oxygen peak at 530.8 eV is observable at RT (blue circles), which vanishes after annealing at 220 °C (493 K) (red circles), and stems from the oxygen of the carboxylate. For comparison, the O 1s peak of deprotonated terephthalic acid lies at 531.4 eV. [160]

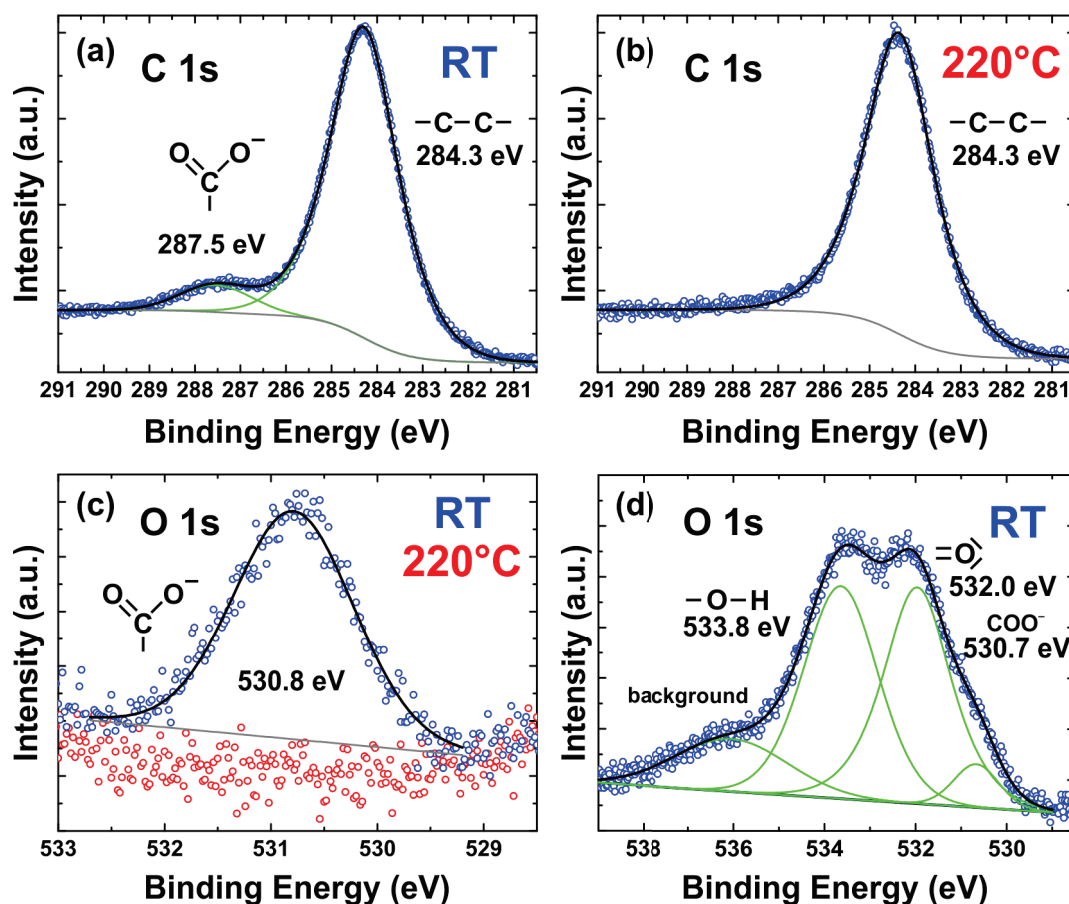


Figure 4.20: XPS spectra of the C 1s and O 1s core-levels. (a) C 1s peak obtained after deposition of a (sub)monolayer TCPB at RT. (b) C 1s peak after annealing at 220 °C (493 K). (c) O 1s peak after deposition of a monolayer TCPB at RT (blue) and after annealing at 220 °C (493 K) (red). (d) O 1s peak after deposition of nominally six layers of TCPB at RT.

Multilayer of TCPB were created by a nominally six times larger deposition time. The corresponding O 1s multilayer spectra of molecules deposited at RT are shown in Figure 4.20 d, experimental data points as blue circles and black lines correspond to fit



consisting of four Voigt functions (green lines). The peak with highest binding energy originates from the substrate (background). The high binding energy peak situated at 533.8 eV is assigned to the oxygen in the hydroxyl groups ( $-O-H$ ) and the low binding energy peak at 532.0 eV stems from oxygen in the carbonyl groups ( $-C=O$ ) consistent with literature. [160, 161] Both peaks have the same integrated intensity. The low binding energy peak at 530.7 eV can be assigned to oxygen atoms in carboxylates of deprotonated molecules close to the Cu(111) surface and accounts for 6 % of the total integrated intensity.

Finally, XPS data revealed the disappearance of the monolayer carboxylate oxygen peak together with the vanishing high binding C 1s peak after annealing results from the desorption of both species from the surface most-likely in the form of volatile  $CO_2$ .

So far the on-surface decarboxylation reaction was illuminated experimentally by means of Scanning Tunneling Microscopy and X-ray Photoelectron Spectroscopy. To gain further insight into the decarboxylation reaction pathway, the reaction is also investigated by Density Functional Theory (DFT) calculations. For this purpose the model compound biphenyl-4-carboxylic acid is used since it is computationally faster to study smaller molecules. Figure 4.21 shows the initial state (IS), transition state (TS) and final state (FS) of the decarboxylation reaction on a bare Cu(111) surface (Fig. 4.21 a), and involving a Cu adatom (Fig. 4.21 c). The free energy profiles of the decarboxylation reactions are shown in Fig. 4.21 b. The calculations include vibrational enthalpy and entropy evaluated at 180 °C (453 K) in addition to the potential energy. In both cases, the energies are given with respect to the initial state (IS) of the reaction without adatom, such as the energy of the IS of the adatom-assisted reaction shows the interaction strength between the molecule and an isolated adatom on the surface. In both cases the reaction is endothermic with free energy barriers of 1.18 eV and 1.41 eV without and with a Cu adatom, respectively. These values agree well with the annealing temperatures used to induce decarboxylation and C–C coupling of TCPB on Cu(111). Assuming that the reaction is described by the Eyring equation, 138 °C (411 K) and 204 °C (477 K) is required to achieve a reaction rate of  $1 \text{ min}^{-1}$  for the model system without and with adatom, respectively. The overall lower energy in the adatom-carboxylate system, together with the availability of Cu adatoms at the terraces at elevated temperatures, [171] makes the adatom-assisted decarboxylation path more likely. Diffusing adatoms on the Cu(111) surface will likely bind to the carboxylates upon thermal annealing before the decarboxylation becomes energetically feasible and therefore the population of the initial state of the reaction pathway with Cu adatom is higher by several orders of magnitude. This is substantiated by the experimental observation of coordinated Cu atoms in-between two decarboxylated molecules in the organometallic network (see Fig. 4.19 b).

### 4.3. 2D Polymer Synthesis via On-Surface Decarboxylation Reaction

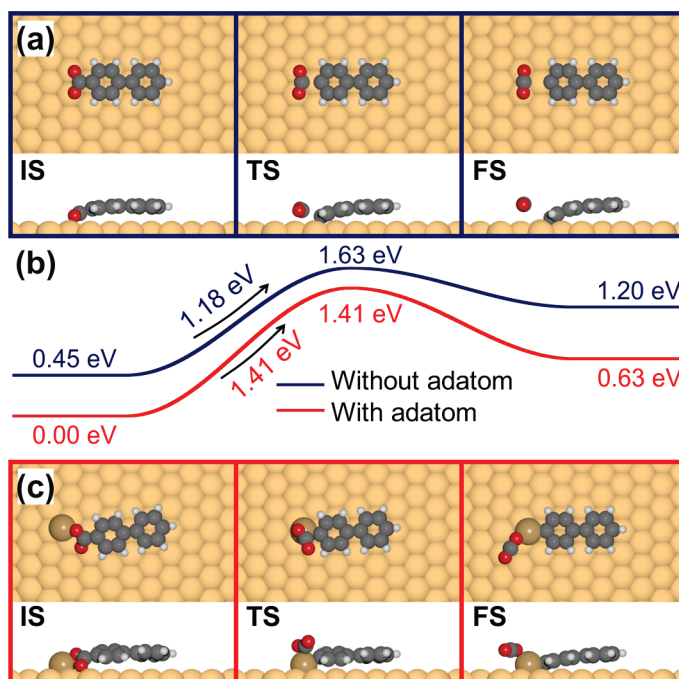


Figure 4.21: Top and side views of initial state (IS), transition state (TS) and final state (FS) of the decarboxylation reaction of model compound biphenyl-4-carboxylic acid (a) without a Cu adatom (blue) and (c) with a Cu adatom (red). Free energy profiles of the two reactions are shown in (b). Calculations include vibrational enthalpy and entropy at 180 °C (453 K). Both reaction pathways are endothermic with free energy barriers between 1.18 eV (without Cu adatom) and 1.41 eV (with Cu adatom). (Grey: carbon, white: hydrogen, red: oxygen, brown: copper)

Figure 4.20 d showed the O 1s core-level of nominally six layers of TCPB on Cu(111). In the following the effect of post-annealing of the multilayer system is presented. Figure 4.22 shows the XPS C 1s data on nominally six layers of TCPB deposited on Cu(111) (a) at RT and (b) after post-annealing at 220 °C (493 K). The XPS spectrum taken of as-deposited TCPB molecules at RT (Fig. 4.22 a) exhibits three peaks. The intense peak with low binding energy of 284.8 eV can be assigned to carbon (C) atoms in phenyls while the high binding energy peak at 289.0 eV corresponds to C atoms of intact carboxyl groups (–COOH). The peak at binding energy of 291.3 eV might be due to a  $\pi$ - $\pi^*$  transition resulting in a broad shake-up peak. The intensity ratio is in accordance with the number of contributing C atoms within one molecule:  $3/27 = 11\%$  in carboxyl groups and  $24/27 = 89\%$  in phenyl rings. Figure 4.22 b shows the sample after post-annealing at 220 °C (493 K). The overall intensity (area under all peaks) shrinks by 25 % suggesting partial desorption of intact molecules. In addition, a new peak at 287.6 eV appears, which is attributed to carbon atoms in carboxylates (see



also Fig. 4.20 a with a monolayer of TCPB). The intense low energy peak with binding energy of 284.5 eV, which is associated with C atoms in phenyl rings, still accounts for roughly 89 % of the total area while the smaller high binding energy signals at 289 eV and 287.6 eV, respectively, account for 11 %. Therefore, in the multilayer system some intact TCPB molecules desorb from the surface (approximately 25 %) and partially the molecules deprotonate resulting in carboxylates ( $-\text{COO}^-$ ).

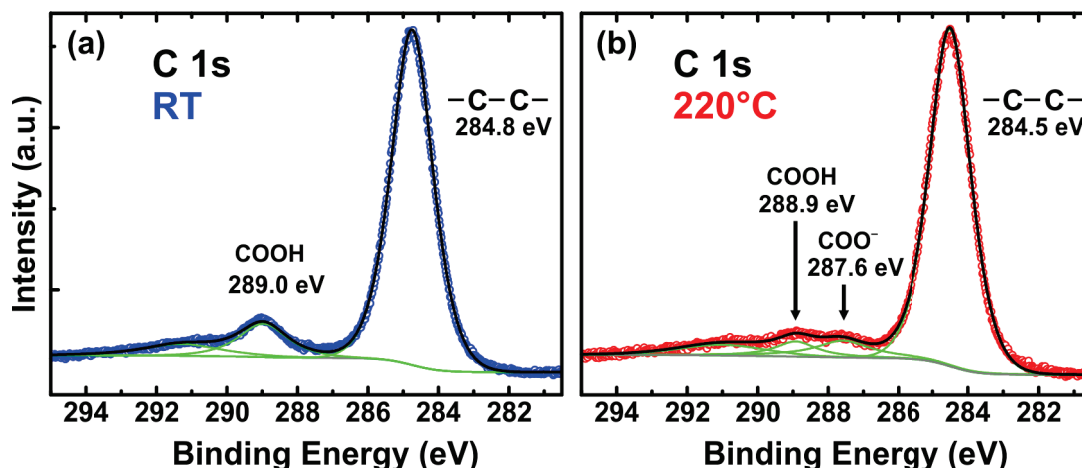


Figure 4.22: XPS C 1s data on multilayers of TCPB deposited on Cu(111) (a) at RT and (b) after post-annealing at 220 °C (493 K). Peak assignments are indicated. (a) High binding energy peak at 289 eV is assigned to three carbon atoms in the (intact) carboxyl groups and the low binding energy peak at 284.8 eV corresponds to 24 C atoms within the phenyl rings. The intensity ratio is in accordance with the number of contributing C atoms within one molecule ( $3/27 = 11\%$  in carboxyl groups and  $24/27 = 89\%$  in phenyl rings). (b) The overall integrated intensity (area under all peaks) shrinks by 25 % suggesting partial desorption of intact molecules. A new peak appears which corresponds to C atoms in carboxylates (binding energy of 287.6 eV) indicating deprotonation of carboxyl groups in the multilayers of TCPB.

These observations are substantiated by the XPS O 1s data. Figure 4.23 shows the O 1s spectrum after annealing TCPB multilayers at 220 °C (493 K). The integrated intensity of the low binding energy peak at 530.9 eV corresponding to deprotonated molecules (oxygen atoms in carboxylates) has increased compared to the integrated intensity of the peak of oxygen atoms in hydroxyl (high binding energy peak at 533.8 eV) and carbonyl (low binding energy peak at 532.0 eV) groups and accounts for 31 % of total integrated intensity (compared to 6 % before annealing, see Fig. 4.20 d) suggesting that the majority of molecules are deprotonated after annealing. In addition, the integrated intensity of the peak of oxygen atoms in hydroxyl groups is reduced compared to the integrated intensity of the peak assigned to oxygen atoms in carbonyl groups

indicating that also a condensation reaction might take place in the multilayer system upon annealing. Finally, the peak with binding energy of 536 eV is not related to TCPB molecules and originates from the substrate. It has been included to improve the fitting procedure.

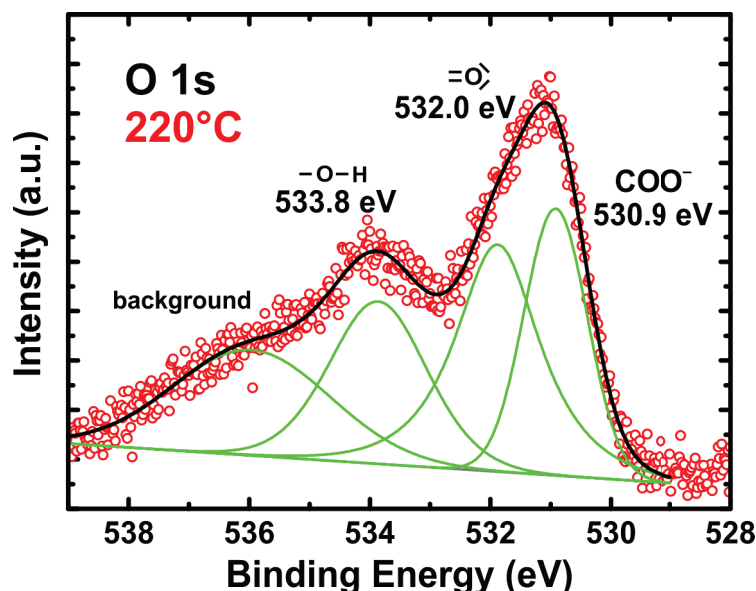


Figure 4.23: XPS O 1s data on multilayer (nominally six) of TCPB deposited on Cu(111) at RT and post-annealed at 220 °C (493 K). The peak assignments are indicated. Besides desorption of intact molecules (reduction of overall integrated intensity), deprotonation takes place in the multilayers due to thermal energy. The high binding energy peak at 536 eV is not related to TCPB molecules and originates from the substrate.

In the next section the electronic properties of 2D nanostructures are investigated. Electronic properties of the multilayer system of TCPB before and after annealing will also be presented.

## 4.4 Electronic Properties of 2D Nanostructures

In the previous sections the synthesis of two-dimensional polymers (2DP) on Au(111) as well as on Cu(111) via different on-surface coupling reactions was described and presented. In this section the electronic properties of a 2DP grown via on-surface decarboxylation on Cu(111) are illuminated. Distinct differences of the electronic features between precursor molecules and reaction products are shown and the experimental observations are explained by DFT calculations of a model compound representing the molecule used in the experiments.

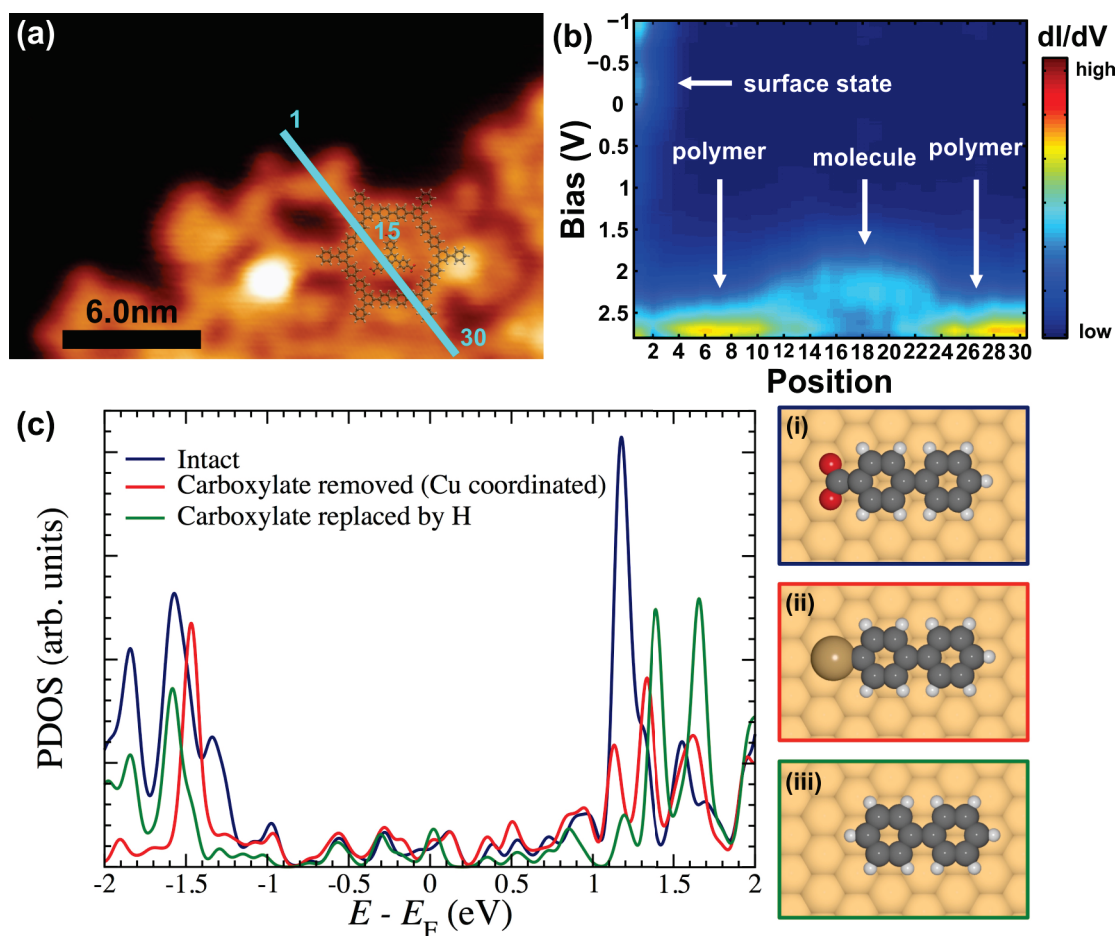


Figure 4.24: 2D STS map (b) containing 30  $dI/dV$  spectra recorded across a polymer and a monomer TCPB molecule along the cyan line in the STM topograph shown in (a),  $U = -1.5$  V,  $I = 0.2$  nA,  $T = 20$  K. (c) Projected density of states (PDOS) of (i) deprotonated model molecule biphenyl-4-carboxylic acid (blue spectrum), (ii) decarboxylated molecule connected to a Cu adatom (red spectrum), and (iii) carboxylate replaced by hydrogen atom (green spectrum) on Cu(111). The LUMO of the deprotonated molecule at 1.2 eV is significantly reduced in intensity upon removal of the carboxylate and shifts to higher energy when a new covalent bond is formed at the terminal carbon atom. In the occupied states region (HOMO) no shift can be observed. Decarboxylation and formation of organometallic structures thus have minor influence on occupied states.

Figure 4.24 a shows a topographic STM image of the 2D polymer formed via decarboxylation after annealing at 220 °C and coadsorbed precursor molecules deposited at RT. The precursor molecule is TCPB and the polymer is extended-porous graphene (see

previous section). One intact (although deprotonated) TCPB molecule is adsorbed inside the pore of the polymeric hexagon. 30 differential conductance spectra ( $dI/dV$ ) along the cyan line were taken. Figure 4.24 b shows the resulting spectra plotted as a 2D Scanning Tunneling Spectroscopy map. The applied bias voltage is shown on the y-axis, while the x-axis shows the position along the cyan line drawn in Fig. 4.24 a. The colorscale shows the magnitude of the differential conductance in arbitrary units. Blue indicates low intensity while red corresponds high intensity. As it has been shown in Section 2.1, the  $dI/dV$  signal is directly proportional to the local density of states (LDOS). Therefore the 2DSTS map shows the density of states above the polymer as well as on top of the monomer molecule inside the pore. In the negative bias range  $-1$  V to  $0$  V (occupied states regime) no states can be observed except on the bare Cu(111) substrate (line spectra 1 to 3), where the Shockley surface state of Cu(111) shows up around  $-440$  mV. [40, 172] However, in the positive bias range ( $0$  V to  $2.8$  V), on both, the polymer and monomer, unoccupied states can be detected. On top of the polymer (line spectra 4 to 11 and 24 to 30) the lowest unoccupied state (LUMO) is situated around  $2.8$  eV, while the LUMO of the precursor molecule TCPB appears closer to the Fermi energy at  $2.2$  eV (line spectra 12 to 23). Note that only the onset of the LUMO of the polymer is measured and the apparent shift of  $0.6$  eV constitutes a lower limit, while the actual shift might be higher. This destabilizing shift of the LUMO away from the Fermi energy upon polymerization is counterintuitive to a simple model in the form of HOMO/LUMO gap reduction upon polymerization [17, 173] and it is clearly not sufficient to explain the experimental observation. In particular, the decarboxylation has to be taken into account as it significantly alters the LUMO. Two effects have to be considered to explain the experimental findings in this system. The first effect is the HOMO/LUMO gap reduction due to the larger  $\pi$ -electron system in the polymerized structures as mentioned above. [17, 22, 23, 173] The second effect concerns the decarboxylation itself, which alters the electronic structure such that not only the gap size can be modified but also the energy position of the LUMO. To compare the electronic properties of monomers with polymerized structures both effects need to be taken into account. To gain further insight into the electronic structure of precursor molecules and reaction products, DFT calculations on the model compound biphenyl-4-carboxylic acid are helpful. Figure 4.24 c shows the projected density of states (PDOS) of the (i) intact but deprotonated (blue spectrum), (ii) decarboxylated and Cu coordinated (red spectrum) and (iii) decarboxylated and hydrogen terminated (green spectrum) model compound biphenyl-4-carboxylic acid. The calculated HOMO/LUMO gap accounts for approximately  $2.7$  eV. However, DFT calculations usually underestimate band gaps. [174] The most apparent difference upon decarboxylation and formation of an organometallic intermediate is the great reduction of the intensity of the peak situated around  $1.2$  eV of the intact

molecule, which corresponds to the LUMO. Qualitatively this agrees very well with the experimental findings. The exact energy position is likely different since the model molecule differs from the molecule used in the experiments. However, the calculation shows that the decarboxylation and formation of organometallic oligomers have a large influence on the energetic position of the LUMO but only a minor influence on the HOMO since the latter does not change its position significantly when the carboxylate is removed.

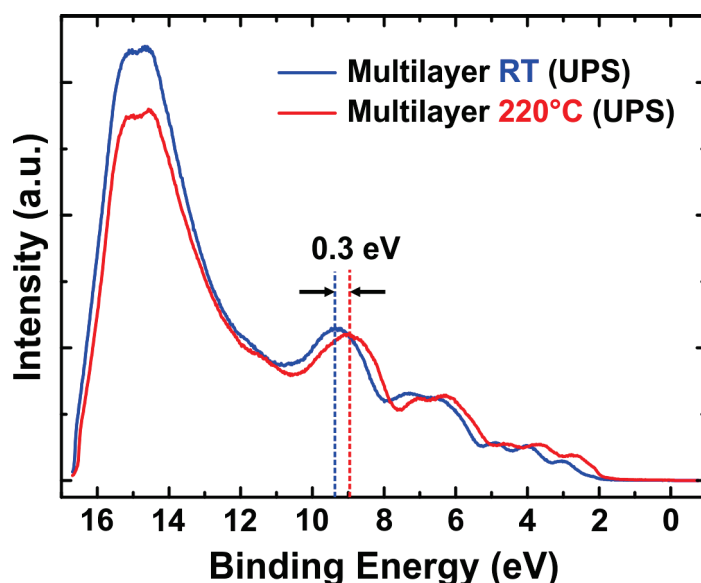


Figure 4.25: Ultra-violet photoemission spectra of multilayer TCPB deposited on Cu(111) at RT (blue spectrum) and after annealing at 220 °C (493 K) for 15 min (red). The energies of occupied orbitals shift around 300 meV towards the Fermi energy upon annealing. The gap region (0 eV to 2 eV) can be identified and the HOMO lies around 2 eV below the Fermi energy.

So far only the unoccupied states were addressed with STS (see Fig. 4.24). The d-bands of Cu(111) lie approximately between 2 eV and 4 eV below the Fermi energy and give a strong signal that interferes with the occupied states of molecules and polymers (see Fig. 2.4 b). Therefore, multilayer data of TCPB deposited at room temperature is used to address the occupied bands in the intact molecule and their shift upon annealing. Figure 4.25 shows the corresponding UPS spectra. Upon annealing at 220 °C (493 K) the occupied states shift towards the Fermi energy by approximately 0.3 eV. Since XPS data on multilayers of TCPB show that upon annealing molecules in higher lying layers mainly deprotonate (see Fig. 4.22 & Fig. 4.23), while molecules close to the Cu(111) surface most-likely still polymerize, the destabilization of occupied states is a consequence of two effects. On the one hand the deprotonation process due to

#### **4.4. Electronic Properties of 2D Nanostructures**

---

thermal energy and on the other hand polymerization in vicinity of the surface. The dominating effect for the shift in UPS is, however, the deprotonation since the amount of such molecules is higher compared to polymerization products only close to the surface (and potentially even limited to the first layer).





## 5 Conclusions and Perspectives

In this final chapter a short summary as well as the conclusions of this thesis are presented. Furthermore, prospective experiments and studies to follow up the investigations in this work are highlighted.

### 5.1 Conclusions

In the present thesis two-dimensional (2D) materials synthesized on well-defined surfaces under Ultra-High Vacuum (UHV) conditions were studied. The synthesis was carried out in a bottom-up fashion via organic molecular and metal beam epitaxy. The characterization of as-prepared samples was mainly carried out by means of Scanning Tunneling Microscopy (STM). However, complementary Photoelectron Spectroscopy (PES) data were also analyzed and presented. Additionally, in collaboration with Dr. Jonas Björk from Linköpingen University of Sweden, results of Density Functional Theory (DFT) calculations of suitable model compounds on respective surfaces were also described.

#### 5.1.1 Non-Covalent 2D materials

2D materials based on supramolecular chemistry, that is non-covalent interactions such as metal-ligand or dipolar interactions, hydrogen bonding or van der Waals forces, exhibit many interesting and promising properties. Initially, the self-assembly of a dicarboxylic acid namely terephthalic acid (TPA) on Ag(100) was described. Subsequently, it was shown that the densely packed self-assembled islands consisting of TPA molecules and stabilized by hydrogen bonding could alter the homoepitaxial growth of silver (Ag) atoms on Ag(100) in a way that the growth occurred smoother. In addition, Ag atoms penetrated the self-assembled islands without disrupting them

and Ag island growth was initiated underneath the molecular islands at room temperature (RT). Secondly, it was shown that in presence of magnesium (Mg) atoms and TPA molecules on Ag(100) the STM tip could induce finger formation along step-edges at RT. A potential mechanism was proposed: The interaction between the electric field which is present inside the tip-sample junction and Mg atoms which are partially ionized and probably surrounded by TPA molecules on Ag(100) might lead to the tip-induced finger formation. However, further experimentation is needed to obtain a complete picture of the underlying process. Step-edge altering could not be induced in absence of one compound and both materials, Mg atoms and TPA molecules had to be present on the surface. Finger formation could not be thermally induced either. Finally, the synthesis of an amorphous metal-organic coordination network (MOCN) consisting of iron (Fe) atoms as metal centers and an important organic semiconductor functionalized with two cyano groups ( $C\equiv N$ ) as ligands (2,7-dicyano[1]benzothieno[3,2-b]benzothiophene) was presented. Synthesis at RT lead to a network with Fe atoms coordinated to 2 to 6 cyano groups. Statistical tools were applied to characterize the amorphous MOCN and to compare it with other 2D amorphous materials reported in literature such as amorphous  $SiO_2$ . In addition, it was shown that at elevated temperatures the amorphous MOCN phase segregates into pure metallic and pure organic phases. This highlighted an important drawback of MOCNs which is their limited stability against temperature.

### 5.1.2 On-Surface Synthesis of Covalent Nanostructures

In contrast to 2D supramolecular materials such as MOCNs, covalent organic 2D polymers (2DP) are more stable due to the nature of covalent bonds. Via various on-surface reactions which are inspired by organic solution chemistry, adequately chosen precursor molecules react on well-defined (metal) surfaces to 2DP. In the first part the most-widely applied on-surface reaction, namely Ullmann coupling, was presented. As originally in solution chemistry the dehalogenation reaction occurs copper-catalyzed, on-surface Ullmann coupling reaction has been widely studied on metal surfaces. Therefore, in this thesis it was shown that the on-surface Ullmann coupling reaction also occurs on a passivated Ni(111) surface as a first step to probe the on-surface Ullmann coupling also on non-metallic substrates. For the passivation an atomically thin layer of either hexagonal boron nitride (h-BN) or graphene was used. Both materials can be easily grown on transition metals. It was shown that the two isoelectronic materials exhibited strong similarities regarding the on-surface Ullmann coupling despite their different electronic structure of insulating h-BN and conductive graphene. Furthermore, on-surface Glaser coupling and cyclotrimerization of an arylalkyne functionalized with a triazine core was studied on Au(111). The

cleverly chosen precursor molecule results in a 2DP which is doped with nitrogen (N) atoms. In addition, the produced nanostructures formed via on-surface Glaser coupling showed high conformational flexibility. Furthermore, it was highlighted that cyclotrimerization leads to an interesting 2DP which showed alternating connections points consisting of phenyl rings and triazine cores. This is especially interesting regarding host-guest chemistry and catalytic considerations. Finally, a comprehensive study of the on-surface decarboxylation reaction on Cu(111) for the growth of extended porous graphene (pore size around 2.1 nm) was presented. For this reaction a tripodal, commercially available, precursor molecule with three terminal carboxyl groups was used and the reaction pathway was fully illuminated through STM, XPS and DFT calculations. In addition, the electronic properties of the monomers as well as 2DP were addressed with STS and UPS. With the support of DFT calculations, it was shown that the abstraction of carboxyl groups upon polymerization destabilizes the unoccupied states despite the larger the  $\pi$ -conjugation system in the polymeric structures. These insights into the electronic structure of precursor molecules and their respective polymers is essential for the design of 2DP with tailored and desired electronic properties for potential applications.

## 5.2 Perspectives

In the previous section the work presented in this thesis was summarized and in this section possible future experiments will be suggested.

### 5.2.1 Atomically Thin 2D Heterostructures

In this section the idea of the synthesis and growth of an in-plane atomically thin heterostructure is presented. Graphene constitutes a zero band gap material whereas porous graphene exhibits a direct band gap of approximately 2.35 eV [18, 175] (see also Fig. 5.1, right side). Therefore, combining both materials in-plane laterally resembles an atomically thin metal-semiconductor junction known from semiconductor physics. Metal-semiconductor junctions (Schottky diode junctions) are mainly used in Schottky transistors as base.

Porous graphene has been fabricated atomically precisely on the noble metal surfaces Cu(111), Ag(111), and Au(111) and best results were obtained on Ag(111). [135, 136] In contrast, graphene flakes with controlled terminations (armchair and zigzag edges) are usually grown on transition metal surfaces such as Ir(111) [176–178], Pt(111) [179] or Ni(111). [180] The growth of graphene nanoflakes on Ir(111) with subsequent intercalation of a couple of nanometer of either Ag or Au atoms has been demonstrated

recently. [177, 181] Consequently, graphene flakes on either Ag(111) or Au(111) can be obtained which can in turn be coupled to porous graphene via on-surface Ullmann coupling for instance. [135, 136]

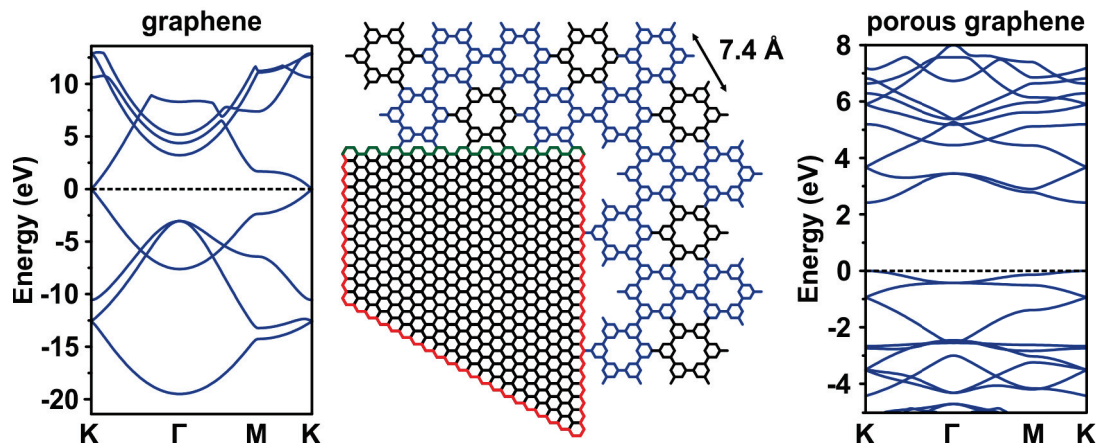


Figure 5.1: Sketch of a possible in-plane atomically thin heterostructure built up of graphene and porous graphene. The graphene flake constitutes both terminations, that is armchair (green) and zigzag (red) edges. However, more covalent bonds (connections points) are formed between the armchair edge of graphene and porous graphene. Some monomer units for the synthesis of porous graphene are color-coded (blue and black). Additionally, gas-phase DFT calculated band structures of the pristine materials are shown. Left: Graphene. Right: Porous graphene.

Figure 5.1 shows a sketch of a possible in-plane atomically thin heterostructure consisting of a graphene flake and porous graphene. The graphene flake is sketched in such a way that it exhibits both terminations, armchair and zigzag edges. It is visible that the best connection to porous graphene is realized along the armchair edge of the graphene flake. The reason for this can be found in the symmetry of the precursor molecule used to grow porous graphene. The macrocycle cyclohexa-*m*-phenylene (CHP) is six-fold symmetric and thus the growth results only in polyphenylene (porous graphene) islands which are terminated with edges equivalent to armchair edges of graphene. Single precursor molecules are highlighted within the sketch in Fig. 5.1. However, it might still be possible to form a heterostructure along the zigzag edge of graphene although this will lead to less covalent bonds between graphene and porous graphene. In addition, Figure 5.1 shows also gas-phase DFT calculations of the band structure of graphene (left side) and porous graphene (right side). As mentioned, porous graphene exhibits a direct band gap at the *K*-point of approximately 2.35 eV. However, this is most-likely a lower bound as DFT calculations tend to underestimate band gaps. Nonetheless, a clear difference in the dispersion between these two

materials is visible (in addition to the size of the band gap). It is therefore highly interesting how the bands will behave and align when a heterostructure consisting of both materials is fabricated.

With the growth recipe mentioned above such a heterojunction can be fabricated under clean UHV conditions. The characterization via STS will give insights into the transition region of the graphene–porous graphene junction. In addition, in order to decouple the heterostructure from the underlying metal substrate, iodine atoms can be intercalated as it has been shown recently by Rastgoo-Lahrood et al. [31] Furthermore, silicon intercalation has also proven to be suitable for successful decoupling of graphene from Ir(111) [182] and thus might also be appropriate for successful decoupling the graphene – porous graphene heterostructure.

Finally, Figure 5.2 shows preliminary data of the attempt to fabricate heterojunctions between h-BN islands grown directly on Cu(111) [183] and 2D nanostructures with the precursor molecule TCPB presented in Chapter 4. Although this is not the heterojunction consisting of graphene and porous graphene as discussed above, the data give insight into the fundamental mechanism and behavior as a first investigation. Figure 5.2 presents two STM images recorded at 20 K in which bare Cu(111) surface, h-BN islands and polymeric structures are visible. The h-BN islands show some defects. However, in Figure 5.2 b the electronically arising Moiré pattern can be faintly observed on the lower island. Although the quality of the h-BN islands as well as the 2D nanostructures is not very high, some heterojunctions between h-BN islands and 2D polymers can be recognized (indicated by red arrows in Fig. 5.2). These first results are a proof of principle that it should be possible to fabricate atomically thin 2D heterostructures. Nevertheless, the focus will be to grow defect free structures and clean heterojunctions as they are indispensable to access intrinsic electronic properties afterwards.



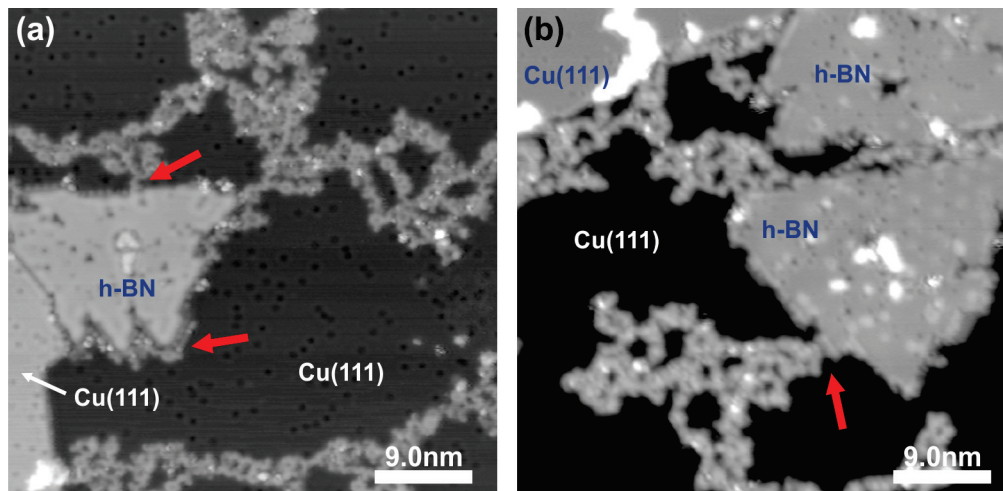


Figure 5.2: First attempts of creating a 2D heterostructure consisting of h-BN and 2D polymers. The h-BN islands were directly grown on a Cu(111) surface. Subsequently, TCPB precursor molecules were introduced and reacted to polymeric structures. Bare Cu(111) and h-BN islands are indicated. Red arrows highlight potential heterojunctions. (a)  $U = 2\text{ V}$ ,  $I = 0.1\text{ nA}$ ,  $T = 20\text{ K}$ . (b)  $U = 4\text{ V}$ ,  $I = 0.1\text{ nA}$ ,  $T = 20\text{ K}$ .

## Bibliography

- [1] Binnig, G., Rohrer, H., Gerber, C. & Weibel, E. Tunneling Through a Controllable Vacuum Gap. *Appl. Phys. Lett.* **40**, 178–180 (1982).
- [2] Binnig, G. & Rohrer, H. Scanning Tunneling Microscopy - From Birth to Adolescence. *Rev. Mod. Phys.* **59**, 615–625 (1987).
- [3] Rosei, F. *et al.* Properties of large organic molecules on metal surfaces. *Prog. Surf. Sci.* **71**, 95–146 (2003).
- [4] Eigler, D. M. & Schweizer, E. K. Positioning Single Atoms With a Scanning Tunnelling Microscope. *Nature* **344**, 524–526 (1990).
- [5] Gimzewski, J., Stoll, E. & Schlittler, R. Scanning tunneling microscopy of individual molecules of copper phthalocyanine adsorbed on polycrystalline silver surfaces. *Surf. Sci.* **181**, 267–277 (1987).
- [6] Barth, J., Costantini, G. & Kern, K. Engineering atomic and molecular nanostructures at surfaces. *Nature* **437**, 671–679 (2005).
- [7] Bartels, L. Tailoring molecular layers at metal surfaces. *Nat. Chem.* **2**, 87–95 (2010).
- [8] Novoselov, K. S. *et al.* Electric Field Effect in Atomically Thin Carbon Films. *Science* **306**, 666–669 (2004).
- [9] Radisavljevic, B., Radenovic, A., Brivio, J., Giacometti, V. & Kis, A. Single-layer MoS<sub>2</sub> transistors. *Nat. Nanotechnol.* **6**, 147–150 (2011).
- [10] Liu, H. *et al.* Phosphorene: An Unexplored 2D Semiconductor with a High Hole Mobility. *ACS Nano* **8**, 4033–4041 (2014).
- [11] Miró, P., Audiffred, M. & Heine, T. An atlas of two-dimensional materials. *Chem. Soc. Rev.* **43**, 6537–6554 (2014).

## Bibliography

---

- [12] Vyas, V. S., Lau, V. W.-H. & Lotsch, B. V. Soft Photocatalysis: Organic Polymers for Solar Fuel Production. *Chem. Mater.* **28**, 5191–5204 (2016).
- [13] Xu, M., Liang, T., Shi, M. & Chen, H. Graphene-Like Two-Dimensional Materials. *Chem. Rev.* **113**, 3766–3798 (2013).
- [14] Perepichka, D. & Rosei, F. Extending Polymer Conjugation into the Second Dimension. *Science* **323**, 216–217 (2009).
- [15] Zhu, P. & Meunier, V. Electronic properties of two-dimensional covalent organic frameworks. *J. Chem. Phys.* **137**, 244703 (2012).
- [16] Liang, L., Zhu, P. & Meunier, V. Electronic, structural, and substrate effect properties of single-layer covalent organic frameworks. *J. Chem. Phys.* **142**, 184708 (2015).
- [17] Gutzler, R. & Perepichka, D. F.  $\pi$ -electron conjugation in two dimensions. *J. Am. Chem. Soc.* **135**, 16585–16594 (2013).
- [18] Du, A., Zhu, Z. & Smith, S. C. Multifunctional porous graphene for nanoelectronics and hydrogen storage: New properties revealed by first principle calculations. *J. Am. Chem. Soc.* **132**, 2876–2877 (2010).
- [19] Lu, R. *et al.* Tunable band gap and hydrogen adsorption property of a two-dimensional porous polymer by nitrogen substitution. *Phys. Chem. Chem. Phys.* **15**, 666–670 (2013).
- [20] Zhou, J. & Sun, Q. Magnetism of phthalocyanine-based organometallic single porous sheet. *J. Am. Chem. Soc.* **133**, 15113–15119 (2011).
- [21] Wang, Y., Yuan, H., Li, Y. & Chen, Z. Two-dimensional iron-phthalocyanine (Fe-Pc) monolayer as a promising single-atom-catalyst for oxygen reduction reaction: a computational study. *Nanoscale* **7**, 11633–11641 (2015).
- [22] Cardenas, L. *et al.* Synthesis and electronic structure of a two dimensional  $\pi$ -conjugated polythiophene. *Chem. Sci.* **4**, 3263–3268 (2013).
- [23] Wiengarten, A. *et al.* Surface-Assisted Dehydrogenative Homocoupling of Porphine Molecules. *J. Am. Chem. Soc.* **136**, 9346–9354 (2014).
- [24] Lindner, R. & Kühnle, A. On-Surface Reactions. *ChemPhysChem* **16**, 1582–1592 (2015).
- [25] Lackinger, M. On-surface polymerization - a versatile synthetic route to two-dimensional polymers. *Polym. Int.* **64**, 1073–1078 (2015).

- 
- [26] Franc, G. & Gourdon, A. Covalent networks through on-surface chemistry in ultra-high vacuum: state-of-the-art and recent developments. *Phys. Chem. Chem. Phys.* **13**, 14283–14292 (2011).
- [27] El Garah, M., MacLeod, J. M. & Rosei, F. Covalently bonded networks through surface-confined polymerization. *Surf. Sci.* **613**, 6–14 (2013).
- [28] Gourdon, A. (ed.) *On-Surface Synthesis*. Advances in Atom and Single Molecule Machines (Springer, 2016).
- [29] Méndez, J., López, F. & Martín-Gago, J. On-surface synthesis of cyclic organic molecules. *Chem. Soc. Rev.* **40**, 4578–4590 (2011).
- [30] Eichhorn, J. *et al.* On-Surface Ullmann Coupling: The Influence of Kinetic Reaction Parameters on the Morphology and Quality of Covalent Networks. *ACS Nano* **8**, 7880–7889 (2014).
- [31] Rastgoo-Lahrood, A. *et al.* Post-Synthetic Decoupling of On-Surface-Synthesized Covalent Nanostructures from Ag(111). *Angew. Chem. Int. Ed.* **55**, 7650–7654 (2016).
- [32] Feynman, P. R. There's Plenty of Room at the Bottom. *Engineering and Science* **23**, 22–36 (1960).
- [33] Schwabl, F. *Quantenmechanik für Fortgeschrittene (QM II)* (2008).
- [34] Schwabl, F. *Quantenmechanik (QM I)* (2007).
- [35] Tersoff, J. & Hamann, D. R. Theory of the Scanning Tunneling Microscope. *Phys. Rev. B* **31**, 805–813 (1985).
- [36] Tersoff, J. & Hamann, D. R. Theory and Application for the Scanning Tunneling Microscope. *Phys. Rev. Lett.* **50**, 1998–2001 (1983).
- [37] Ternes, M. *Scanning Tunneling Spectroscopy at the Single Atom Scale*. Ph.D. thesis, Ecole Polytechnique Fédérale de Lausanne (2006).
- [38] Hertz, H. Ueber einen Einfluss des ultravioletten Lichtes auf die electrische Entladung. *Ann. Phys. Chem.* **267**, 983–1000 (1887).
- [39] Einstein, A. Über einen die Erzeugung und Verwandlung des Lichtes betreffenden heuristischen Gesichtspunkt. *Ann. Phys.* **322**, 132–148 (1905).
- [40] Kevan, S. D. Evidence for a new broadening mechanism in angle-resolved photoemission from Cu(111). *Phys. Rev. Lett.* **50**, 526–529 (1983).

## Bibliography

---

- [41] Hüfner, S. *Photoelectron Spectroscopy* (Springer, 1996).
- [42] Gartland, P. O., Berge, S. & Slagsvold, B. J. Photoelectric Work Function of a Copper Single Crystal for the (100), (110), (111), and (112) Faces. *Phys. Rev. Lett.* **28**, 738–739 (1972).
- [43] Sessi, V. *Coordination Dependent Magnetic Properties of 3d and 4d Metal Nano-Structures*. Ph.D. thesis, Ecole Polytechnique Fédérale de Lausanne (2010).
- [44] Krotzky, S. G. *Nanostructures at Well-Defined Surfaces*. Ph.D. thesis, Universität Konstanz (2013).
- [45] Stipe, B. C., Rezaei, M. A. & Ho, W. A Variable-Temperature Scanning Tunneling Microscope Capable of Single-Molecule Vibrational Spectroscopy. *Rev. Sci. Int.* **70**, 137 (1999).
- [46] Besocke, K. An Easily Operable Scanning Tunneling Microscope. *Surf. Sci.* **181**, 145–153 (1987).
- [47] Frohn, J., Wolf, J. F., Besocke, K. & Teske, M. Coarse Tip Distance Adjustment and Positioner for a Scanning Tunneling Microscope. *Rev. Sci. Int.* **60**, 1200–1201 (1989).
- [48] Krotzky, S. *et al.* Thermodynamics of the Segregation of a Kinetically Trapped Two-Dimensional Amorphous Metal–Organic Network. *J. Phys. Chem. C* **120**, 4403–4409 (2016).
- [49] Thiel, P. A. & Evans, J. W. Nucleation, Growth, and Relaxation of Thin Films: Metal(100) Homoepitaxial Systems. *J. Phys. Chem. B* **104**, 1663–1676 (2000).
- [50] Thiel, P. A., Shen, M., Liu, D.-J. & Evans, J. W. Coarsening of Two-Dimensional Nanoclusters on Metal Surfaces. *J. Phys. Chem. C* **113**, 5047–5067 (2009).
- [51] Evans, J., Thiel, P. & Bartelt, M. Morphological evolution during epitaxial thin film growth: Formation of 2D islands and 3D mounds. *Surf. Sci. Rep.* **61**, 1–128 (2006).
- [52] Zhang, C.-M. *et al.* Submonolayer island formation and the onset of multilayer growth during Ag/Ag(100) homoepitaxy. *Surf. Sci.* **406**, 178–193 (1998).
- [53] Sanchez, J. R. & Evans, J. W. Diffusion of small clusters on metal (100) surfaces: Exact master-equation analysis for lattice-gas models. *Phys. Rev. B* **59**, 3224–3233 (1999).



- 
- [54] Han, Y., Liu, D.-J. & Evans, J. W. Real-Time Ab Initio KMC Simulation of the Self-Assembly and Sintering of Bimetallic Epitaxial Nanoclusters: Au + Ag on Ag(100). *Nano Lett.* **14**, 4646–4652 (2014).
- [55] Stoldt, C. R. *et al.* Evolution of Far-From-Equilibrium Nanostructures Formed by Cluster-Step and Cluster-Cluster Coalescence in Metal Films. *Phys. Rev. Lett.* **81**, 2950–2953 (1998).
- [56] Schwoebel, R. L. Step Motion on Crystal Surfaces. *J. Appl. Phys.* **37**, 3682 (1966).
- [57] Ehrlich, G. Atomic View of Surface Self-Diffusion: Tungsten on Tungsten. *J. Chem. Phys.* **44**, 1039 (1966).
- [58] Alvarez, J., Lundgren, E., Torrelles, X. & Ferrer, S. Effect of a Surfactant in Homoepitaxial Growth of Ag(001): Dendritic Versus Faceted Island Morphologies. *Surf. Sci.* **464**, 165–175 (2000).
- [59] Shen, M., Liu, D.-J., Jenks, C. J., Thiel, P. A. & Evans, J. W. Accelerated coarsening of Ag adatom islands on Ag(111) due to trace amounts of S: Mass-transport mediated by Ag–S complexes. *J. Chem. Phys.* **130**, 094701 (2009).
- [60] Copel, M., Reuter, M. C., Kaxiras, E. & Tromp, R. M. Surfactants in epitaxial growth. *Phys. Rev. Lett.* **63**, 632–635 (1989).
- [61] Fiorentini, V., Oppo, S. & Scheffler, M. Towards an understanding of surfactant action in the epitaxial growth of metals: The case of Sb on Ag(111). *Appl. Phys. A* **60**, 399–402 (1995).
- [62] van der Vegt, H. A., van Pinxteren, H. M., Lohmeier, M., Vlieg, E. & Thornton, J. M. C. Surfactant-induced layer-by-layer growth of Ag on Ag(111). *Phys. Rev. Lett.* **68**, 3335–3338 (1992).
- [63] Vrijmoeth, J., van der Vegt, H. A., Meyer, J. A., Vlieg, E. & Behm, R. J. Surfactant-Induced Layer-by-Layer Growth of Ag on Ag(111): Origins and Side Effects. *Phys. Rev. Lett.* **72**, 3843–3846 (1994).
- [64] Ruben, M. *et al.* 2D Supramolecular Assemblies of Benzene-1,3,5-triyl-tribenzoic Acid: Temperature-Induced Phase Transformations and Hierarchical Organization with Macrocyclic Molecules. *J. Am. Chem. Soc.* **128**, 15644–15651 (2006).
- [65] Clair, S. *et al.* STM study of terephthalic acid self-assembly on Au(111): Hydrogen-bonded sheets on an inhomogeneous substrate. *J. Phys. Chem. B* **108**, 14585–14590 (2004).

## Bibliography

---

- [66] Bromann, K., Brune, H., Röder, H. & Kern, K. Interlayer Mass Transport in Homoepitaxial and Heteroepitaxial Metal Growth. *Phys. Rev. Lett.* **75**, 677–680 (1995).
- [67] Ge, X. & Morgenstern, K. Ehrlich-Schwoebel barrier and interface-limited decay in island kinetics on Ag(100). *Phys. Rev. B* **85**, 045417 (2012).
- [68] Stepanow, S. *et al.* Steering molecular organization and host–guest interactions using two-dimensional nanoporous coordination systems. *Nat. Mater.* **3**, 229–233 (2004).
- [69] Skomski, D., Abb, S. & Tait, S. L. Robust Surface Nano-Architecture by Alkali–Carboxylate Ionic Bonding. *J. Am. Chem. Soc.* **134**, 14165–14171 (2012).
- [70] Moroni, R., Bisio, F. & Mattera, L. Mg deposition on Ag(100): Temperature evolution of the structural and electronic properties. *Appl. Surf. Sci.* **212–213**, 224–229 (2003).
- [71] Wollschläger, J. *et al.* Epitaxial Growth of Mg on Pd(100) and Ag(100): Growth Modes for Complete and Incomplete Adlayer Condensation. In *Energy*, 100, 235–244 (1997).
- [72] Yin, F., Palmer, R. E. & Guo, Q. Faceting of nanoscale fingers on the (111) surface of gold. *Surf. Sci.* **600**, 1504–1509 (2006).
- [73] Guo, Q., Yin, F. & Palmer, R. Beyond the Herringbone Reconstruction: Magic Gold Fingers. *Small* **1**, 76–79 (2004).
- [74] Yin, F., Palmer, R. & Guo, Q. Nanoscale surface recrystallization driven by localized electric field. *Phys. Rev. B* **73**, 073405 (2006).
- [75] Wilson, K. E., Früchtl, H. a., Grillo, F. & Baddeley, C. J. (S)-Lysine adsorption induces the formation of gold nanofingers on Au(111). *Chem. Commun.* **47**, 10365 (2011).
- [76] Pascual, J. I. *et al.* Mesoscopic chiral reshaping of the Ag(110) surface induced by the organic molecule PVBA. *J. Chem. Phys.* **120**, 11367–11370 (2004).
- [77] Vyas, V. S., Gutzler, R., Nuss, J., Kern, K. & Lotsch, B. V. Optical gap in herringbone and  $\pi$ -stacked crystals of [1]benzothieno[3,2-b]benzothiophene and its brominated derivative. *CrystEngComm* **16**, 7389–7392 (2014).
- [78] Schlickum, U. *et al.* Chiral Kagomé Lattice from Simple Ditopic Molecular Bricks. *J. Am. Chem. Soc.* **130**, 11778–11782 (2008).

- 
- [79] Schlickum, U. *et al.* Surface-Confined Metal-Organic Nanostructures from Co-Directed Assembly of Linear Terphenyl-dicarbonitrile Linkers on Ag(111). *J. Phys. Chem. C* **114**, 15602–15606 (2010).
- [80] Schlickum, U. *et al.* Metal–Organic Honeycomb Nanomeshes with Tunable Cavity Size. *Nano Lett.* **7**, 3813–3817 (2007).
- [81] Büchner, C. *et al.* Topological Investigation of Two-Dimensional Amorphous Materials. *Z. Phys. Chem.* **228**, 587–607 (2014).
- [82] Yang, F. *et al.* Identification of 5–7 Defects in a Copper Oxide Surface. *J. Am. Chem. Soc.* **133**, 11474–11477 (2011).
- [83] Li, Y. & Drabold, D. A. Symmetry breaking and low energy conformational fluctuations in amorphous graphene. *Phys. Status Solidi B* **250**, 1012–1019 (2013).
- [84] Bebensee, F. *et al.* A Surface Coordination Network Based on Copper Adatom Trimers. *Angew. Chem. Int. Ed.* **53**, 12955–12959 (2014).
- [85] Marschall, M. *et al.* Random two-dimensional string networks based on divergent coordination assembly. *Nat. Chem.* **2**, 131–137 (2010).
- [86] Meyer, J. *et al.* Tuning the formation of discrete coordination nanostructures. *Chem. Commun.* **51**, 12621–12624 (2015).
- [87] Blunt, M. O., Russell, J. C., Champness, N. R. & Beton, P. H. Templating molecular adsorption using a covalent organic framework. *Chem. Commun.* **46**, 7157–7159 (2010).
- [88] Gottardi, S. *et al.* Cyano-Functionalized Triarylamines on Au(111): Competing Intermolecular versus Molecule/Substrate Interactions. *Adv. Mater. Interfaces* **1**, 1300025 (2014).
- [89] Klyatskaya, S. *et al.* Surface-Confined Self-Assembly of Di-carbonitrile Polyphenyls. *Adv. Funct. Mater.* **21**, 1230–1240 (2011).
- [90] Kühne, D. *et al.* High-quality 2D metal-organic coordination network providing giant cavities within mesoscale domains. *J. Am. Chem. Soc.* **131**, 3881–3883 (2009).
- [91] Sirtl, T. *et al.* Control of Intermolecular Bonds by Deposition Rates at Room Temperature: Hydrogen Bonds versus Metal Coordination in Trinitrile Monolayers. *J. Am. Chem. Soc.* **135**, 691–695 (2013).

## Bibliography

---

- [92] Dmitriev, A., Spillmann, H., Lin, N., Barth, J. V. & Kern, K. Modular Assembly of Two-Dimensional Metal–Organic Coordination Networks at a Metal Surface. *Angew. Chem. Int. Ed.* **42**, 2670–2673 (2003).
- [93] Lingenfelder, M. A. *et al.* Towards Surface-Supported Supramolecular Architectures: Tailored Coordination Assembly of 1,4-Benzenedicarboxylate and Fe on Cu(100). *Chem. Eur. J.* **10**, 1913–1919 (2004).
- [94] Clair, S. *et al.* Monitoring Two-Dimensional Coordination Reactions: Directed Assembly of Co–Terephthalate Nanosystems on Au(111). *J. Phys. Chem. B* **110**, 5627–5632 (2006).
- [95] Lin, T. *et al.* Thermodynamic versus kinetic control in self-assembly of zero-, one-, quasi-two-, and two-dimensional metal-organic coordination structures. *J. Chem. Phys.* **142**, 101909 (2015).
- [96] Whitelam, S. *et al.* Common Physical Framework Explains Phase Behavior and Dynamics of Atomic, Molecular, and Polymeric Network Formers. *Phys. Rev. X* **4**, 011044 (2014).
- [97] Lin, N., Dmitriev, A., Weckesser, J., Barth, J. V. & Kern, K. Real-Time Single-Molecule Imaging of the Formation and Dynamics of Coordination Compounds. *Angew. Chem. Int. Ed.* **41**, 4779–4783 (2002).
- [98] Barth, J. V. Molecular Architectonic on Metal Surfaces. *Annu. Rev. Phys. Chem.* **58**, 375–407 (2007).
- [99] Eciija, D. *et al.* Dynamics and Thermal Stability of Surface-Confined Metal–Organic Chains. *Surf. Sci.* **643**, 91–97 (2016).
- [100] Kim, E. *et al.* Magic Numbers in Small Iron Clusters: A First-Principles Study. *Chem. Phys. Lett.* **613**, 59–63 (2014).
- [101] McIntosh, A. I., Yang, B., Goldup, S. M., Watkinson, M. & Donnan, R. S. Terahertz Spectroscopy: A Powerful New Tool for the Chemical Sciences? *Chem. Soc. Rev.* **41**, 2072–2082 (2012).
- [102] Jahanbeka, A., Chilukuri, B., Mazur, U. & Hipps, K. W. Kinetically Trapped Two-Component Self-Assembled Adlayer. *J. Phys. Chem. C* **119**, 25364–25376 (2015).
- [103] Martí-Rujas, J. *et al.* Dramatic Structural Rearrangements in Porous Coordination Networks. *J. Am. Chem. Soc.* **133**, 5853–5860 (2011).

- 
- [104] Morchutt, C., Björk, J., Straßer, C., Starke, U. & Kern, K. Interplay of Chemical and Electronic Structure on the Single-Molecule Level in 2D Polymerization (2016). Submitted.
- [105] Morchutt, C., Björk, J., Krotzky, S., Gutzler, R. & Kern, K. Covalent coupling via dehalogenation on Ni(111) supported boron nitride and graphene. *Chem. Commun.* **51**, 2440–2443 (2015).
- [106] Grill, L. *et al.* Nano-architectures by covalent assembly of molecular building blocks. *Nat. Nanotechnol.* **2**, 687–691 (2007).
- [107] Zwaneveld, N. A. A. *et al.* Organized Formation of 2D Extended Covalent Organic Frameworks at Surfaces. *J. Am. Chem. Soc.* **130**, 6678–6679 (2008).
- [108] Weigelt, S. *et al.* Covalent Interlinking of an Aldehyde and an Amine on a Au(111) Surface in Ultrahigh Vacuum. *Angew. Chem. Int. Ed.* **46**, 9227–9230 (2007).
- [109] Weigelt, S. *et al.* Surface Synthesis of 2D Branched Polymer Nanostructures. *Angew. Chem. Int. Ed.* **47**, 4406–4410 (2008).
- [110] Treier, M., Richardson, N. V. & Fasel, R. Fabrication of Surface-Supported Low-Dimensional Polyimide Networks. *J. Am. Chem. Soc.* **130**, 14054–14055 (2008).
- [111] Marele, A. C. *et al.* Formation of a surface covalent organic framework based on polyester condensation. *Chem. Commun.* **48**, 6779 (2012).
- [112] Matena, M., Riehm, T., Stöhr, M., Jung, T. & Gade, L. Transforming Surface Coordination Polymers into Covalent Surface Polymers: Linked Polycondensed Aromatics through Oligomerization of N-Heterocyclic Carbene Intermediates. *Angew. Chem. Int. Ed.* **47**, 2414–2417 (2008).
- [113] Zhong, D. *et al.* Linear Alkane Polymerization on a Gold Surface. *Science* **334**, 213–216 (2011).
- [114] Hla, S.-W., Bartels, L., Meyer, G. & Rieder, K.-H. Inducing All Steps of a Chemical Reaction with the Scanning Tunneling Microscope Tip: Towards Single Molecule Engineering. *Phys. Rev. Lett.* **85**, 2777–2780 (2000).
- [115] Lipton-Duffin, J. A., Ivasenko, O., Perepichka, D. F. & Rosei, F. Synthesis of Polyphenylene Molecular Wires by Surface-Confined Polymerization. *Small* **5**, 592–597 (2009).
- [116] Fan, Q. *et al.* Surface-assisted organic synthesis of hyperbenzene nanotroughs. *Angew. Chem. Int. Ed.* **52**, 4668–4672 (2013).

## Bibliography

---

- [117] Eichhorn, J., Heckl, W. M. & Lackinger, M. On-surface polymerization of 1,4-diethynylbenzene on Cu(111). *Chem. Commun.* **49**, 2900–2902 (2013).
- [118] Gao, H.-Y. *et al.* Glaser Coupling at Metal Surfaces. *Angew. Chem. Int. Ed.* **52**, 4024–4028 (2013).
- [119] Gao, H. Y. *et al.* Photochemical glaser coupling at metal surfaces. *J. Phys. Chem. C* **118**, 6272–6277 (2014).
- [120] Gao, H. Y. *et al.* Decarboxylative polymerization of 2,6-naphthalenedicarboxylic acid at surfaces. *J. Am. Chem. Soc.* **136**, 9658–9663 (2014).
- [121] Ullmann, F. & Bielecki, J. Ueber Synthesen in der Biphenylreihe. *Ber. Dtsch. Chem. Ges.* **34**, 2174–2185 (1901).
- [122] Björk, J., Hanke, F. & Stafström, S. Mechanisms of halogen-based covalent self-assembly on metal surfaces. *J. Am. Chem. Soc.* **135**, 5768–5775 (2013).
- [123] Björk, J. Reaction mechanisms for on-surface synthesis of covalent nanostructures. *J. Phys.: Condens. Matter* **28**, 083002 (2016).
- [124] Xi, M. & Bent, B. E. Iodobenzene on Cu(111): formation and coupling of adsorbed phenyl groups. *Surf. Sci. Lett.* **278**, 19–32 (1992).
- [125] Xi, M. & Bent, B. E. Mechanisms of the Ullmann coupling reaction in adsorbed monolayers. *J. Am. Chem. Soc.* **115**, 7426–7433 (1993).
- [126] Vasseur, G. *et al.* Quasi one-dimensional band dispersion and surface metalization in long-range ordered polymeric wires. *Nat. Commun.* **7**, 10235 (2016).
- [127] Cai, J. *et al.* Atomically precise bottom-up fabrication of graphene nanoribbons. *Nature* **466**, 470–473 (2010).
- [128] Kittelmann, M. *et al.* On-surface Covalent Linking of Organic Building Blocks on a Bulk Insulator. *ACS Nano* **5**, 8420–8425 (2011).
- [129] Kittelmann, M., Nimmrich, M., Lindner, R., Gourdon, A. & Kühnle, A. Sequential and site-specific on-surface synthesis on a bulk insulator. *ACS Nano* **7**, 5614–5620 (2013).
- [130] Gutzler, R. *et al.* Surface mediated synthesis of 2D covalent organic frameworks: 1,3,5-tris(4-bromophenyl)benzene on graphite(001), Cu(111), and Ag(110). *Chem. Commun.* 4456–4458 (2009).



- 
- [131] Walch, H., Gutzler, R., Sirtl, T., Eder, G. & Lackinger, M. Material- and orientation-dependent reactivity for heterogeneously catalyzed carbon-bromine bond homolysis. *J. Phys. Chem. C* **114**, 12604–12609 (2010).
- [132] Blunt, M. O., Russell, J. C., Champness, N. R. & Beton, P. H. Templating molecular adsorption using a covalent organic framework. *Chem. Commun.* **46**, 7157–7159 (2010).
- [133] Eichhorn, J. *On-Surface Synthesis of Two-Dimensional Organic Nanostructures*. Ph.D. thesis, Technische Universität München (2015).
- [134] Larrea, C. R. & Baddeley, C. J. Fabrication of a High-Quality, Porous, Surface-Confined Covalent Organic Framework on a Reactive Metal Surface. *ChemPhysChem* **17**, 971–975 (2016).
- [135] Bieri, M. *et al.* Porous graphenes: two-dimensional polymer synthesis with atomic precision. *Chem. Commun.* 6919–6921 (2009).
- [136] Bieri, M. *et al.* Two-dimensional polymer formation on surfaces: Insight into the roles of precursor mobility and reactivity. *J. Am. Chem. Soc.* **132**, 16669–16676 (2010).
- [137] Dienel, T. *et al.* Dehalogenation and Coupling of a Polycyclic Hydrocarbon on an Atomically Thin Insulator. *ACS Nano* **8**, 6571–6579 (2014).
- [138] Auwärter, W., Muntwiler, M., Osterwalder, J. & Greber, T. Defect lines and two-domain structure of hexagonal boron nitride films on Ni(111). *Surf. Sci.* **545**, L735–L740 (2003).
- [139] Walch, H., Gutzler, R., Sirtl, T., Eder, G. & Lackinger, M. Material- and Orientation-Dependent Reactivity for Heterogeneously Catalyzed Carbon–Bromine Bond Homolysis. *J. Phys. Chem. C* **114**, 12604–12609 (2010).
- [140] Gutzler, R. *et al.* Halogen bonds as stabilizing interactions in a chiral self-assembled molecular monolayer. *Chem. Commun.* **47**, 9453–9455 (2011).
- [141] Lahiri, J., Miller, T., Adamska, L., Oleynik, I. & Batzill, M. Graphene Growth on Ni(111) by Transformation of a Surface Carbide. *Nano Lett.* **11**, 518–522 (2010).
- [142] Lahiri, J. *et al.* Graphene growth and stability at nickel surfaces. *New. J. Phys.* **13**, 025001 (2011).
- [143] Garcia-Lekue, A. *et al.* Spin-Dependent Electron Scattering at Graphene Edges on Ni(111). *Phys. Rev. Lett.* **112**, 066802 (2014).

## Bibliography

---

- [144] Bianchini, F., Patera, L. L., Peressi, M., Africh, C. & Comelli, G. Atomic Scale Identification of Coexisting Graphene Structures on Ni(111). *J. Phys. Chem. Lett.* **5**, 467–473 (2014).
- [145] Sun, X., Entani, S., Yamauchi, Y., Pratt, A. & Kurahashi, M. Spin polarization study of graphene on the Ni(111) surface by density functional theory calculations with a semiempirical long-range dispersion correction. *J. Appl. Phys.* **114**, 143713 (2013).
- [146] Olle, M., Ceballos, G., Serrate, D. & Gambardella, P. Yield and Shape Selection of Graphene Nanoislands Grown on Ni(111). *Nano Lett.* **12**, 4431–4436 (2012).
- [147] Chen, M. *et al.* Combined Photoemission and Scanning Tunneling Microscopy Study of the Surface-Assisted Ullmann Coupling Reaction. *J. Phys. Chem. C* **118**, 6820–6830 (2014).
- [148] Björk, J. & Hanke, F. Towards design rules for covalent nanostructures on metal surfaces. *Chem. Eur. J.* **20**, 928–934 (2014).
- [149] Glaser, C. Untersuchungen über einige Derivate der Zimmtsäure. *Ann. d. Chem. u. Pharm.* **154**, 137–171 (1870).
- [150] Glaser, C. Beiträge zur Kenntniss des Acetylnylbenzols. *Ber. Dtsch. Chem. Ges.* **2**, 422–424 (1869).
- [151] Klappenberger, F. *et al.* On-Surface Synthesis of Carbon-Based Scaffolds and Nanomaterials Using Terminal Alkynes. *Acc. Chem. Res.* **48**, 2140–2150 (2015).
- [152] Vyas, V. S. *et al.* A tunable azine covalent organic framework platform for visible light-induced hydrogen generation. *Nat. Commun.* **6**, 8508 (2015).
- [153] Zhang, Y.-Q. *et al.* Homo-coupling of terminal alkynes on a noble metal surface. *Nat. Commun.* **3**, 1286 (2012).
- [154] Zhou, H. *et al.* Direct Visualization of Surface-Assisted Two-Dimensional Diyne Polycyclotrimerization. *J. Am. Chem. Soc.* **136**, 5567–5570 (2014).
- [155] Liu, J., Ruffieux, P., Feng, X., Müllen, K. & Fasel, R. Cyclotrimerization of arylalkynes on Au(111). *Chem. Commun.* **50**, 11200–11203 (2014).
- [156] Vyas, V. S. *et al.* A Tunable Azine Covalent Organic Framework Platform for Visible Light-Induced Hydrogen Generation. *Nat. Commun.* **6**, 8508 (2015).

- [157] Barth, J. V., Brune, H., Ertl, G. & Behm, R. J. Scanning Tunneling Microscopy Observations on the Reconstructed Au(111) Surface: Atomic Structure, Long-Range Superstructure, Rotational Domains, and Surface Defects. *Phys. Rev. B* **42**, 9307–9318 (1990).
- [158] Lafferentz, L. *et al.* Controlling on-surface polymerization by hierarchical and substrate-directed growth. *Nat. Chem.* **4**, 215–220 (2012).
- [159] Sánchez-Sánchez, C. *et al.* On-Surface Synthesis of BN-Substituted Heteroaromatic Networks. *ACS Nano* **9**, 9228–9235 (2015).
- [160] Stepanow, S. *et al.* Deprotonation-Driven Phase Transformations in Terephthalic Acid Self-Assembly on Cu(100). *J. Phys. Chem. B* **108**, 19392–19397 (2004).
- [161] Payer, D. *et al.* Ionic Hydrogen Bonds Controlling Two-Dimensional Supramolecular Systems at a Metal Surface. *Chem. Eur. J.* **13**, 3900–3906 (2007).
- [162] Zhang, Y.-Q. *et al.* Unusual Deprotonated Alkynyl Hydrogen Bonding in Metal-Supported Hydrocarbon Assembly. *J. Phys. Chem. C* **119**, 9669–9679 (2015).
- [163] Wang, S., Wang, W. & Lin, N. Resolving band-structure evolution and defect-induced states of single conjugated oligomers by scanning tunneling microscopy and tight-binding calculations. *Phys. Rev. Lett.* **106**, 206803 (2011).
- [164] Eichhorn, J. *et al.* On-surface Ullmann polymerization via intermediate organometallic networks on Ag(111). *Chem. Commun.* **50**, 7680–7682 (2014).
- [165] Li, Q. *et al.* Surface-Controlled Mono/Diselective ortho C–H Bond Activation. *J. Am. Chem. Soc.* **138**, 2809–2814 (2016).
- [166] Sun, Q., Zhang, C., Kong, H., Tan, Q. & Xu, W. On-Surface Aryl–Aryl Coupling via Selective C–H Activation. *Chem. Commun.* **50**, 11825–11828 (2014).
- [167] Simonov, K. A. *et al.* Effect of Substrate Chemistry on the Bottom-Up Fabrication of Graphene Nanoribbons: Combined Core-Level Spectroscopy and STM Study. *J. Phys. Chem. C* **118**, 12532–12540 (2014).
- [168] Classen, T. *et al.* Hydrogen and coordination bonding supramolecular structures of trimesic acid on Cu(110). *J. Phys. Chem. A* **111**, 12589–12603 (2007).
- [169] Parker, B., Immaraporn, B. & Gellman, A. J. Carboxylic Acid Deprotonation on the Ag(110) and Ag(111) Surfaces. *Langmuir* **17**, 6638–6646 (2001).

## Bibliography

---

- [170] Han, S. W., Joo, S. W., Ha, T. H., Kim, Y. & Kim, K. Adsorption Characteristics of Anthraquinone-2-carboxylic Acid on Gold. *J. Phys. Chem. B* **104**, 11987–11995 (2000).
- [171] Giesen, M. Scaling transition of the time dependence of step fluctuations on Cu(111). *Surf. Sci.* **442**, 543–549 (1999).
- [172] Shockley, W. On the Surface States Associated with a Periodic Potential. *Phys. Rev.* **56**, 317–323 (1939).
- [173] Zade, S. S., Zamoshchik, N. & Bendikov, M. From Short Conjugated Oligomers to Conjugated Polymers. Lessons from Studies on Long Conjugated Oligomers. *Acc. Chem. Res.* **44**, 14–24 (2011).
- [174] Perdew, J. P. Density Functional Theory and the Band Gap Problem. *Int. J. Quantum Chem.* **28**, 497–523 (2009).
- [175] Ding, Y., Wang, Y., Shi, S. & Tang, W. Electronic Structures of Porous Graphene, BN, and BC<sub>2</sub>N Sheets with One- and Two-Hydrogen Passivations from First Principles. *J. Phys. Chem. C* **115**, 5334–5343 (2011).
- [176] Phark, S.-h. *et al.* Scanning tunneling spectroscopy of epitaxial graphene nanoisland on Ir(111). *Nanoscale Res. Lett.* **7**, 255 (2012).
- [177] Leicht, P. *et al.* In Situ Fabrication Of Quasi-Free-Standing Epitaxial Graphene Nanoflakes On Gold. *ACS Nano* **8**, 3735–3742 (2014).
- [178] Coraux, J. *et al.* Growth of graphene on Ir(111). *New. J. Phys.* **11**, 023006 (2009).
- [179] Kim, H. W. *et al.* Confinement of the Pt(111) Surface State in Graphene Nanoislands. *J. Phys. Chem. C* **120**, 345–349 (2016).
- [180] Garcia-Lekue, A. *et al.* Substrate-Induced Stabilization and Reconstruction of Zigzag Edges in Graphene Nanoislands on Ni(111). *J. Phys. Chem. C* **119**, 4072–4078 (2015).
- [181] Tesch, J. *et al.* Structural and electronic properties of graphene nanoflakes on Au(111) and Ag(111). *Sci. Rep.* **6**, 23439 (2016).
- [182] Meng, L. *et al.* Silicon intercalation at the interface of graphene and Ir(111). *Appl. Phys. Lett.* **100**, 083101 (2012).
- [183] Joshi, S. *et al.* Boron Nitride on Cu(111): An Electronically Corrugated Monolayer. *Nano Lett.* **12**, 5821–5828 (2012).

## Personal Information

Name	<b>Claudius Morchutt</b>
Date of Birth	November 26, 1986
Place of Birth	Friedberg, Germany
Nationality	German
eMail	c.morchutt@gmail.com

## Education

2012 – present	<b>Doctoral Studies in Physics</b> , Ecole Polytechnique Fédérale de Lausanne, Switzerland
2006 – 2012	<b>Master Studies in Physics</b> , Philipps-Universität Marburg, Germany
2009 – 2010	<b>Erasmus Studies Abroad</b> , Université Joseph Fourier Grenoble, France
2006	<b>A levels</b> , Liebigschule Gießen, Germany

## Experience

2013 – present	<b>Ph.D. Student</b> , Max Planck Institute for Solid State Research, Stuttgart, Germany Title: <i>On-Surface Assembly and Reactions of Organic Molecules in Ultra-High Vacuum</i>
2012 – 2013	<b>Teaching Assistant</b> , Ecole Polytechnique Fédérale de Lausanne, Switzerland
May 2012 – Aug. 2012	<b>Internship</b> , BDO, Financial Advisory Services, Düsseldorf, Germany
2010 – 2011	<b>Master Thesis</b> , Commissariat à l'Energie Atomique (CEA), Grenoble, France Title: <i>Emission Properties of CdSe Quantum Dots Embedded in ZnSe Nanowires</i>

## Oral Presentations

June 2016	<b>International Workshop: On-Surface Synthesis</b> (San Sebastian, Spain) <i>Interplay of Chemical and Electronic Structure on the Single-Molecule Level in 2D Polymerization</i>
Mar. 2016	<b>DPG Frühjahrstagung (Spring meeting)</b> (Regensburg, Germany) <i>Interplay of Chemical and Electronic Structure on the Single-Molecule Level in 2D Polymerization</i>
Mar. 2015	<b>DPG Frühjahrstagung (Spring meeting)</b> (Berlin, Germany) <i>Covalent Coupling via Dehalogenation on Ni(111) Supported Boron Nitride and Graphene</i>
Apr. 2014	<b>DPG Frühjahrstagung (Spring meeting)</b> (Dresden, Germany) <i>Physisorbed Molecular Networks as Surfactants for the Growth of Ag on Ag(100)</i>

## Publications

- #1 Hötger, D., **Morchutt, C.**, Stepanow S., Etzkorn, M., Gutzler, R., and Kern, K. *2D bimetallic porphyrine network acting as bifunctional catalyst for ORR and OER: fundamental insights in the electronic structure by XMCD*, (2016). In preparation.
- #2 **Morchutt, C.**, Björk, J., Straßer, C., Starke, U., Gutzler, R., and Kern, K. *Interplay of Chemical and Electronic Structure on the Single-Molecule Level in 2D Polymerization*, (2016). Submitted.
- #3 Krotzky, S., **Morchutt, C.**, Vyas, V.S., Lotsch, B.V., Gutzler, R. & Kern, K. *Thermodynamics of the Segregation of a Kinetically Trapped Two-Dimensional Amorphous Metal-Organic Network*. J. Phys. Chem. C **120**, 4403-4409 (2016).
- #4 **Morchutt, C.**, Björk, J., Gutzler, R., and Kern, K. *Covalent Coupling via Dehalogenation on Ni(111) Supported Boron Nitride and Graphene*. Chem. Commun. **51**, 2240-2443 (2015).
- #5 Bounouar, S., **Morchutt, C.**, Elouneg-Jamroz, M., Besombes, L., André, R., Bellet-Amalric, E., Bougerol, C., den Hertog, M., Kheng, K., Tatarenko, S., and Poizat, J.Ph. *Exciton-Phonon Coupling Efficiency in CdSe Quantum Dots Embedded in ZnSe Nanowires*. Phys. Rev. B **85**, 035428 (2012).
- #6 Bounouar, S., Elouneg-Jamroz, M., den Hertog, M., **Morchutt, C.**, Bellet-Amalric, E., André, R., Bougerol, C., Genuist, Y., Poizat, J.Ph., Tatarenko, S., and Kheng, K. *Ultrafast Room Temperature Single-Photon Source from Nanowire-Quantum Dots*. Nano Lett. **12**, 2977-2981 (2012).



